*International Reviews in Physical Chemistry*
Vol. 29, No. 3, July–September 2010, 453–520

Taylor & Francis
Taylor & Francis Group

# Ultrafast X-ray scattering: structural dynamics from diatomic to protein molecules

Hyotcherl Ihee[a]*, Michael Wulff[b], Jeongho Kim[a] and Shin-ichi Adachi[c]

[a]*Department of Chemistry, Center for Time-Resolved Diffraction, Graduate School of Nanoscience and Technology (WCU), KAIST, Daejeon 305-701, Republic of Korea;* [b]*European Synchrotron Radiation Facility, 6 Rue Jules Horowitz, BP220, F-38043 Grenoble Cedex, France;* [c]*Photon Factory, High Energy Accelerator Research Organization, 1-1 O-ho, Tsukuba, Ibaraki 305-0801, Japan*

(*Received 15 March 2010; final version received 27 May 2010*)



Recent years have witnessed the birth of picosecond pump-probe X-ray diffraction and scattering techniques, thanks to the technological developments in the third generation synchrotron beamlines and advances in theory and data analysis by combining quantum calculations, molecular dynamics simulations and global fitting analysis. Our laboratories have employed this technique to study structural dynamics and spatiotemporal kinetics of many molecular systems in solution including diatomic molecules, haloalkanes, organometallic complexes and protein molecules over timescales from picoseconds (ps) to milliseconds. The visualising power and unbiased sensitivity of X-ray scattering proved to be instrumental in identifying global reaction pathways and in some cases capturing detailed three-dimensional structures of reaction intermediates. Many results have accumulated from which we have selected some interesting examples to be reviewed here. The structural dynamics of $Br_2$ and $I_2$ are compared and the reaction pathways for $HgBr_2$ and $HgI_2$ are compared. Solvents may affect the reaction pathways as illustrated in the photolysis of $CH_2I_2$ in two different solvents. How does the excitation wavelength affect the reaction pathways is another important aspect in photochemistry as shown for $Ru_3(CO)_{12}$. Applications to the folding of cytochrome-c and the structural dynamics of myoglobin and bacteriorhodopsin are also reviewed. The time resolution is currently limited to about 100 ps, the X-ray pulse width available from synchrotron sources. In the near future, X-ray free electron lasers (XFELs) will deliver 100 fs or shorter X-ray pulses. In femtosecond (fs) X-ray scattering experiments with this higher resolution, real-time observation of ultrafast chemical events, such as bond-breaking and bond-making will be possible. So far, gas-phase reactions, which are the main targets for ultrafast electron diffraction due to the high scattering power of electrons, have not yet been studied with time-resolved X-ray scattering, but in principle this discipline will become feasible with the coming XFEL sources. We thus discuss potential fs X-ray scattering experiments for gas phase as well as solution phase reactions. In addition, the high photon flux and the coherence of XFEL-generated X-ray pulses might open up new research areas, such as single-molecule diffraction.

**Keywords:** ultrafast X-ray scattering; ultrafast X-ray diffraction; structural dynamics; reaction dynamics; liquidography; solution scattering; single molecule diffraction; time-resolved; pump-probe

*Corresponding author. Email: hyotcherl.ihee@kaist.ac.kr

ISSN 0144–235X print/ISSN 1366–591X online

DOI: 10.1080/0144235X.2010.498938
http://www.informaworld.com

**Contents** PAGE

## 1. Introduction

### 1.1. *Structural dynamics*

One of the fundamental goals in physical chemistry is to describe how a chemical reaction proceeds from reactants to products via intermediates, if they exist, at the atomic and molecular levels. In particular, solution-phase reaction dynamics are of much interest since many chemical and biologically relevant reactions occur in solution. Studying reactions in solution offers opportunities for understanding not only fundamental molecular reaction dynamics but also the interplay between the solute and the solvent, but at the same time, the interactions between solutes and solvents make this task non-trivial. The solute–solvent interaction often alters the rates, pathways and branching ratios of chemical reactions through the cage effect [1–5]. For example, the timescale of the response of solvent molecules to electronic rearrangement of solute molecules critically affects the rates of photochemical reactions in liquid phase. To tackle this classical yet central question of reaction dynamics (kinetics) and to reveal reaction mechanisms at the atomic level, we need to investigate the detailed processes that take place during the reaction and gather essential information, such as the identity of reaction intermediates, the associated rate constants that connect them, and the energy flow between chemical species and states. Ideally, one wishes to track all the atomic coordinates and energies of the molecules participating in a reaction as a function of reaction time, so that the movement on a potential energy surface (PES) can be mapped out. According to traditional definitions, *reaction kinetics* is mainly concerned with determining reaction rates, whereas *reaction dynamics* is focussed on the detailed molecular motions responsible for the reaction. In this regard, we use *structural dynamics in this review to stress that X-rays are used to visualise atomic motions* in the course of a reaction process.

### 1.2. *Two experimental approaches to study reaction dynamics*

In general, two major experimental approaches have been applied to studying reaction dynamics. The first one is to make two reactant molecules collide and then investigate the reaction outcome [6–11]. By resolving the rotational, vibrational and translational energies of the products, the molecular motion at the onset of the bi-molecular reaction can be inferred even if the motion is not captured in real time. This crossed-beam approach is quite powerful in revealing reaction dynamics of bi-molecular reactions in the gas phase, but it is not so easy to adapt it to study solution-phase reactions. The other approach is to

directly track the reaction as a function of time, preferably with a sufficient time resolution. For example, in a typical pump-probe spectroscopy experiment, a reaction is initiated by an ultrashort optical laser pulse (pump), and the reaction progress is probed by another ultrashort optical laser pulse (probe) as a function of time delay between the pump and probe pulses [12–23]. This pump-probe approach may find its origin in flash photolysis developed in the 1960s and the time resolution has improved to femtoseconds, thanks to the advance of ultrafast laser technologies. Mapping the pump-probe signals as a function of time delays between the pulses can reveal useful information, such as the lifetime of an energy state and vibrational wave packet motions along PESs. The time-resolved pump-probe spectroscopy can be used for studying reactions in any phase and can be extended by replacing the optical probe pulse by a different type of probe, so that richer dynamical information can be obtained. For example, the reactions in the gas phase can be efficiently probed by ion detection using mass spectrometry because of its high sensitivity to even very dilute chemical species [24]. Also, photoelectrons can be used as a sensitive probe of the dynamics of molecules and clusters [25,26], especially when combined with ion-imaging that allows simultaneous measurements of the rotational, vibrational, electronic and translational energy distributions of the reaction products [27,28]. For reactions in solution, time-resolved transient absorption and fluorescence spectroscopy at UV and visible frequencies have been the most popular choice due to simplicity in their implementation and the high sensitivity to specific electronic states [29–32]. Besides, time-resolved vibrational spectroscopies using infrared (IR) pulses or Raman process have been used to study reaction dynamics in liquids and in solution owing to the rather direct connection of vibrational transition frequencies with molecular structure [33,34].



### 1.3. *Demand for a direct structural probe and time-resolved diffraction*

For a simple diatomic molecule, optical spectroscopic signals originating from wave packet dynamics can be directly linked to molecular structural dynamics. The situation becomes more complicated as the complexity of the molecule increases, and extracting structural dynamics becomes a daunting task even for a simple polyatomic molecule consisting of a handful of atoms let alone macromolecules. This is because the optical spectroscopy probes valence electronic states that extend over multiple atomic sites and therefore is only an indirect measure of the underlying atomic structure, except in some favourable cases of time-resolved vibrational spectroscopy [18–23] and coherent multi-dimensional spectroscopy [35–37] measurements. Thus, we need an alternative or complementary tool that provides more direct structural information.

Replacing the optical probe with X-ray [38–53] or electron [54–57] diffraction (scattering) offers a direct route to molecular structures as the diffraction (scattering) effect originates from atomic interferences in real space instead of optical resonances in energy space. In contrast to visible or IR light that is sensitive to electronic or vibrational transitions of specific chromophores, X-rays and electrons are diffracted (or scattered) off all atom–atom pairs and chemical species present in the molecule that direct information on the molecular structure can be retrieved from the measured X-ray diffraction patterns. Taking advantage of the high sensitivity of X-rays to atomic-level molecular structure, time-resolved X-ray diffraction (TRXD) (or scattering)

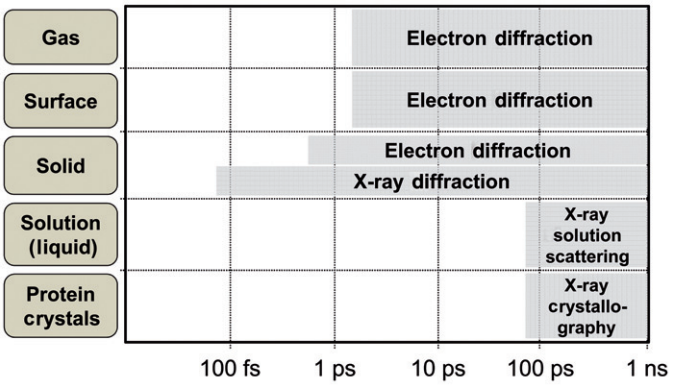


Figure 1. [Colour online] Present status of time-resolved X-ray and electron diffraction in their applications to studying dynamics in various phases and timescales. Thus far, the low penetration depth of electron diffraction has limited its application to gas phase, surface and thin films. In contrast, the X-ray diffraction has been applied to the (liquid) solution phase and to protein crystals, but its relatively poor time resolution has been a major limitation.
Source: Adapted from Ref. [231].



techniques have been applied to studying structural dynamics of chemical reactions. Diffraction is the most common and accurate method for determining molecular structure on the atomic length scale. For example, most three-dimensional (3-D) protein structures have been determined by X-ray crystallography, where X-ray diffraction signals from a single crystal with long-range order are analysed to determine the 3-D structure at atomic resolution. Combined with the pump-and-probe scheme, time-resolved X-ray or electron diffraction can provide a shortcut to structural dynamics. The applications of time-resolved X-ray and electron diffraction techniques are summarised in Figure 1. The nearly million-fold higher scattering cross-section of electrons makes electron diffraction (scattering) very useful in probing structural dynamics of dilute or thin samples, such as molecules in the gas phase, surfaces, nanostructures and thin films. On the other hand, thanks to the significantly weaker scattering cross-section of X-rays, X-rays penetrate matter several orders of magnitude better than electrons. Consequently, it is practically more convenient to use X-rays rather than electrons for probing crystalline and liquid samples with a thickness of tens of micrometres. Indeed, with the advance of X-ray synchrotron sources that can generate high-flux, ultrashort hard X-ray pulses, TRXD (scattering) techniques have become general and powerful tools to explore structural dynamics of matter. Accordingly, the techniques have been successfully applied to studying various dynamics of chemical and biological systems [38–46,58–62] and of condensed matter [47–53]. TRXD allows us to access the mechanism of structural transformations at the atomic level in crystalline state [43,44,46,47]. For example, time-resolved X-ray Laue crystallography in principle can track the positions, in three dimensions, of *all the atoms* in a protein during its biological function. On the other hand, time-resolved solution scattering [40,63–65] can probe structural dynamics in non-crystalline states of materials and thus complementing X-ray diffraction.

### 1.4. *Diffraction, scattering, crystallography and liquidography*

At this point, it may be useful for the reader to define the terms *diffraction* and *scattering*, as both terms have been used to describe diffraction from non-crystalline samples in the gas and liquid phases. Any process where the incoming wave is deviated from its original path due to the interaction with matter can be called scattering and, if the scattered wave interfere due to the (molecular) structure of the matter, the interference is called diffraction. In that sense, the interference pattern in the X-ray scattering from a liquid should be also called X-ray diffraction because the interference between the scattered X-rays still occurs from such non-crystalline samples. On the other hand, the diffraction signals from a non-crystalline sample or due to non-crystalline aspects in a crystal are commonly called diffuse scattering to distinguish it from Bragg diffraction peaks from well-ordered crystalline planes. Since most structural studies with X-ray diffraction use Bragg diffraction from a single crystal, there is another terminology to describe this technique, X-ray crystallography. To distinguish diffraction studies on liquid samples from those on crystalline samples, we introduced a new terminology: X-ray liquidography.



### 1.5. *Time-resolved X-ray liquidography*

Time-resolved X-ray liquidography (TRXL), which is also called as time-resolved X-ray solution scattering (TRXSS), provides rather direct information of transient molecular structures, because scattering signals are sensitive to all chemical species present in the sample and can be compared with the theoretical scattering signal calculated from 3-D atomic coordinates of the chemical species involved. Accordingly, TRXL using 100-ps X-ray pulses from a synchrotron has been effective in elucidating molecular geometries involved in photoinduced reaction pathways, elegantly complementing ultrafast optical spectroscopy [40,63–79]. For studying the structural dynamics of molecules in solution, time-resolved X-ray absorption spectroscopy [80–82] is a complementary tool to TRXL with the limitation of probing local structure around a metal atom or metal ion.

Thus far, compared to optical spectroscopy, the major limitation of TRXL has been the limited temporal resolution from the duration of the available X-ray pulses, which is 50–150 ps from the third generation synchrotrons. In terms of time resolution, femtosecond (fs) X-ray sources, such as laser-driven plasma and accelerator-based source have been used to investigate the dynamics of acoustic phonons, heating, non-thermal behaviour near the melting point and phase transitions in simple crystalline samples with $\sim$100 fs temporal resolution [83–86]. In such cases, the system under study is quite simple and thus the structural dynamics can be probed by monitoring only one or a few Bragg spots as a function of time. To follow atomic positions of all the atoms in more complex systems, nearly all Bragg diffraction spots need to be recorded as a function of time, and thus the current fs X-ray sources cannot be used due to their insufficient photon flux. Instead, high brilliance third generation synchrotron sources have been used to study transient structural changes in small organic [43,60], inorganic [61,62] and complex protein molecules [44,58,59] in crystals with $\sim$100 ps time resolution. The same is true for TRXL. The current time resolution is limited by the X-ray pulse width and will soon be improved into the fs regime with the advent of X-ray free electron lasers (XFELs).

Table 1. Summary of molecular systems studied by pump-probe X-ray solution scattering.

| Solute | Solvent | Excitation wavelength | References |
|---|---|---|---|
| $Br_2$ | $CCl_4$ | 400 nm | [145] |
| $I_2$ | $CCl_4$ | 520 nm | [63,215] |
| $HgBr_2$ | $CH_3OH$ | 267 nm | [227] |
| $HgI_2$ | $CH_3OH$ | 267 nm | [228] |
| $CH_2I_2$ | $CH_3OH$ | 267 nm | [65] |
| $CH_2I_2$ | $C_6H_{12}$ | 267 nm | [76] |
| $CHI_3$ | $CH_3OH$ | 267 nm | [72] |
| $C_2H_4I_2$ | $CH_3OH$ | 267 nm | [64] |
| $C_2F_4I_2$ | $CH_3OH$ | 267 nm | [74] |
| $[Pt_2(P_2O_5H_2)_4]^{4-}$ | $H_2O$ | 267 nm | [77] |
| $Tl^+ + [Pt_2(P_2O_5H_2)_4]^{4-}$ | $H_2O$ | 267 nm | [78] |
| $Ru_3(CO)_{12}$ | $C_6H_{12}$ | 390 nm | [73] |
| $Ru_3(CO)_{12}$ | $C_6H_{12}$ | 260 nm | [158] |
| Neat $H_2O$ | | 266 nm | [229] |
| Neat $CH_3OH$ | | 1.5 and 1.7 μm | [90] |
| Neat $C_6H_{12}$ | | 1.7 μm | [158] |
| Neat $CH_2Cl_2$ | | 267 nm | [230] |
| Cyt-c | $H_2O$ | 532 nm | [75] |
| Mb | $H_2O$ | 532 nm | [75,220] |
| Hb | $H_2O$ | 532 nm | [75] |
| bR | $H_2O$ | 527 nm | [193] |



### 1.6. *Outline of this review*

Table 1 lists the molecular systems studied by TRXL. Structural dynamics and spatiotemporal kinetics of a wide variety of molecular systems including diatomic molecules, haloalkanes, organometallic complexes and protein molecules in the solution phase have been studied with TRXL over timescales from picoseconds to milliseconds. Two reviews on the technique of pump-probe X-ray solution scattering already exist. [87,88] In this review, we aim to update on more recent advances and deal with topics that have not been discussed much in the previous reviews. We outline the basic theory and the formulae necessary for understanding TRXL, and then move on to describe the experimental details. As the experimental setup on beamline ID09B at the European Synchrotron Radiation Facility (ESRF) is well-described in the literature, we have chosen to describe the TRXL setup on beamline NW14A at KEK, where polychromatic X-ray pulses with an energy bandwidth of $\Delta E/E \sim 1$–5% are generated by reflecting white X-ray pulses ($\Delta E/E = 15\%$) by multilayer optics. Unlike conventional X-ray scattering/diffraction experiments, where monochromatic X-rays are used to achieve high structural resolution, polychromatic X-ray pulses with $10^2$–$10^3$ times more photons than monochromatic X-ray pulses are used, at a modest expense of the spatial resolution, since they give a higher signal-to-noise ratio (SNR) in TRXL experiments. In addition, we describe in detail the synchronisation between the laser and X-ray pulses, one of the key components in time-resolved X-ray experiments in areas ranging from diffraction,

scattering and absorption to imaging. Just as the hardware for the realisation of TRXL is challenging, the analysis of the measured data poses another challenge. For TRXL data from small molecules in solution, the protocol for the data analysis is rather well-established, whereas more developments are needed for proteins. In the latter case, the kinetic analysis is straightforward, but extracting the structural information still needs more efforts. We present the now well-established global fitting analysis for small molecules. Finally, we present some examples of reactions ranging from small molecules to proteins. Here, we attempt to highlight the aspects that can emphasise the strength of TRXL compared with time-resolved optical spectroscopy. First, we compare the results of the two diatomic molecules ($I_2$ and $Br_2$) and the two triatomic molecules ($HgI_2$ and $HgBr_2$) studied by TRXL. Then we show TRXL studies on $Ru_3(CO)_{12}$, a prototypical organometallic photocatalyst, where the dependence of the reaction pathways on the excitation wavelength was examined in great detail. We also show how the reaction pathway of the $CH_2I_2$ solute depends on the solvents (methanol and cyclohexane). Then we shift to macromolecules. We present the protein folding dynamics of cytochrome-c (Cyt-c), the light-driven structural dynamics of myoglobin (Mb) and the proton-pump protein, bacteriorhodopsin (bR).



## 2. Theoretical background

Here we first lay out the basic principle of diffraction applicable to any crystalline, liquid, gas and amorphous material. Then we present a formula specific to liquids (liquidography) and compare it with crystallography. Once the formula for describing the scattering intensity for a static liquid sample is established, we move on to show how it can be further developed to describe a solution, i.e. a sample containing solutes and solvents. Furthermore, in time-resolved scattering experiments, a small portion of the whole sample is perturbed; it is thus the difference in the scattered intensity before and after the perturbation that contains the net signal. Thus we discuss how we deal with the difference scattering curve along with the effect of polychromaticity and the temporal profile of the X-ray pulses.

### 2.1. *Scattered amplitude, scattering intensity and the structure*

If an X-ray wave is sent to a sample of interest, part of the incoming X-ray wave is scattered. The scattering amplitude, $A(\mathbf{q})$, of the X-ray wave is given by Equation (1) and vice versa (Equation 2).

$$A(\mathbf{q}) = \int \rho_e(\mathbf{r}) \exp(-i\mathbf{q} \cdot \mathbf{r}) \mathrm{d}\mathbf{r}, \tag{1}$$

$$\rho_e(\mathbf{r}) = \frac{1}{(2\pi)^3} \int A(\mathbf{q}) \exp(i\mathbf{q} \cdot \mathbf{r}) \mathrm{d}\mathbf{q}, \tag{2}$$

where $\mathbf{q}$ is the momentum transfer between the incident ($\mathbf{k_0}$) and the elastically scattered ($\mathbf{k}$) X-ray waves (Figure 2) and $\rho_e(\mathbf{r})$ the electron density of the sample as a function of the 3-D coordinate $\mathbf{r}$. These equations directly connect the molecular structure in $\rho_e(\mathbf{r})$ to the

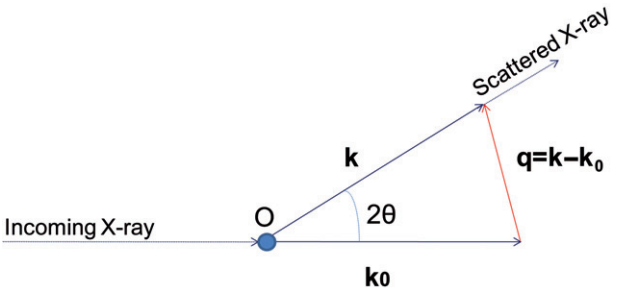


Figure 2. [Colour online] Schematic description of the scattering geometry. An X-ray wave is sent to a sample at O and scattered. The relationship between the incoming X-ray ($\mathbf{k_0}$), the scattered X-ray ($\mathbf{k}$) and momentum transfer vector $\mathbf{q}$ are shown.

amplitude of the diffracted X-ray wave via the well-known Fourier transform. In principle, if the diffracted amplitude can be measured, $\rho_e(\mathbf{r})$ can be determined by a simple Fourier transform of the amplitude (Equation 2). The very reason why X-ray scattering is so powerful in providing direct structural information is seen directly in this key equation. In reality, the situation is more complicated by the fact that we do not have technology to detect the phase of the X-ray directly, which is the famous phase problem in crystallography. Experimentally, we are restricted to (only) detect the square modulus of $A(\mathbf{q})$, i.e. the scattered intensity, $S(\mathbf{q})$, described by

$$S(\mathbf{q}) = \left| \int \rho_e(\mathbf{r}) \exp(-i\mathbf{q} \cdot \mathbf{r}) d\mathbf{r} \right|^2. \tag{3}$$

The direct Fourier transform relationship between $\rho_e(\mathbf{r})$ and $S(\mathbf{q})$ no longer holds and thus $\rho_e(\mathbf{r})$ cannot be directly determined from the measured $S(\mathbf{q})$.

Since we are interested in the atomic positions $\mathbf{r}_n$, we often express $\rho_e(\mathbf{r})$ as a superposition of electron densities centred on the atomic positions.

$$\rho_e(\mathbf{r}) = \sum_n \rho_n(\mathbf{r} - \mathbf{r}_n), \tag{4}$$

where $\rho_n$ is the electron density of the $n$th atom and $\mathbf{r}$ a certain position from the origin. In the framework of $\mathbf{r}_n$, $A(\mathbf{q})$ and $S(\mathbf{q})$ can be expressed as follows:

$$A(\mathbf{q}) = \sum_n f_n(\mathbf{q}) \exp(-i\mathbf{q} \cdot \mathbf{r}_n), \tag{5}$$

$$S(\mathbf{q}) = \sum_n \sum_m f_n(q) f_m(q) \exp(-i\mathbf{q} \cdot (\mathbf{r}_n - \mathbf{r}_m)), \tag{6}$$

where the indices $m$ and $n$ include all atoms in the sample and $f_n(\mathbf{q})$ is the scattering amplitude from the $n$th atom (the so-called atomic form factor), which is the Fourier transform of the electron density of atom $n$.

$$f_n(\mathbf{q}) = \int \rho_n(\mathbf{r}) \exp(-i\mathbf{q} \cdot \mathbf{r}) d\mathbf{r}. \tag{7}$$

For simplicity, the atom is often approximated as a spherical object and $f_n(\mathbf{q})$ depends only on the modulus of $\mathbf{q}$:

$$q = \frac{4\pi}{\lambda}\sin\theta, \tag{8}$$

where $\theta$ is half the scattering angle between $\mathbf{k}$ and $\mathbf{k_0}$. The parameters for calculating the atom-specific $f_n(q)$ are well-tabulated in the International Tables for Crystallography.

### 2.2. *Scattering from a randomly oriented liquid sample*

Since the molecules in liquids or gases are randomly oriented, the effect of isotropic averaging has to be included. The well-known Debye equation stems from the isotropic averaging of $S(\mathbf{q})$ into $S(q)$.

$$\begin{aligned} S(q) &= \sum_n \sum_m f_n(q) f_m(q) \frac{\sin qr_{nm}}{qr_{nm}} \\ &= \sum_n f_n^2(q) + \sum_n \sum_{m \neq n} f_n(q) f_m(q) \frac{\sin qr_{nm}}{qr_{nm}}, \end{aligned} \tag{9}$$

where $r_{nm}$ is the distance between $n$th and $m$th atoms. This isotropic averaging is not necessary but one can see that the calculation is greatly simplified to become a function of one dimension instead of three dimensions. Although this Equation (9) is the key working formula for gas-phase scattering, the enormous number of possible combinations of $n$ and $m$ in a liquid makes the Debye equation practically unusable. This problem can be solved by introducing the pair distribution function $g_{ij}(r)$ between atom types $i$ and $j$ so that $4\pi r^2 g_{ij}(r)\mathrm{d}r$ is the probability of finding a $j$-type atom at the distance $r$ from an $i$-type atom. With $g_{ij}(r)$, Equation (9) can be expressed as follows.

$$S(q) = \sum_i N_i f_i^2(q) + \sum_i \sum_{i \neq j} \frac{N_i N_j}{V} f_i(q) f_j(q) \int_0^\infty (g_{ij}(r) - 1) \frac{\sin(qr)}{qr} 4\pi r^2 \mathrm{d}r, \tag{10}$$

where the indexes $i$ and $j$ include all atom *types*, $N_i$ the number of $i$-type atoms and $V$ the volume of the sample. One can see that Equation (10) is more general than Equation (9). In the case of gas-phase molecules, the pair distribution function is essentially a delta function and thus Equation (10) eventually reverts to Equation (9). Equation (10) tells us that a theoretical $S(q)$ curve can be calculated directly from the $g_{ij}(r)$ functions and thus compared with the experimental $S(q)$ curve. This is the basis for the comparison of experimental scattering curves against theoretical ones. Molecular dynamics (MD) simulations can provide the $g_{ij}(r)$ functions for elemental liquids and solutions. In the MD simulation, a large number of molecules, typically 256, 512, 1024 or 2048, are allowed to move in the specified force fields and the $g_{ij}(r)$ functions can be calculated from the resulting MD trajectories. Note that MD is normally performed in thermal equilibrium even if excited-state solutes are involved.

### 2.3. *Comparison of crystallography and liquidography*

The key comparisons between crystallography and liquidography are outlined in Figure 3. In crystallography, the sample is a single crystal with long-range orders. The lattice in a periodic array makes the X-ray wave diffract into specific $\mathbf{q}$ directions that satisfy the

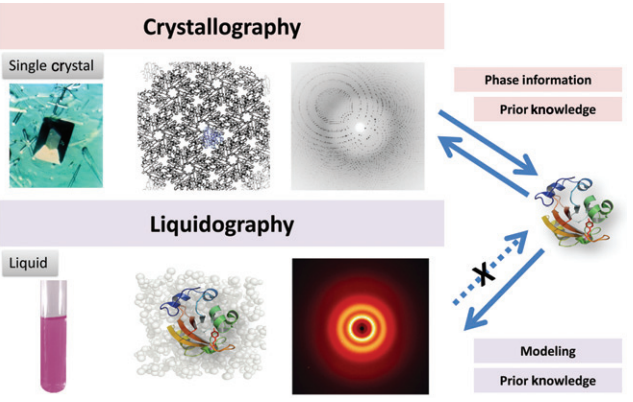


Figure 3. The key differences between crystallography and liquidography (solution scattering) are schematically highlighted. Whether the sample under investigation is single crystalline or liquid solution makes the distinction between crystallography and liquidography. In crystallography, the sample is a single crystal which has long-range orders. Because of the diffraction from the lattice, we see diffraction spots in special locations that satisfy the Bragg law and that can be indexed with *hkl*'s. The arrows indicate the possibility of conversion between the scattering information and the molecular structure. If we know the structure amplitudes and phases of all *hkl*'s, we can reconstruct the 3-D electron density as a function of *xyz*. The diffraction patterns can be always calculated from a structure model. In the case of liquid scattering, due to the lack of the lattice and the random orientation of molecules, it gives an isotropically averaged smooth oscillation profile. Due to the isotropic averaging, we cannot reconstruct the 3-D electron density, but only 1-D pair distribution function as a function of *r*. Since the information content is reduced, it is not possible to directly reconstruct the structure from the data. However, it is still possible to calculate the scattering pattern from a structure and thus compare it with the scattering data.



Laue condition. This is why the diffracted signal from a single crystal shows sharp diffraction spots. In the case of amorphous samples or a single molecule without periodicity, the diffracted X-rays can appear in the entire **q** space and the sharp Bragg peaks disappear. In addition, due to the random molecular orientation, the information in 3-D **q** space collapses into one-dimensional (1-D) $q$ space and the scattering pattern appears isotropic. In the case of crystallography, Equation (2) is still used to reconstruct the 3-D structure and for that purpose $A(\mathbf{q})$ has to be determined from the measured $S(\mathbf{q})$ by acquiring the missing phase information from another method, such as isomorphous replacement, anomalous scattering and molecular replacement. In the case of randomly oriented liquid, one has to deal with $S(\mathbf{q})$ and thus the tactics to overcome the phase problems in crystallography are not useful anymore. Instead, the theoretical $S(\mathbf{q})$ calculated from pair distribution functions based on a structural model has to be compared with the experimental $S(\mathbf{q})$ and the discrepancy between the experimental and theoretical $S(\mathbf{q})$ is minimised by optimising the structure model. This procedure can never guarantee finding a true global minimum, but fortunately prior knowledge about the system can usually guide us to the true solution.

### 2.4. *Scattering from a solution*

A liquid solution is a mixture of a minor component (solute) and a major component (solvent). Thus the total scattering from a solution can be classified into three types of

contributions: the scattering from the solute alone ($S(q)_{\text{solute}}$), the scattering from the solute–solvent interferences ($S(q)_{\text{cage}}$) and the scattering from the solvent alone ($S(q)_{\text{solvent}}$), and Equation (10) can be rewritten as follows by reclassifying the indexes $i$ and $j$ based on whether they belong only to solutes, solute–solvent or solvents.

$$S(q) = S(q)_{\text{solute}} + S(q)_{\text{cage}} + S(q)_{\text{solvent}}, \tag{11}$$

$$S(q)_{\text{solute}} = \sum_{i\ (\text{within solute})} N_i f_i^2(q) + \sum_{i\ (\text{within solute})} \sum_{i\neq j} \frac{N_i N_j}{V} f_i(q) f_j(q) \int_0^\infty (g_{ij}(r) - 1) \frac{\sin(qr)}{qr} 4\pi r^2 \mathrm{d}r, \tag{11a}$$

$$S(q)_{\text{cage}} = \sum_{i\ (\text{solute-solvent})} N_i f_i^2(q) + \sum_{i\ (\text{solute-solvent})} \sum_{i\neq j} \frac{N_i N_j}{V} f_i(q) f_j(q) \int_0^\infty (g_{ij}(r) - 1) \frac{\sin(qr)}{qr} 4\pi r^2 \mathrm{d}r, \tag{11b}$$

$$S(q)_{\text{solvent}} = \sum_{i\ (\text{within solvents})} N_i f_i^2(q) + \sum_{i\ (\text{within solvents})} \sum_{i\neq j} \frac{N_i N_j}{V} f_i(q) f_j(q) \int_0^\infty (g_{ij}(r) - 1) \times \frac{\sin(qr)}{qr} 4\pi r^2 \,\mathrm{d}r. \tag{11c}$$

The first is the scattering from the naked solute in vacuum, which equals the gas-phase scattering. The indices $i$ and $j$ run over only the atom types within the solute molecules. If the distance between the solute molecules is large enough, then the scattering from the interference between solutes can be ignored and the atoms within only one solute molecule can be considered. Therefore, this first term is easily calculated from atomic solute coordinates. For example, for $CHI_3$ dissolved in $CH_3OH$ at a concentration of 20 mM, the average distance between $CHI_3$ molecules is ~27 Å and thus this approximation holds. The second term is the scattering due to the cross interference between solute and solvent. This represents the structure of the solvent around the solutes; we call it the *cage term*. The index $i$ is for the atom types within the solute and the index $j$ is the atom types in the solvent. The last term is the scattering from the solvents alone and the indices $i$ and $j$ run over only the atom types within and between the solvent molecules. This term describes the structure of the bulk solvent which also depends on thermodynamic variables, such as temperature, pressure and density. As mentioned in Section 2.3, the $S(q)$ curve is easily calculated from the $g_{ij}(r)$ functions. In the same way, Equations (11a)–(11c) indicate that each term can be calculated from the $g_{ij}(r)$ functions as far as the indexes are well-classified. An example of $g_{ij}(r)$ and the corresponding scattering intensity $S(q)$ is shown in Figure 4 for $I_2$ in $CCl_4$. Figure 4(a) shows the solute-only term. In this case there is only one atom type, the I atom, and thus only the I···I pair needs to be considered. Due to the rigid structure of the $I_2$ molecule, $g_{\text{II}}(r)$ appears as a delta function at $r = 2.67$ Å. The solvent-only terms are shown in Figure 4(c). In $CCl_4$, there are two atom types, C and Cl, and thus three $g_{ij}(r)$ functions need to be considered; $g_{\text{CC}}(r)$, $g_{\text{CCl}}(r)$ and $g_{\text{ClCl}}(r)$. Figure 4(b) show the solute–solvent cross terms. Since there is only one atom type

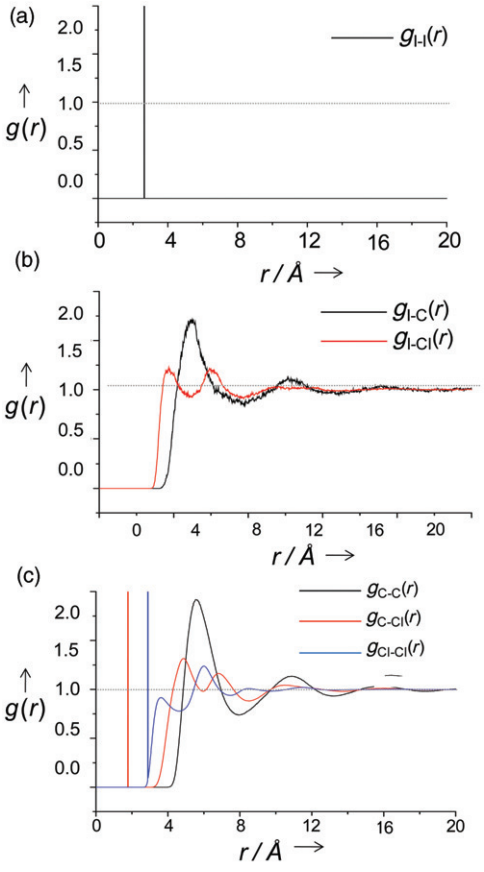


Figure 4. $g_{ij}(r)$ for the atom–atom pairs for $I_2$ in $CCl_4$: (a) $g_{ij}(r)$ for $I_2$ (solute-only term) (b) $g_{ij}(r)$ for the solute–solvent cross term and (c) $g_{ij}(r)$ for the solvent pairs C–C, C–Cl and Cl–Cl in $CCl_4$ (solvent-only term). The $g_{ij}(r)$s are calculated in equilibrium by MD simulation for one $I_2$ molecule in 256 $CCl_4$ molecules.



for the solute, I, and two atom types for the solvent (C and Cl), three $g_{ij}(r)$ functions need to be considered; $g_{CC}(r)$, $g_{IC}(r)$ and $g_{ICl}(r)$. The peak in $g_{ICl}(r)$ around 3.8 Å defines, in some sense, the radius of the $CCl_4$ cage around $I_2$.

### 2.5. *Time-resolved scattering*

In a time-resolved scattering experiment, a small portion of the whole sample is perturbed and it is thus the difference in the scattered intensity before and after the perturbation that contains the net signal. Here the difference intensity can be decomposed into three terms: the solute-only term, the solvent-only term and the cage term as in Equation (11) except that it is represented as a difference quantity.

$$\Delta S(q,t) = \Delta S(q,t)_{\text{solute}} + \Delta S(q,t)_{\text{cage}} + \Delta S(q,t)_{\text{solvent}}. \tag{12}$$

The first two terms ($\Delta S(q,t)_{\text{solute}} + \Delta S(q,t)_{\text{cage}}$) together can be considered as the solute-related term ($\Delta S(q,t)_{\text{solute-related}}$) and can be expressed as follows.

$$\Delta S(q,t)_{\text{solute}} + \Delta S(q,t)_{\text{cage}} = \Delta S(q,t)_{\text{solute-related}} = \frac{1}{R}\left[\sum_k c_k(t)S_k(q) - S_g(q)\sum_k c_k(0)\right], \tag{13}$$

where $k$ is the index of the solute (reactants, intermediates and products), $c_k(t)$ the fraction of molecules in $k$ as a function of time $t$, $S_k(q)$ the solute-related (the solute-only plus the cage components) scattering intensity of species $k$, $S_g(q)$ the scattering intensity of the reactants ($k =$ reactants), and $R$ is introduced to account for the ratio of the number of solvent molecules to that of solute molecules.

The $\Delta S(q,t)_{\text{solvent}}$ term in Equation (12) is very sensitive to the thermodynamic state of the bulk solvent, such as temperature, density and pressure, which may change during a chemical reaction due to energy transfer from light-absorbing solute molecules to the surrounding solvent molecules and the following relaxation to equilibrium with the environment around the scattering volume. In general, the temporal progression of the solvent response can be described as a linear combination of two independent thermodynamical parameters, arbitrarily chosen amongst density, temperature and pressure, pertaining to the photoinduced change. Initially (<5 ns), the energy transferred from the photoexcited solute heats the solvent and the temperature and pressure build up at constant volume and density. This process can be described by a solvent specific differential, $(\partial S(q)/\partial T)_\rho$. $(\partial S(q)/\partial T)_\rho$ is hereafter referred to as $(\partial S/\partial T)$. The scattering changes due to this term are mainly ascribed to the broadening of atom–atom distances in the solvent, constrained to a constant volume, by adiabatic heating at early times. By solving the hydrodynamic equations [89], it can be shown that for time delays sufficiently short $t < \tau_L = L/c$, where $\tau_L$ is the Longaker–Litvak time, $L$ is the laser beam size and $c$ the speed of sound in the liquid, the solvent is heated at constant volume, assuming that the laser beam size is smaller than the longitudinal dimension (i.e. parallel to the beam propagation) of the heated volume. In typical TRXL experiments, $c = 1143\ \text{m s}^{-1}$, $L \sim 50\ \mu\text{m}$, which leads to $\tau_L \sim 44$ ns. On longer timescales, 10–100 ns, the pressure relaxes causing expansion of the solvent and the solvent eventually returns to ambient pressure in typically 100 ns at a slightly elevated volume and temperature. Assuming local thermal equilibrium in the solvent, the change in the solvent scattering, at a given time delay $t$, is fully described by two hydrodynamic variables (e.g. temperature, $T$, and density, $\rho$):

$$\Delta S(q,t)_{\text{solvent}} = \left(\frac{\partial S}{\partial T}\right)_\rho \Delta T(t) + \left(\frac{\partial S}{\partial \rho}\right)_T \Delta\rho(t). \tag{14}$$

$\Delta T(t)$ and $\Delta\rho(t)$ represent the temperature change and density change at the time delay $t$ with respect to those before photoexcitation. The two differentials ($(\partial S/\partial T)_\rho$, and $(\partial S/\partial \rho)_T$) can be considered as time-independent components specific to the solvent. These can be calculated by MD simulations or via solvent-heating experiment. In the first case, three MD simulations are performed as a function of the thermodynamic variables $T$ and $\rho$. For example, two temperatures ($T_1$ and $T_2$) and densities ($\rho_1$ and $\rho_2$) are used where the densities are chosen such that the system is at the same pressure at $(T_1, \rho_1)$ and $(T_2, \rho_2)$.

Three MD simulations are run at the different thermodynamic conditions $(T_1, \rho_1)$, $(T_2, \rho_1)$ and $(T_2, \rho_2)$ and the MD trajectories are used to provide the solvent scattering intensity at three different conditions. Then, by taking the difference between the scattering in $(T_1, \rho_1)$ from that in $(T_2, \rho_1)$ and dividing by the temperature difference $(T_2 - T_1)$, the temperature differential at constant density $(\partial S/\partial T)_\rho$ is obtained. In the same way, subtracting the scattering intensity of system in $(T_2, \rho_2)$ from that in $(T_2, \rho_1)$ and dividing the density changes $(\rho_1 - \rho_2)$ provides the density differential at constant temperature $(\partial S/\partial \rho)_T$. The solvent differentials can also be obtained in a separate solvent-heating experiment. For example, the pure solvent is vibrationally excited with near-IR light, without inducing any structural change [90]. Since experimental solvent differentials probe the real solvent response with the pink X-ray spectrum used in the solute experiment, we usually get more reliable solute data with experimental solvent differentials rather than MD differentials. A more detailed discussion about how to get the experimental differential terms will be discussed in the section about the data analysis.

Combining Equations (12)–(14) gives us the master equation for the data analysis.

$$\Delta S(q,t) = \frac{1}{R}\left[\sum_k c_k(t) S_k(q) - S_g(q)\sum_k c_k(0)\right] + (\partial S/\partial T)_\rho \Delta T(t) + (\partial S/\partial \rho)_T \Delta\rho(t). \quad (15)$$



### 2.6. *Consideration for the polychromaticity and temporal profile of the X-ray pulse*

So far, we have considered the use of a perfectly monochromatic X-rays with only a single wavelength. In the third generation beamlines, we often use slightly polychromatic X-ray beams to speed up the data collection and thus the effect of the X-ray wavelength profile $P(\lambda)$ on the scattering intensity needs to be taken into account. Since the scattering intensity into a specific scattering angle $(2\theta)$ is contributed not by a single $\lambda$ but by a broad spectrum $P(\lambda)$, the scattering intensity has to be represented as a function of $2\theta$ rather than $q$. Once the theoretical curve for the monochromatic X-ray $(\Delta S(q)_{\text{mono}})$ is calculated via Equation (15), the theoretical difference scattering intensity considering the polychromaticity $(\Delta S(2\theta)_{\text{poly}})$ can be expressed as follows.

$$\Delta S(2\theta)_{\text{poly}} = \frac{\int S(q)_{\text{mono}} P(\lambda)\mathrm{d}\lambda}{\int P(\lambda)\mathrm{d}\lambda}. \quad (16)$$

After this correction, we often convert this scattering intensity to a function of $q$ using a representative wavelength. The choice of the representative wavelength is arbitrary, but the centre of mass or the peak of $P(\lambda)$ are reasonable choices.

We also need to consider the X-ray temporal profile when the time delay approaches the X-ray pulse length of about 100 ps. The difference curve considering this $(\Delta S(q,t)_{\text{time-average}})$ can be calculated by convoluting the theoretical difference curve $(\Delta S(q,t)_{\text{instant}})$ with the X-ray temporal profile $(I(t))$.

$$\Delta S(q,t)_{\text{time-average}} = \int_{-\infty}^{+\infty} I_X(\tau - t)\Delta S(q,\tau)_{\text{inst}}\,\mathrm{d}\tau. \quad (17)$$

If the processes of interest are slower than the X-ray pulse width (typically 100 ps), this step is not necessary.

## 3. Experiment: synchrotron-based pump-probe X-ray scattering

### 3.1. *Optical-pump and X-ray-scatter scheme*

In a typical TRXL experiment, an ultrashort optical laser pulse initiates the photochemistry of a solute in solution, and an ultrashort X-ray pulse from a synchrotron facility, instead of an ultrashort optical pulse used in the optical pump-probe experiment, is sent to the reacting volume to probe the structural dynamics inscribed in the TRXD signal as a function of time delay. TRXL data have been collected using an optical-pump and X-ray-probe diffractometer on beamline ID09B at ESRF [91,92] and beamline NW14A of PF-AR at KEK [93]. Beamline 14IDB at APS also has the capability of collecting TRXL data. The experimental setup is schematically illustrated in Figure 5. It comprises a closed capillary jet or open-liquid jet to supply the solution that are pumped by laser pulses and scatter X-rays, a pulsed laser system to excite the sample, a pulsed synchrotron source to produce picosecond X-ray pulses to scatter from the sample, a synchronised high-speed chopper that selects single X-ray pulses and an integrating charge-coupled device (CCD) area detector.

### 3.2. *Pulsed nature of synchrotron radiation*

Synchrotron radiation is described as the radiation from charged particles accelerated at relativistic velocities by classical relativistic electrodynamics. It provides excellent

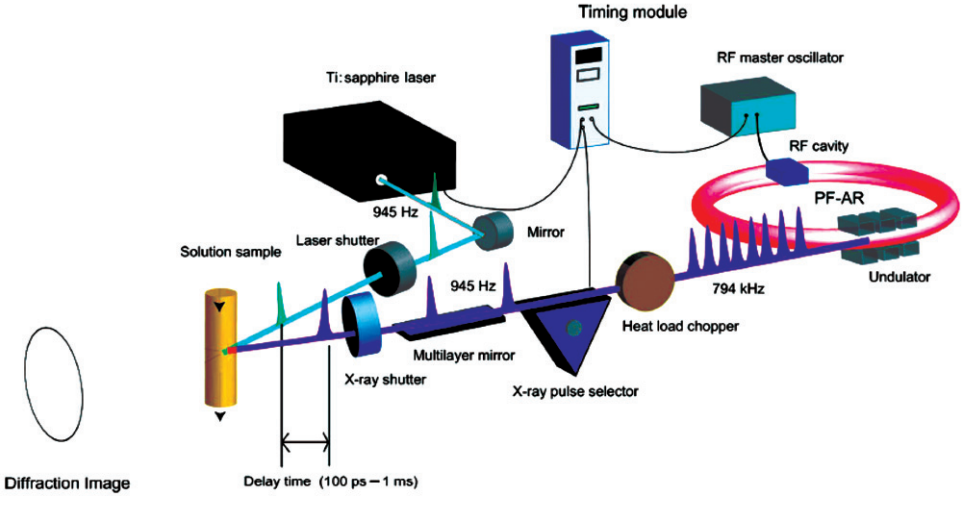


Figure 5. [Colour online] Schematic drawing of the experimental setup for TRXL. The liquid jet is irradiated by an optical laser pulse. After a well-defined time delay ($t$), the X-ray pulses from a synchrotron, selected by a high-speed chopper, are sent to the sample and scatter. The non-excited reference data collected at the negative time delay is subtracted from the diffraction data collected at positive time delays to extract the structural changes only.

characteristics as an X-ray source, such as small divergence, short wavelength and linear or circular polarisation. Synchrotron radiation has another useful feature for time-resolved X-ray technique, the short-pulsed nature, due to the periodic acceleration of charged particles in storage ring. Electrons circulating in storage ring irradiate synchrotron radiation and lose their energy. In order to compensate for the energy loss, a radio frequency (RF) oscillator accelerates electrons periodically at a harmonic frequency of the revolution frequency $f = c/L$, where $c$ is the speed of light and $L$ is the circumference of the storage ring. In order to keep electrons circulated stably in the storage ring, electrons need to pass through the RF oscillator at the appropriate timing, which is called the stable phase. Electrons stay and oscillate around the stable phase as a group, which is called the electron bunch. Due to this equilibration process, the length of the electron bunch is typically 1545 mm (rms), which corresponds to an X-ray pulse duration of 50–150 ps. Thus, the timing of the synchrotron X-ray pulse is synchronised to the timing of the RF oscillator. If the laser is externally triggered by the same RF master clock that accelerates the electrons, the laser and X-ray pulses can be synchronised to a short-term jitter of 1–3 ps (rms). The time resolution in pump-probe experiments with synchrotron light comes from controlling the pump-probe delay by synchronising both light sources to one master clock.



### 3.3. *X-ray source characteristics and isolation of a single X-ray pulse*

Synchrotrons are operated at pulse frequencies from MHz to GHz depending on the bunch-filling of the storage ring. In particular, time-resolved experiments at synchrotron facilities primarily require few bunch-filling modes of the storage ring, such as single-bunch or hybrid modes to facilitate the isolation of a single pulse with a mechanical chopper. In general, X-ray detectors have a relatively slow response time and, furthermore, two-dimensional (2-D) X-ray area detectors (e.g. CCD) have no fast gating capabilities. Due to this limitation of area detectors, the isolation of a single X-ray pulse from a pulse train is crucial for the success of time-resolved X-ray experiments. Since a single pulse is readily isolated by a fast chopper in suitable few bunch-filling modes, the operation in single-bunch or hybrid modes is highly desirable for time-resolved X-ray experiments.

The 6.5 GeV PF-AR storage ring is dedicated to single-bunch operation for about 5000 h/year. Electrons with a ring current of 60 mA (75.5 nC per bunch) are stored in a single electron bunch with a lifetime of about 20 h. The RF frequency of the PF-AR ring is 508.58 MHz, which is the 640th harmonic of the orbit frequency. Therefore, the X-ray pulses are delivered at a frequency of 794 kHz (=508.58 MHz/640) with a pulse duration of about 140 ps (FWHM). The beamline has two undulators with a period length of 20 mm (U20) and 36 mm (U36). The U20 gives the first harmonic in the energy range of 13–18 keV. The energy bandwidth of the first harmonic is $\Delta E/E = 15\%$, which can be used as a narrow-bandwidth pink beam for TRXL experiments. The U36 covers an energy range of 5–20 keV with first, third and fifth harmonics, which is useful for X-ray spectroscopy experiments.

In order to isolate a single X-ray pulse from the sources, a system of two choppers is installed on NW14A. The first chopper, the heat-load chopper, has an opening time of 15 μs, which isolates trains of 10 pulses at 945 Hz [61]. The second X-ray chopper, made by Forschungszentrum Jülich [94], consists of a rotor with a narrow channel for the beam passage. This high-speed chopper isolates a single X-ray pulse from the 10-pulse train.

The Jülich chopper realises continuous phase locking with timing jitter $<2$ ns. The opening time of the channel at the centre of the tapered aperture is 1.64 μs. If the repetition frequency of the pump-probe experiment is lower than 945 Hz, as for the 10-Hz YAG laser system on the beamline, a millisecond X-ray shutter (UNIBLITZ, XRS1S2P0) is inserted between the X-ray chopper and the sample.

### 3.4. *Energy bandwidth of the incident X-ray beam*

In order to gain maximum X-ray photon flux at 1 kHz, the energy bandwidth of the X-ray beam is a key issue. X-ray pulses with a 3% energy bandwidth from the first harmonics of the U17 undulator on beamline ID09B at ESRF have been used successfully for many TRXL experiments [40,63–77,79]. On the other hand, the undulator U20 on beamline NW14A on the PF-AR ring has a $\Delta E/E = 15\%$ energy bandwidth, due to relatively large electron beam emittance of PF-AR. In order to examine the feasibility of time-resolved liquidography with such a large bandwidth and to search for the optimal bandwidth, we simulated the Debye scattering curves for the reaction $C_2H_4I_2 \rightarrow C_2H_4I + I$ using (1) a 15% bandwidth with the default X-ray energy distribution, such as the undulator spectrum at the NW14A beamline, (2) a Gaussian spectrum with a 5% bandwidth, (3) a Gaussian spectrum with a 1% bandwidth and (4) a Gaussian spectrum with a 0.01% energy bandwidth, as shown in Figure 6.

Although the photon flux of X-ray pulse increases with the energy bandwidth, the simulation shows that the default 15% bandwidth X-ray spectrum with its long low-energy tail is unsuitable for the time-resolved liquidography owing to the smearing of the spatial resolution. Especially, the long tail of the U20 X-ray spectrum further blurs the scattering pattern at high scattering angles as compared to a symmetric Gaussian spectrum with the same bandwidth. As a result of the asymmetric lineshape, the X-ray spectrum with a long tail at ID09B of ESRF with a 3% bandwidth is effectively comparable to a symmetric Gaussian spectrum with a 10% bandwidth. In contrast, the scattering curve calculated from the Gaussian spectrum with a 5% energy bandwidth is similar to that from a 0.01%

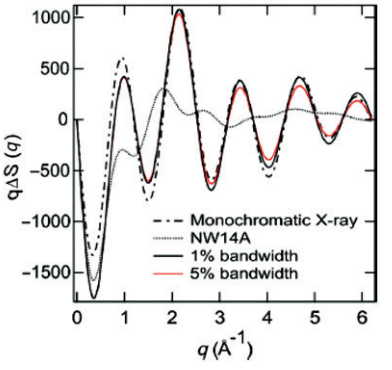


Figure 6. [Colour online] Debye scattering curves calculated for the model reaction $C_2H_4I_2 \rightarrow C_2H_4I + I$ using Gaussian X-ray energy profile: a 0.01% (monochromatic, dot-dashed line), a 5% (red solid line) and a 1% (solid line). Finally, the 15% (FWHM) asymmetric energy profile from the raw U20 undulator beam with its long tail (dotted line).

energy bandwidth (monochromatic) Gaussian spectrum. Furthermore, the total flux of the 5% energy bandwidth X-ray beam is higher, by a factor of 500, than that of the monochromatic X-ray beam (a 0.01% energy bandwidth) from a Si single crystal. These estimations clearly suggest that the X-ray pulses with $\Delta E/E$ of 5% is a very good compromise for TRXL, since it provides a strong scattering signal without sacrificing structural resolution. Thus, we reduced the bandwidth of the X-ray pulses from the default 15% to less than the 5% with a single-bounce multilayer in vacuum.

The multilayer optics on beamline NW14A can produce X-ray pulses with a 1–5% bandwidth, allowing us to measure TRXL with the U20 undulator on beamline NW14A. We used two types of multilayers. The first layer, made of $W/B_4C$ ($d = 27.7$ Å, X-ray Company, Russia) deposited on a Si single crystal with a size of $50 \times 50 \times 5\,mm^3$, provides an X-ray spectrum with a 1% energy bandwidth as shown in Figure 7(a). The peak energy of the X-ray spectrum can be changed by tilting the angle of the multilayer optics. The second multilayer, which is made of depth-graded Ru/C layer (average $d = 40$ Å, NTT Advanced Technology, Japan), produces a 5% energy bandwidth X-ray spectrum as shown in Figure 7(b). The white X-ray beam from the U20 undulator has a photon flux of $1 \times 10^9$ photons/pulse at 1 kHz. When multilayer optics with 1% and 5% energy bandwidths are used downstream the Jülich chopper, photon fluxes of $6 \times 10^7$ and $3 \times 10^8$ photons/pulse are obtained, respectively.

### 3.5. *Synchronisation of laser and X-ray pulses*

Beamline NW14A is equipped with a 150-fs Ti : sapphire regenerative amplifier laser system (Spectra Physics, Millenia, Tsunami, Spitfire, Empower). The Ti : sapphire laser system produces optical pulses at 800 nm at a 945-Hz repetition rate, with the pulse energy reaching up to 800 μJ/pulse . The laser is installed in a separate laser hutch next to the experimental hutch. An optical parametric amplifier (Light Conversion, TOPAS-C) is also installed in the laser hutch for the conversion of 800 nm light to a broad spectral range from visible to mid-IR. The laser beam is brought to the sample in the experimental hutch

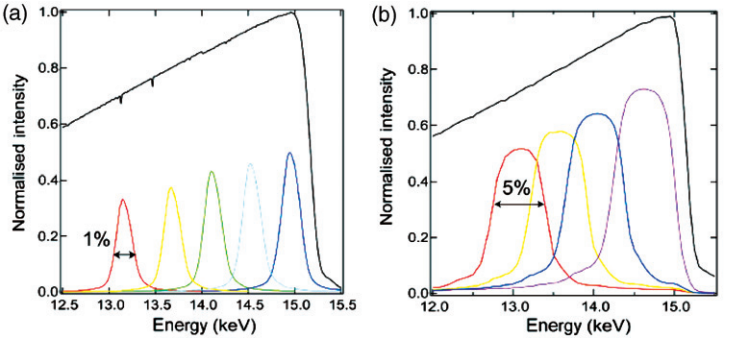


Figure 7. [Colour online] Broadband X-ray pulses were produced by multilayer optics from the undulator spectrum. The peak energy position is controlled by changing the incident angle. The black curve is the X-ray spectrum from the undulator U20 at a gap of 11 mm. (a) X-ray spectra from the $W/B_4C$ multilayer. The X-ray bandwidth is 1%. (b) X-ray spectra from the depth-graded Ru/C multilayer. The X-ray bandwidth is 5%.

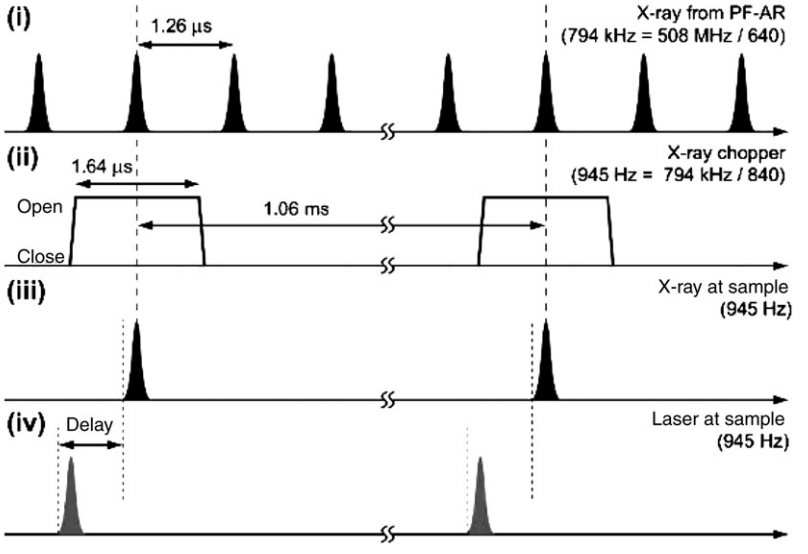


Figure 8. Timing chart for the synchronisation on beamline NW14A when using an X-ray chopper to synchronise the 794 kHz X-ray pulses from the storage ring and the 945 Hz laser pulses at a 1 : 1 ratio. Timing settings of the X-rays from (i) PF-AR, (ii) the X-ray chopper, (iii) the X-rays at the sample and (iv) the laser at the sample are shown.



through a beam duct. The synchronisation of the X-ray and laser pulses is based on the RF master clock that drives the electron bunch in the storage ring. When the X-ray experiment is conducted with a 945 Hz Ti:sapphire-laser and with a detector without gating capabilities (e.g. CCD), an X-ray chopper is required to synchronise the X-ray and laser pulses at a 1 : 1 ratio. The timing chart of the synchronisation is shown in Figure 8.

The X-ray pulse is emitted every 1.26 μs (794 kHz = 508 MHz/640) from the PF-AR ring. After the RF amplifier, the RF master clock signal of PF-AR is split into two major timing components: one for the laser system and the other for the X-ray chopper system. In the X-ray chopper system, the 508 MHz RF and the 794 kHz revolution signals are used as the clock and the reference signals, respectively. A 945 Hz (794 kHz/840) repetition frequency of the X-ray pulses is then selected to trigger the Ti:sapphire 150-fs laser system running at the same repetition frequency. In the laser system, the mode-locked Ti : sapphire oscillator operating at 85 MHz (508 MHz/6) synchronised with the X-ray pulses provides seed pulses to the regenerative amplifier. The seed pulses trigger the regenerative amplifier pumped by the Q-switched Nd:YLF laser at 945 Hz (85 MHz/89,600). Then, 945 Hz laser pulses are directed to the sample position by a series of mirrors. The pulse trains from the pumping laser and the probing X-ray pulses at the sample are shown in Figure 8. The timing of the delay between the two pulse trains is controlled by changing the ejection timing of the laser pulses from the regenerative amplifier using a phase shifter (Candox). The timing of the X-ray and the laser is measured with an InGaAs metal-semiconductor-metal (MSM) photodetector (Hamamatsu, G7096) coupled to a high-frequency preamplifier and a 2.5 GHz digital

oscilloscope (Tektronix, DPO7254). The rise time of the MSM photodetector is typically 40 ps, which is faster than the X-ray pulse duration, and the photodetector is set at the sample position.

### 3.6. *Spatial and temporal overlaps*

In order to increase the SNR of the TRXL data and to define accurate time delay between the laser and X-ray pulses, the laser and X-ray pulses have to be overlapped at the sample both spatially and temporally. To check the temporal overlap, we place a fast InGaAs detector at the sample position and record the time traces of the laser and X-ray pulses along a single time axis monitored by a 2.5 GHz digital oscilloscope. By adjusting the laser firing time, it is possible to adjust the relative timing between the two pulses to within a few picoseconds. During an experiment, the time traces of the laser and X-ray pulses are monitored by fast photodiodes simultaneously and non-intrusively.

The spatial overlap between X-ray and laser pulses is achieved using a 50 μm diameter pinhole placed at the sample position. The pinhole is located at the centre of X-ray beam, and then the laser beam is moved across the pinhole by scanning the position of the focussing lens until it passes through the centre of the pinhole. To ensure precise spatial overlap, we monitor the intensity of scattering induced by thermal expansion in a liquid solvent, which typically occurs in 1 μs with our beam sizes. Specifically, the ratio of scattered intensities in the inner and outer discs of the solvent signal is monitored. Once the sample expands, the solvent signal shifts to lower scattering angles, leading to the increase of low-angle scattering and the decrease of high-angle scattering. Therefore, the ratio between the inner and outer parts of the solvent signal changes in proportion with the laser excitation. The X-ray beam is typically vertically 200 μm and horizontally 250 μm. The laser spot is of circular shape with a diameter of 300–400 μm.

### 3.7. *Sample environment and data acquisition*

Two different sample cell systems have been used: dilute solutions of 0.5–100 mM concentration or pure solvents are prepared and circulated through either a capillary or through an open-jet sapphire nozzle. The open jet provides a stable flow with ~0.3 mm thickness at a speed ensuring the refreshment of the probe volume for every laser pulse (typically ~3 m/s). In the capillary-based system, the solution is flowed through a quartz capillary of 0.3 mm diameter. In the open-jet system, the capillary is removed and the solution is passed between two flat sapphire crystals with a spacing of 0.3 mm (Kyburz), which produces a stable naked liquid sheet directly exposed to the laser/X-ray beams. The open-jet system producing a bare liquid jet has the advantage over the closed capillary system in terms that the scattering background from the glass material is eliminated and thus the SNR substantially improves. The lower background also helps to enhance the accuracy of the normalisation process. In addition, the capillary jet often encounters a problem that the excitation laser drills a hole in the capillary.

The molecules in the jet are excited by laser pulses from the fs laser system described above. To maximise the population of transients and photoproducts, the laser pulse energy (typically 25–100 μJ depending on the excitation wavelength) is set to be relatively higher than that used in typical time-resolved optical spectroscopy, and thus multi-photon

excitation often occurs. In general, one wants to follow photochemistry induced by only one-photon absorption that the laser pulse duration of ~100 fs is stretched to ~2 ps by introducing positive chirp from a pair of fused-silica prisms inserted before the sample. To probe slow photoinduced dynamics, a nanosecond laser is used instead of the fs laser.

The laser beam is generally directed to the sample with a 10-degree tilt angle relative to the X-ray beam. The scattered X-ray diffraction signal is recorded by an area detector (MarCCD165, Rayonics, $2048 \times 2048$, ~80 μm effective pixel size) with a sample-to-detector distance of ~45 mm. A typical exposure time is ~5 s, and, given the ~1 kHz repetition rate of the laser/X-ray pulses, the detector receives $5 \times 10^3$ X-ray pulses and $\sim 5 \times 10^{12}$ X-ray photons per image. Diffraction data are collected for typically 10 or more time delays ($t$) from −100 ps up to 1 μs (for example, −100 ps, 0 ps, 30 ps, 100 ps, 300 ps, 1 ns, 3 ns, 10 ns, 30 ns, 100 ns, 300 ns and 1 μs). Each time delay is interleaved by a measurement of the unperturbed sample (typically at −3 ns).



### 3.8. *Solvent-heating experiment to obtain experimental $(\partial S/\partial T)_\rho$, and $(\partial S/\partial \rho)_T$ of solvent*

The two solvent differentials, $(\partial S/\partial T)_\rho$ and $(\partial S/\partial \rho)_T$, are needed in the data analysis to account for the response of the solvent to changes in temperature and density during the reactions. As discussed in Section 2.5, these can be obtained from either MD simulations or solvent-heating experiment. Due to this complexity, fingerprinting the molecules in action would not be possible were it not aided by theory. MD simulation can simulate statistical atom–atom correlation functions $g_{\alpha\beta}(r)$ for a solution.[95,96]. These simulations are indispensable for disentangling the different contributions in the scattering patterns, and they have proved quite accurate in reproducing measured signals. However, numerous factors influence the accuracy of these simulations. First of all, theoretical potentials define trajectories on which molecules evolve; hence, the structure determination may depend on the type of potential used. Certain force fields are difficult to model efficiently: the most well-known example is the force fields associated with hydrogen bonds (methanol, water, etc.). The simulations are run on a finite ensemble of molecules, which define the simulation box size, thus putting a constraint on the lowest $q$ and on the real space analysis. For these reasons, it is desirable to obtain the solvent-only term experimentally. Armed with experimental solvent differentials, one can in principle subtract the solvent contribution and deduce the structure of the caged solutes during the reaction. In the solvent-heating experiment, the solvent is heated with either near-IR light via vibrational excitation or with UV light via two-photon process. In the first case, no chemical reaction occurs in the solvent molecules, but only the vibrational modes are excited, thereby eventually depositing heat. In the latter case, the solvent molecules may undergo irreversible reactions, but as far as the relative portion of the irreversible reaction is small enough, this method is still useful. An alternative method to deposit heat to the sample is to dissolve dye molecules and excite the solution with visible light. In this case, the dye molecule absorbs the light and the photon energy is transferred to the solvent. Here we describe a more detailed experimental procedure for the case with the near-IR light.

The key idea is that the near-IR pulses excite overtones of O–H and $CH_3$ vibrations in liquid methanol, and in doing so, they deposit heat without inducing any chemical change.

It can be shown that for neat liquids, the time needed to reach a uniform temperature in a typical experiment is less than 100 ps (see below). This fact justifies the use of hydrodynamics equations for time delays larger than 100 ps; these equations show that at early time delays, the volume and the density of the solvent do not change, and consequently only the effective temperature (and pressure) of the solvent rises [97]. The laser-induced change is obtained by subtracting the non-excited scattering, measured at a negative time delay, from the scattering at a very short time delay ~100 ps. This gives the change in the diffraction intensity due to a temperature change at constant density, $(\partial S/\partial T)_\rho$, where $S$ stands for the diffraction intensity, $T$ the temperature and $\rho$ the density [95]. At later time delays, pressure relaxation, being faster than the thermal one, drives the system into a configuration of a hot solvent at ambient pressure, i.e. thermal expansion. The difference between the diffracted intensity at a late time delay yields the constant pressure term, $(\partial S/\partial T)_P$, where $P$ stands for the pressure. By combining the two terms $(\partial S/\partial T)_\rho$ and $(\partial S/\partial T)_P$, one can get the principal differentials $(\partial S/\partial T)_\rho$ and $(\partial S/\partial \rho)_T$ (see later). Since the $(\partial S/\partial T)_P$ term for pure methanol is necessary for a proper absolute scaling of the experimental differentials obtained from the NIR experiment, a series of separate measurements were conducted on pure methanol as follows. A monochromatic X-ray beam at 26 keV was sent through liquid methanol contained in a sample cell designed for stable temperature control. The diffraction data were taken at four different temperatures; 15.0°C, 17.5°C, 20.0°C and 22.5°C.

The presence of only two components in the solvent response has been verified using the singular value decomposition (SVD) method [58,98], which showed only two significant singular vectors. The SVD analysis showed unequivocally the reliability of the data and the data reduction routines. After extremely fast vibrational cooling of methanol, well below 10 ps, the response of the solvent is entirely due to hydrodynamics. Therefore, it is relatively easy to determine the derivatives in Equation (14), by measuring the response at two time delays only. For this reason, we collected, with greatly enhanced statistics, diffraction patterns at 100 ps and 1 μs. The 100 ps data is essentially identical to $(\partial S/\partial T)_\rho$ multiplied by the temperature rise at this early stage of heating at constant volume, hence the second term contributing net zero. At 1 μs, the liquid returns to ambient pressure. Therefore, the 1 μs data equals $(\partial S/\partial T)_P$ multiplied by the temperature rise at 1 μs. The temperature rise at 1 μs was estimated to be 1.50 K by scaling the 1 μs data to $(\partial S/\partial T)_P$ determined experimentally from a series of static measurements at various temperatures. At 1 μs, the solvent is still hot, yet its temperature has lowered from the temperature at 100 ps by the ratio $C_V/C_P$ due to expansion. Therefore, the temperature rise at 100 ps is 1.76 K and the experimental $(\partial S/\partial T)_\rho$ can be obtained by dividing 100 ps data by this number. $\Delta\rho$ at 1 μs can be calculated to be $-1.77\,\mathrm{kg/m^3}$ from the known isobaric thermal expansion coefficient of $1.49 \times 10^{-3}\,\mathrm{K^{-1}}$. The equation of state (Equation 14) for the liquid at 1 μs can be rewritten as

$$\left(\frac{\partial S}{\partial \rho}\right)_T \Delta\rho = \Delta S(1\,\mu\mathrm{s}) - \frac{C_V}{C_P}\Delta S(100\,\mathrm{ps}). \tag{18}$$

Then the experimental $(\partial S/\partial \rho)_T$ is obtained from Equation (18).

The concentration of the methanol molecules that absorb the NIR and contribute to the heating was estimated to 40 mM by considering the temperature change. As the concentration of pure methanol at ambient conditions is 24.7 M, this corresponds to

exciting 1 out of 618 molecules. The total energy deposited to the irradiated volume is estimated to be ~9 μJ/pulse by considering the total volume exposed to the NIR laser pulse. The validity of classical hydrodynamics assumes a homogeneous and isotropic sample; thus, it is important to estimate the time it takes to smooth out the memory of time zero, which can be described as a collection of hot points in the liquid. To estimate this thermalisation time, we note that the average distance between excited methanol molecules, at the observed 40 mM concentration, is 21.5 Å if the volume per excited solute is approximated by a sphere. Following the classical thermal diffusion theory developed by Landau and Lifshitz, a hot point in a liquid cools down in time and space following the equation:

$$T(r,t) \propto \frac{1}{8(\pi\chi t)}\exp(-r^2/(4\chi t)) \tag{19}$$

with

$$\chi = \frac{\kappa}{\rho C_V}. \tag{20}$$

Here $\chi$ is the thermometric conductivity and $\kappa$ the thermal conductivity. Note that the space dependence is contained in the exponential and that the position of the mid-point in the space distribution moves as

$$r_{50\%}(t) = 2\ \ln 2\sqrt{\chi t}. \tag{21}$$

The parameters for methanol are $\rho = 791\ \mathrm{kg/m^3}$, $C_V = 2151\ \mathrm{J/K/kg}$, $\kappa = 0.21\ \mathrm{J/s/m/K}$, and $\chi = 1.2345\ 10^{-7}\ \mathrm{m^2/s}$. From Equation (21), we deduce that it takes 13.5 ps, on average, for two neighbouring spherical thermal waves to meet, which is the criteria for local thermal homogeneity. As the scattering data presented here are ensemble averaged by our 100 ps long X-ray pulse, it is justified to use classical hydrodynamics in this study. In future, experiments with pulsed X-ray lasers (XFEL) with 100 fs X-ray pulses, the earliest time delays will show the signature from the cooling of hot points.



## 4. Data processing and analysis for small-molecule solutions with 100 ps time resolution

### 4.1. *Conversion of 2-D images into 1-D curves*

After data collection, the 2D diffraction images are azimuthally integrated into 1-D intensity curve, $S(q,t)$, as a function of the momentum transfer $q$. The programme suite FIT2D [99] is highly useful in this regard and the correction to account for the flat detector screen is included in this step. The 1-D $S(q,t)$ curves are then corrected for the scattering angle-dependent absorption in the phosphor screen in the CCD where X-ray photons are converted to visible light photons. The X-rays are more efficiently converted to visible light signal at high angles as the optical path in the phosphor scales as $1/\cos(2\theta)$ for a flat screen, where $2\theta$ is the scattering angle. Without this correction, the signal amplitudes at high angles would have been artificially strong. We also need to consider the correction for the scattering angle-dependent X-ray absorption due to the liquid sample.

In order to visualise the very small laser-induced scattering changes ($\Delta S/S < 0.2\%$), difference scattering curves are generated by subtracting laser-on from laser-off images. Given the weak laser-induced change in the total scattering, the images are subject to

judicious normalisation prior to subtraction. Firstly, we scale the exposure time to compensate for the decrease in intensity of the incoming X-ray beam, due to the decaying bunch charge of the electrons circulating in the synchrotron ring. This ensures that equivalent images are exposed to the same level, which reduces the effect from non-linear response in the CCD detector. Secondly, the fast transfer of heat from excited molecules to the bulk forces the solution to expand. The expansion takes place on a timescale determined by the time it takes for sounds waves to traverse the laser illuminated volume. In fast reactions and with current beam sizes $\sim$100 μm, the expansion happens between 10 and 100 ns [95]. This means that the number of molecules is generally different in laser-off and laser-on images. To correct for these effects, we use the recorded image itself as a monitor of the incoming X-ray intensity, and the density of scattering centres (atoms). Specifically, we use a small interval around an isosbestic point $q_0$ in the high-$q$ part of the spectrum as the normalisation range. The radial intensity is then divided by the integral count in this interval. The definition of an isosbestic point is that the intensity at that particular $q$ value is constant regardless of time delay. An initial candidate $q_0$ can be initially located from theoretical difference curves, and further refined using a simple iterative procedure. Starting with a relatively broad interval around the initial $q_0$ ($q_0 > 7\,\text{Å}^{-1}$, $\Delta q \sim 1.5\,\text{Å}^{-1}$), the procedure checks for nodal points in the difference curves in the chosen range around $q_0$; the procedure is reiterated by changing the central point $q_0$ until the nodal point, $q_0$, is well-defined, i.e. until $q_0$ becomes an isosbestic point. Usually, after 2–3 repetitions $q_0$ converges to a value within $0.02\,\text{Å}^{-1}$ spread, and it becomes insensitive to the normalisation interval (typical value used $\sim 0.6\,\text{Å}^{-1}$). Changing $q_0$ by $0.02$–$0.05\,\text{Å}^{-1}$ around the optimal value does not change the difference maps appreciably.

After normalisation, the associated curves are subtracted to give difference curves and averaged. The diffraction data for the unperturbed sample measured at a negative time delay (typically at $-3$ ns) is subtracted from the diffraction data collected at positive time delays to extract the diffraction change only. The difference diffraction intensities $\Delta S(q, t)$ contain direct information on the structural changes of the solute and solvent in the probed solution. The relative laser induced diffraction signal change $\Delta S/S$ is quite small. It depends on both time and scattering angle, and is typically less than 0.1%. Standard deviations (SDs) as a function of $q$ are calculated in the process of conversion from a 2-D image to a 1-D curve by taking into account the distribution of the intensities at the same $q$ value. The error of the averaged $\Delta S(q, t)$ can be obtained from the error propagation of SDs or by taking another standard deviation from the mean value of individual difference curves. The SNR of a typical $\Delta S(q, t)$ depends on $q$ and $t$ and oscillates resembling the shape of $\Delta S(q, t)$ except that the negative values of $\Delta S(q, t)$ become positive in the plot of SNR. A typical averaged $\Delta S(q, t)$ from about 50–100 repetitions has a SNR up to 15. The SNR is zero when $\Delta S$ is zero and reaches a maxima in the peaks and valleys of $\Delta S(q, t)$. To magnify the oscillatory feature at high $q$, $\Delta S(q, t)$ is often multiplied by $q$ to yield $q\Delta S(q, t)$.

Due to the presence of background scattering, i.e. air and capillary when used, direct subtraction introduces spurious effects. In fact, the density of the solution being time dependent (i.e. for time delays beyond 10 ns [96,100]), the ratio of scattered intensity from the sample and the background becomes time dependent. In a typical experiment, the relative density change is $\sim$0.3%. This effect is readily corrected under the assumption that the total scattering is a sum of sample and background scattering and that the density

change is known. The first assumption implies that the background scattering can be measured reliably by simply removing the sample (leaving the empty capillary, when used). As far as the density change is concerned, an iterative procedure will provide the right value as follows. In the first step, this correction is neglected and $\Delta\rho$ is estimated using the real-space Fourier transform of the data, scaled to absolute units (see below), in the $r \to 0$ limit [95]. This $\Delta\rho$ is an initial value used in the following equation, the output of which generates a corrected difference curve [90].

$$\Delta S_S = \frac{1+\alpha/\beta}{1+\alpha}\left\{\Delta S_M + \frac{1-\beta}{\beta+\alpha}\left[\alpha S^{off}_{sample} - S_{back}\right]\right\}, \tag{22}$$

where $\alpha$ is the fractional intensity from the background at $q_0$, $\beta = 1 + \Delta\rho/\rho$, $\Delta S_M$ the uncorrected difference curve, $S^{off}_{sample}$ the scattering intensity of the solution alone without laser and $S_{back}$ the background scattering. Three or four reiterations of the procedure are enough to yield a satisfactory result. The effect of this correction can be considerable for time delays after around 50 ns when the capillary sample system is used, but is generally very small for data collected with a bare liquid jet.

Although $q\Delta S(q,t)$ contains direct information on the structural changes, often the result in reciprocal space is not intuitive. For this reason, $q\Delta S(q,t)$ is transformed to real space where the changes are more readily interpretable: positive and negative peaks mean formation and depletion, respectively, of the corresponding interatomic distance. Obtained through sine-Fourier transforms of $q\Delta S(q,t)$, the difference radial distribution function ($r\Delta R(r,t)$) represents the experimental atom–atom pair distribution function during the course of the reaction.

$$r\Delta R(r,t) = \frac{1}{2\pi^2}\int_0^\infty q\Delta S(q,t)\sin(qr)e^{-q^2\alpha}\,dq, \tag{23}$$

where the constant $\alpha$ is a damping constant to account for the finite experimental $q$ range. In principle, the errors in the $r$-space can also be obtained from the same procedure as the one described for the $q$-space data: The sine-Fourier transform of every single $q\Delta S(q,t)$ is taken and then averaged over all $r\Delta R(r,t)$ curves, which defines a meaningful standard deviation. We note that conventionally $r\Delta R(r,t)$ is also denoted as $r\Delta S(r,t)$ or $r\Delta S[r,t]$ in the literature.



### 4.2. *Data analysis*

The goal of the data analysis is to extract kinetic and structural information from the measured difference intensities ($\Delta S(q,t)^{exp}$). For this, we need to explain and reproduce the experimental data in terms of theoretical data. The theoretical difference intensities are calculated using Equation (15), repeated here.

$$\Delta S(q,t) = \frac{1}{R}\left[\sum_k c_k(t)S_k(q) - S_g(q)\sum_k c_k(0)\right] + (\partial S/\partial T)_\rho \Delta T(t) + (\partial S/\partial\rho)_T \Delta\rho(t).$$

The polychromacity of the X-ray beam has to be taken into account when a $\Delta S(q,t)^{theory}$ curve is compared with the $\Delta S(q,t)^{exp}$ curve by weighting the X-ray spectrum into the $\Delta S(q,t)^{theory}$ curve. The equation indicates that, to calculate $\Delta S(q,t)^{theory}$, two

types of basis components are needed: time-independent functions, such as $S_k(q)$, $(\partial S(q)/\partial T)_\rho$ and $(\partial S(q)/\partial \rho)_T$ and time-dependent functions, such as $c_k(t)$, $\Delta T(t)$ and $\Delta\rho(t)$. In the following, the steps involved in the calculation of time-independent and time-independent basis functions are described with the photochemistry of $CHI_3$ in $CH_3OH$ as an example.

$S_k(q)$ are calculated from MD simulations combined with quantum calculations of the candidate solute structures. The possible structures of the parent molecule, the transient intermediates and the products in solution are provided by fully optimising the molecular geometry with the *ab initio* and/or density functional theory (DFT) methods with solvent effects included. In the case of the photochemistry of $CHI_3$ in $CH_3OH$, the molecular structures of all putative species, such as $CHI_3$, $CHI_2$, $CHI_2$–I isomer, $I_2$, I and $CH_3OH$ are calculated. The charges on the atoms of all the related species are also calculated via the natural bond orbital analysis. These structures and charges are used as starting points for the MD simulations, where one solute molecule is placed in a box containing 512 or more rigid solvent molecules. After the MD simulations, the pair correlation functions $g_{ij}(r)$ for the atom-type pair $i$ and $j$ are calculated. The $S_k(q)$ curves are then computed by Equation (10), repeated here.

$$S(q) = \sum_i N_i f_i^2(q) + \sum_i \sum_{i \neq j} \frac{N_i N_j}{V} f_i(q) f_j(q) \int_0^\infty (g_{ij}(r) - 1) \frac{\sin(qr)}{qr} 4\pi r^2 \, \mathrm{d}r.$$

Including $g_{ij}(r)$ for only the pairs within the solute molecule (e.g. $CHI_2$–I isomer has one type of C···H, three types of C···I, three types of H···I and three types of I···I) results in the solute-only term, which can be also described by Debye scattering of isolated solute molecules as in the gas phase. The cage term is calculated when $g_{ij}(r)$ for the solvent–solute cross pairs (e.g. the $CHI_2$ radical in $CH_3OH$ has $C_{solute}\cdots C_{solvent}$, $C_{solute}\cdots O$, I···$C_{solvent}$, and I···O, and many other pairs including H) are used in the integration. In practice, $g_{ij}(r)$ for both solute-only and solute–solvent cross pairs are used to yield the solute-only plus cage terms, i.e. the solute-related terms, $S_k(q)$. The solvent differential functions, $(\partial S(q)/\partial T)_\rho$ and $(\partial S(q)/\partial \rho)_T$, can be obtained either from MD simulations or determined in a separate experiment where the pure solvent is vibrationally excited by near-IR light [66]. The latter gives superior agreement than the former. In general, the $g_{ij}(r)$ from MD for a particular atom pairs $\alpha$ and $\beta$ can be used to calculate the contribution from that particular atom–atom pair to the overall signal, thereby aiding the peak assignment (e.g. the atom pair of I and O gives the I···O interatomic contribution, which is one of the major solute–solvent cross terms).

Once all the necessary components are ready, the least-squares method is used to fit the experimental difference intensities $(\Delta S(q,t)^{\mathrm{exp}})$ against theoretical difference intensities $(\Delta S(q,t)^{\mathrm{theory}})$. Here, one can consider two options. The first one is to fit a single difference curve at a time delay separately one by one (simple fitting analysis). The other is to fit all the difference curves for all time delays simultaneously with a set of common fitting parameters (global fitting analysis). In both cases, the chi-square ($\chi^2$) is minimised by optimising a set of fitting parameters. In the simple fitting case, the $\chi^2$ is defined as follows.

$$\chi^2 = \sum_q \left( \frac{(\Delta S^{\mathrm{theory}}(q,t) - \Delta S^{\mathrm{exp}}(q,t))}{\sigma_{q,t}} \right)^2, \tag{24}$$

where $\sigma_{q,t}$ is the $q$-dependent SD of $\Delta S(q,t)^{\exp}$. Here the fitting parameters are $c_k(t)$, $\Delta T(t)$ and $\Delta\rho(t)$ and can include structural parameters affecting $S_k(q)$. After fitting the curve at each time point, the fitted $c_k(t)$, $\Delta T(t)$ and $\Delta\rho(t)$ can be plotted as a function of time, yielding the population change of the solute species, and the time-dependent change of the solvent temperature and density. Although this simple fitting analysis is useful in the early stage of the data analysis, it also has the following problem. In the simple fitting analysis, $c_k(t)$, $\Delta T(t)$ and $\Delta\rho(t)$ are independent of one another, and there is no mathematical connection among them. In reality, they are quantitatively linked obeying energy and mass conservation. Depending on how the population of the solute species change, the heat from the solutes is transferred to the solvent, and it changes the solvent temperature and density accordingly. In addition, in this approach the number of fitting parameters increases linearly with the number of available experimental time delays. To account for the connectivity among $c_k(t)$, $\Delta T(t)$ and $\Delta\rho(t)$ and to reduce the number of fitting parameters, we use global fitting analysis, where theoretical difference curves are fitted at *all* time delays rather than at one time delay at a time. In this case, the $\chi^2$ is defined as a sum of the $\chi^2$ at all times.

$$\chi^2 = \sum_t \chi_t^2 = \sum_t \sum_q \left( \frac{(\Delta S^{\text{theory}}(q,t) - \Delta S^{\exp}(q,t))}{\sigma_{q,t}} \right)^2. \tag{25}$$

Figure 9 presents an overall scheme for the global fitting analysis. A set of differential equations for the population of species is considered and solving the rate equations yields the theoretical $c_k(t)$, then the time-dependent heat into the solvent, $Q(t)$, when the energy levels of each species usually estimated from DFT calculations are considered as follows.

$$\begin{aligned} Q(t) &= \text{Energy}(t=0) - \text{Energy}(t) \\ &= \frac{N_a}{R}\left[\sum_k (E_g + h\nu)c_k(0) - \sum_k E_k c_k(t)\right] + \frac{N_a}{R} f_{\text{fast}}[1 - \exp(-t/k_{\text{fast}})], \end{aligned} \tag{26}$$

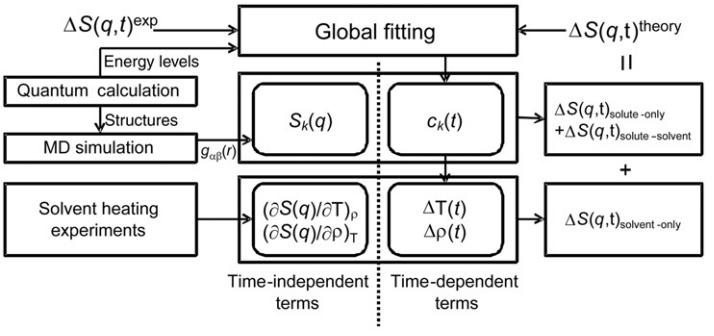


Figure 9. Schematic representation of the data analysis. A theoretical difference scattering curve is represented as a sum of the three terms contributions: the solute-only term, the solute–solvent cross-term and the solvent-only term. The discrepancy between the theory and experiment is minimised in global fitting analysis by considering data at all positive time delays simultaneously. See the text for details.

where $N_a$ is the Avogadro's number, $R$ the ratio of the number of solvent molecules per solute, $E_g$ (J/mol) the absolute energy of the parent (ground-state) molecule, $h\nu$ the excitation energy and $E_k$ (J/mol) the energy of species $k$. The symbol $f_{fast}$ is to denote the fraction of rapid relaxed species, and $k_{fast}$ ($s^{-1}$) the rate constant for vibrational cooling which occurs faster than the temporal resolution of TRXL (~100 ps). $Q(t)$ can be used to calculate the change in temperature ($\Delta T(t)$) and density ($\Delta\rho(t)$) as a function of time via hydrodynamics relations [89,101].

One can see that rate coefficients for the rate equations determine $c_k(t)$, $\Delta T(t)$ and $\Delta\rho(t)$ and thus these terms are mathematically connected rather than being independent. The fitting parameters include the rate coefficients, the fraction of the excited molecules, the fraction of the molecules undergoing structural changes and the laser beam size. Structural parameters, such as bond lengths and angles and energy levels of chemical species can be included as fitting parameters.

### 4.3. *Example: photochemistry of $CHI_3$*

A result of global fitting analysis for $CHI_3$ is shown in Figure 10. The time-dependent basis functions ($c_k(t)$, $\Delta T(t)$ and $\Delta\rho(t)$) depend on the fitting parameters from the global fitting analysis. A set of rate equations for a reaction kinetic model including all reasonable candidate reaction pathways is set up to determine the reaction mechanism. As a candidate reaction model for $CHI_3$, the rate constants for dissociation ($CHI_3 \rightarrow CHI_2 + I$), geminate and non-geminate recombination ($CHI_2 + I \rightarrow CHI_3$), and the non-geminate formation of molecular iodine ($I + I \rightarrow I_2$) can be considered. Integrating the rate equations provides $c_k(t)$ to be used to construct the theoretical scattering signal. The $\Delta T(t)$ and $\Delta\rho(t)$ are mathematically linked to $c_k(t)$ and to each other by energy and mass conservation and hydrodynamics. From $c_k(t)$, the time-dependent heat released from solutes to the solvent, $Q(t)$, is calculated and used to compute $\Delta T(t)$ and $\Delta\rho(t)$ via thermodynamic and hydrodynamics relations [102].

Figure 10(a) shows a comparison of $q\Delta S(q,t)^{exp}$ and $q\Delta S(q,t)^{theory}$ from global fitting analysis of TRXL data of $CHI_3$ in $CH_3OH$, and Figure 10(b) shows the corresponding $r\Delta R(r,t)^{exp}$ and $r\Delta R(r,t)^{theory}$. Figure 10(e) summarises the final fit values. Upon irradiation of 20 mM iodoform in methanol, 24(±1)% of the solute molecules are excited by the laser pulse at 267 nm. Among the excited iodoform, 28(±1)% dissociate into $CHI_2 + I$ within the time resolution of 100 ps, and the remaining 72(±1)% decay into the ground state via vibrational cooling and release their energy to the solvent. The iodine atoms recombine to form $I_2$ with the bimolecular rate constant of $1.55(\pm0.25) \times 10^{10}\,M^{-1}\,s^{-1}$. Based on these values from global fitting analysis, chemical population changes (as shown in Figure 10c) and the temperature and density change of the solvent (as shown in Figure 10d) as a function of time can be drawn. Initially, the temperature and the pressure of the solvent increase at a constant volume due to the energy transfer from the solute to solvent. Then, the thermal expansion occurs with a time constant of ~50 ns, returning the sample to ambient pressure. Due to the thermal expansion, the density of the solvent decreases by $1.2\,kg/m^3$ (0.15%) at 1 μs, leading to a temperature increase of 1.02 K. After the analysis, the whole signal can be decomposed into each component. For example, the solute-only term, the cage term and the solvent-only term in real space are shown in Figure 11(d–f) along with the assignment of the peaks in the real space.

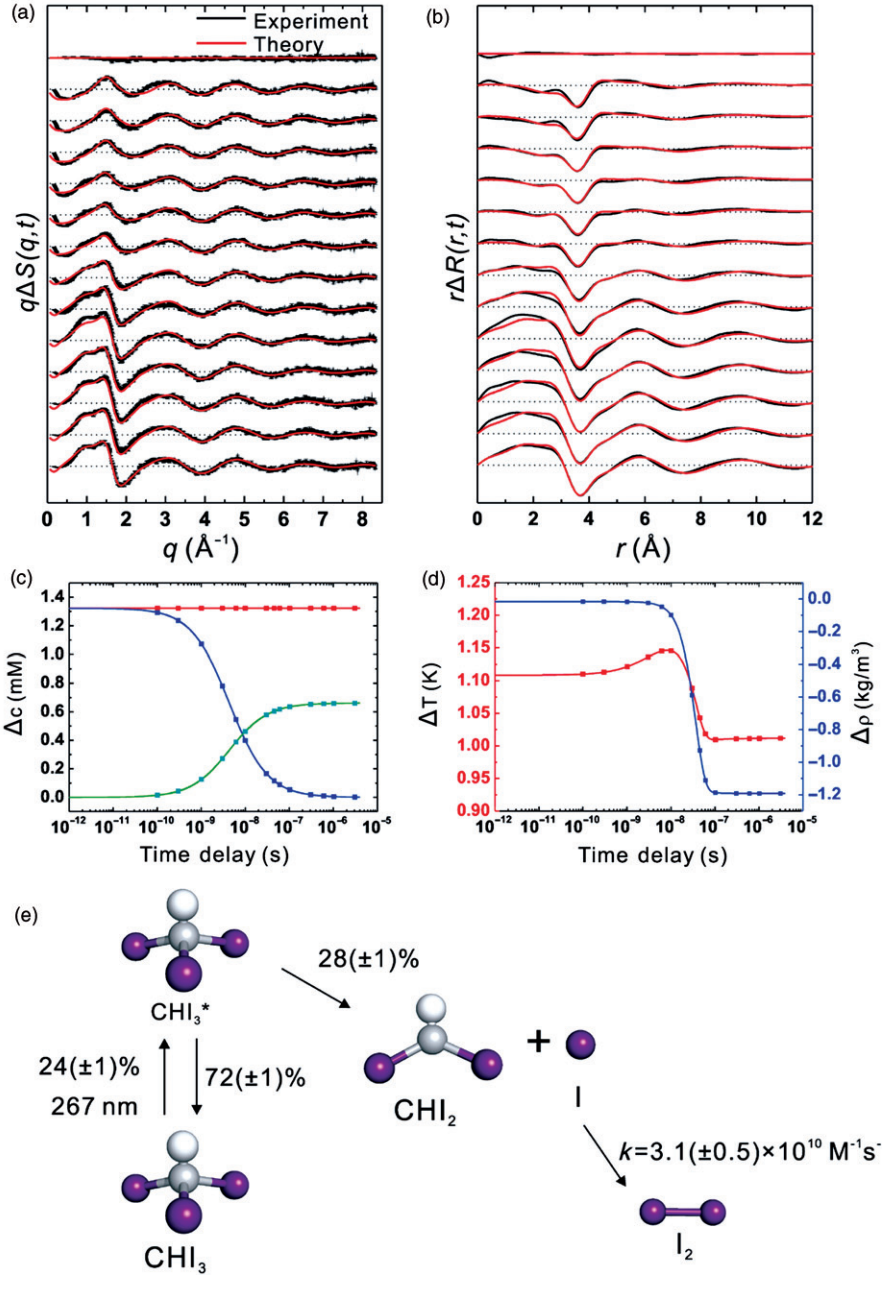


Figure 10. [Colour online] Structural dynamics of the photochemistry of $CHI_3$ in methanol upon photolysis at 267 nm determined by TRXL. (a) Experimental difference diffraction intensities, $q\Delta S(q, t)$ (black) and theoretical curves (red) as a result of global fitting analysis. (b) Difference radial distribution curves, $r\Delta R(r, t)$, corresponding to (a). (c) The population changes of the various chemical species as a function of time delay determined from global fitting analysis. (d) The change in the solvent density (red) and temperature (blue) determined from global fitting analysis. (e) A reaction mechanism determined by TRXL.
Source: Adapted and modified from Ref. [72].

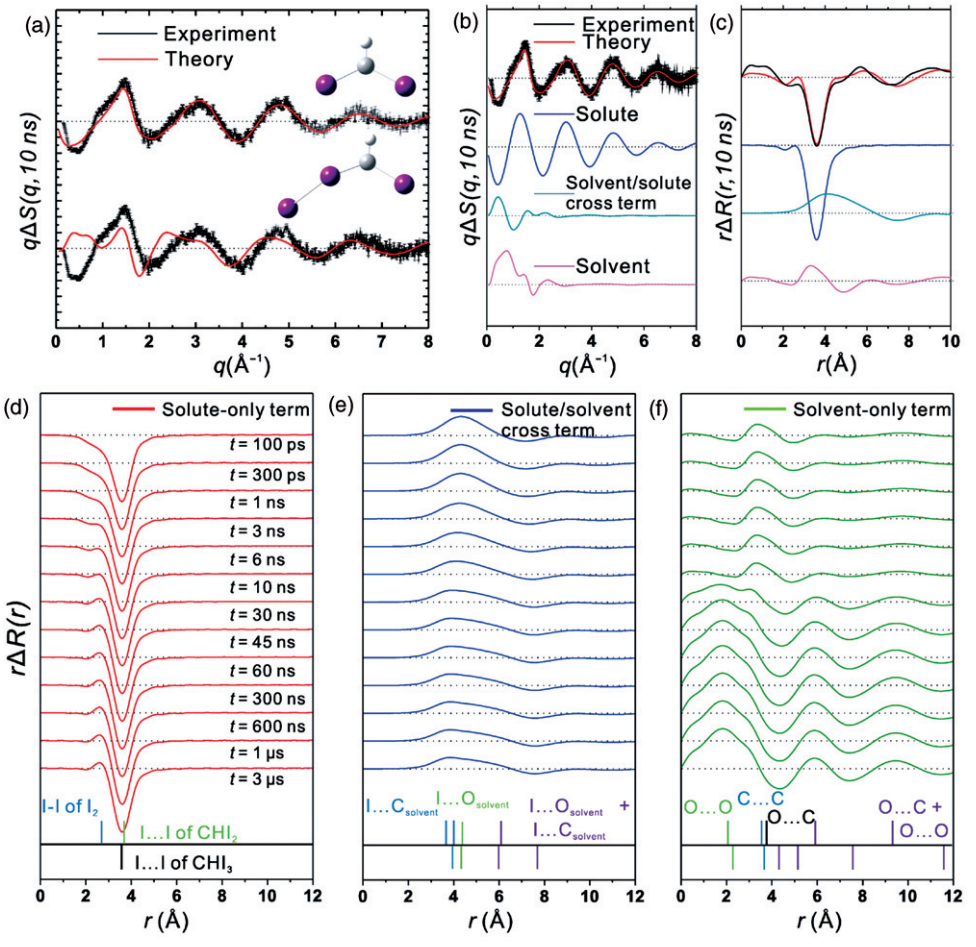


Figure 11. [Colour online] Determining the major reaction channel for $CHI_3$ in methanol excited at 267 nm and decomposition into three components for peak assignment. (a) $q\Delta S(q,t)$ for two-candidate reaction pathways, $CHI_2$ formation vs. $CHI_2$–I isomer formation, are compared. Experimental curves with experimental errors are shown in black and theoretical curves are in red. The $CHI_2$ formation channel gives superior agreement between experiment and theory, confirming that simple dissociation is the major reaction pathway and the isomer formation is negligible. (b) The $q\Delta S(q, 10\,\text{ns})$ curve is decomposed into the solute-only, cage and solvent-only contributions. (c) The same decomposition in the real space for $r\Delta R(r, 10\,\text{ns})$ corresponding to (b). (d) The solute-only component of $r\Delta R(r,t)$. (e) The cage component of $r\Delta R(r,t)$. (f) The solvent-only component of $r\Delta R(r,t)$.

The prominent negative peak around 3.6 Å of the solute-only term (Figure 11d) is due to the depletion of the I $\cdots$ I distance in $CHI_3$ and the shoulder at 2.7 Å in late time delays is due to the formation of a new I–I bond in $I_2$. Most positive and negative peaks located at distances larger than the size of the solute molecule in Figure 11(e) and (f) are related to the solvent rearrangement due to temperature and density changes.

### 4.4. *High-angle analysis: truncated Fourier transform analysis*

As already discussed, the presence of the solvent molecules complicates the data analysis of TRXL data as it requires the consideration of not only the solute-only term, but also the cage term and the solvent-only term. Among these three terms, the solute-only term is easily calculated from the Debye formula that describes the diffraction from isolated molecules (gas phase). The solvent-only term can be determined experimentally in a separate solvent-heating measurement. However the cage term cannot be obtained directly from a separate experiment, and has to be calculated with MD simulations. However, MD simulations are often time-consuming and sometimes the accuracy of MD is questionable due to the use of a finite simulation box and an approximate potential. For example, we showed that the solvent-only terms are much better described by experimental solvent differentials than by theoretical solvent differentials obtained via MD simulations [66]. For this reason, we worked on devising an alternative way of obtaining structural insight based on a $q$-truncated Fourier transform (TFT) [68] to analyse TRXL data using the Debye function for isolated solutes only without involving time-consuming MD simulations and without biasing the experimental data towards candidate models.

The key idea is simple; the Fourier sine-transform (FT) is applied to the experimental data and to theoretical data calculated from the molecular structure of a candidate isolated-solute via the Debye formula, and a comparison of the degree of correlation between the experimental RDF and the model RDFs can then distinguish the best candidate among the isolated-solute models for the reaction intermediates. For the solute containing heavy atoms, which scatter to much larger $q$ values, the high $q$ region is dominated by the solute since the light-atom scattering of the solvent falls off more rapidly with $q$. Since the theory does not include the solvent, the low-$q$ region where the solvent-related terms are relatively high can be excluded in the analysis, and this TFT improves the degree of correlation and facilitates the comparison since it allows for the experimental data to be unbiased by a theoretical model, while still being able to be used to evaluate candidate isolated-solute models. We considered two methods to truncate the low-$q$ region. In the first method, the following integral is evaluated as follows.

$$r\Delta R(r,t)_{\mathrm{TFT}} = \frac{1}{2\pi^2}\int q\Delta S(q+q_T,t)\sin(qr)\mathrm{e}^{-q^2\alpha}\mathrm{d}q, \tag{27}$$

where $q_T$ is the truncation point.

An example of the application of TFT to TRXL data is shown in Figure 12 for the TRXL data at 100 ps for photodissociation of $C_2H_4I_2$ in methanol. TFT is applied to the $q\Delta S(q,t)$ curves of the experimental data and gas-phase models (in this case, the bridged and the anti-structure). The resulting RDFs are displayed as a function of $q_T$. Throughout all $q_T$ ranges above 1 $\mathrm{\AA}^{-1}$, the RDFs from the bridged model show clearly different features from those of the anti-model, especially around 2 Å, which is sensitive to the C–I bond distance. This peak can be used as a fingerprint region because the bridged structure has two identical C$\cdots$I internuclear distances whereas the anti-structure has two different C$\cdots$I internuclear distances. Comparison of the experimental TFT and two theoretical TFTs instantly reveals that the experimental data agrees much better with the bridged model than with the anti-model. When $q_T$ is larger than 1 $\mathrm{\AA}^{-1}$, the experimental RDFs are almost identical to the corresponding RDFs of the bridged model. The RDFs of the anti-model reproduces the experimental peak around 5 Å, but fails around 2 Å. The peak at 5 Å

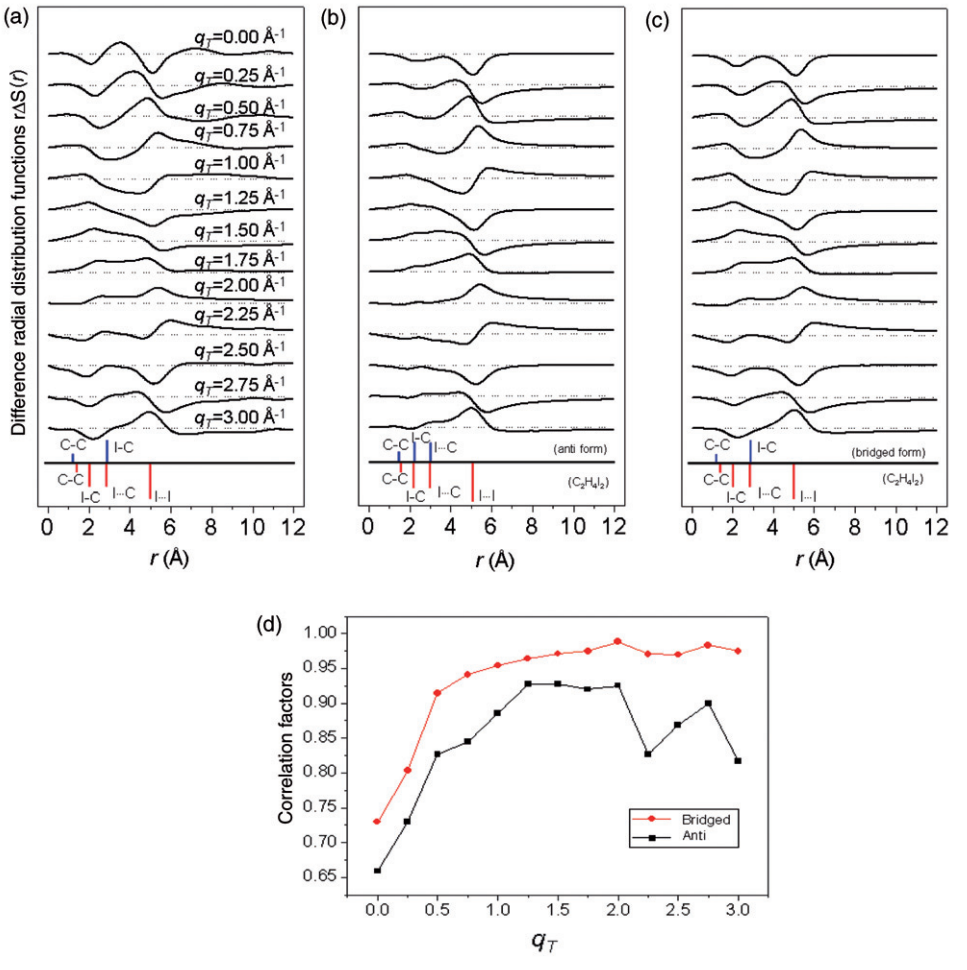


Figure 12. [Colour online] (a) TFT of $C_2H_4I_2$/methanol data at 100 ps, (b) TFT of gas-phase models of the anti-structure and (c) TFT of the bridged structure. At the bottom of each graph, peak assignments are given for the disappearing parent molecule (below the horizontal line) and the appearing intermediate structure (above the horizontal line). The position of a bar is related with the corresponding internuclear distance and the height is proportional to the number of the corresponding internuclear distance. Qualitative comparison clearly indicates that the experimental TFT agrees well with the TFT of the bridged model rather than the anti-model. (d) Structural correlation factors of the experimental TFT data to theoretical models as a function of $q_T$. In general, structural correlation factors to the bridged structure are higher than those to the anti-structure, quantitatively indicating the former explains the experimental data better.

is due to the depletion of the I···I internuclear pair in the parent molecule which is common for both reaction channels. Therefore, the application of TFT with mode B to TRXD data on the photodissociation of $C_2H_4I_2$ in methanol clearly shows that the $C_2H_4I$ transient radical has a bridged structure rather than a classical anti-structure, confirming the previous conclusion [103]. TFT is relevant not only to solution-phase data but also to

gas-phase data [54,56,104,105] because the low-$q$ region (below 2–4 $\text{Å}^{-1}$) of the latter is typically not obtained experimentally.

The comparative analysis of experimental data to theoretical models using TFT described in Figure 12 relies on visual comparison and is therefore rather qualitative. A quantitative tool can be provided using structural correlation factors between the experimental TFT and the TFT of the theoretical model defined as follows:

$$C(t) = \int \left(r\Delta R^{\text{Exp}}(r,t) \cdot r\Delta R^{\text{Model}}(r,t)\right) \mathrm{d}r, \tag{28}$$

where $r\Delta R(r,t)^{\text{Exp}}$ is the experimental RDF and $r\Delta R(r,t)^{\text{Model}}$ the RDF of an isolated-solute model. It is important that both experimental and model RDFs should be normalised so that:

$$\int (r\Delta R(r,t))^2 \, \mathrm{d}r = 1. \tag{29}$$

This normalisation ensures that the correlation factors approach unity for a perfect model. In addition, this makes the experimental data scaled to theoretical models even when the exact population of the transient concentration is not known. Figure 12 shows the correlation factors for $C_2H_4I_2$ in methanol as a function of $q_T$. Comparison of the anti- and the bridged model shows that the correlation factors of the bridged model are always closer to 1 than those of for the anti-model, consistent with the qualitative analysis. The important point is that the experimental data and the theoretical models are transformed in the exact same way. Note that the correlation factor at $q_T = 0$ (i.e. without truncation) already allows one to distinguish reaction pathways. The correlation factors increase with increasing $q_T$ due to the reduced contribution from solvent and comparing correlations factors in a wider range of $q_T$ adds discriminating power.



## 5. Applications

TRXL has been used to capture the molecular structures of intermediates and their reaction kinetics for various photochemical processes. In the following sections, we present some application examples ranging from small molecules to proteins, which illustrate the wide applicability of TRXL.

### 5.1. *Reaction pathways of $HgBr_2$ and $HgI_2$*

Mercuric halides, $HgX_2$ (X = Cl, Br and I), and their photodissociation dynamics have been of much interest due to their optical and electronic properties [106–119]. They are a good model system for studying ultrafast photochemistry thanks to their simple triatomic molecular structure, high photochemical reactivity, fast recombination rates and the presence of heavy atoms [120]. Accordingly, there have been many experimental and theoretical studies on the photodissociation of $HgX_2$ in the gas phase. For example, Zewail and co-workers have studied the photodissociation dynamics of $HgI_2$ using fs transient absorption and fluorescence spectroscopy, discovering two-body dissociation mechanism along reaction coordinates consisting of two vibrational modes [121,122]. Moreover, fs

mass spectrometry [123,124] and theoretical quantum chemistry [125,126] elucidated the branching dynamics of $HgI_2$ on a saddle point on the PES.

In contrast to the intensely studied mercuric halides in the gas phase, photodissociation of $HgX_2$ in solution phase has been studied to much lesser extent. Previously, the photodissociation dynamics of $HgI_2$ (in ethanol and DMSO) and $HgBr_2$ (in $CH_3CN$ and DMSO) in the solution phase have been studied using fs transient absorption spectroscopy, elucidating the vibrational wave-packet motion and solvation dynamics on the timescale of tens of picoseconds [127–136]. However, more comprehensive understanding of the reaction mechanism in the solution phase is needed, in particular, branching ratios and recombination dynamics of photodissociated species spanning from picoseconds to microseconds. To address these unresolved issues, TRXL was applied to study photodissociation dynamics of $HgI_2$ and $HgBr_2$. First, the TRXL study of $HgI_2$ dissolved in methanol successfully revealed the dissociation pathways, solvent energetics and the transient structures of intermediates [137]. In particular, it was found that the primary reaction pathway in solution is two-body dissociation into HgI and I, which is in contrast to the gas-phase reaction involving both two-body ($HgI_2 \rightarrow HgI + I$) and three-body dissociation ($HgI_2 \rightarrow Hg + I + I$) [124]. Later, TRXL was applied to $HgBr_2$ in methanol, elucidating that the major reaction pathway of $HgBr_2$ photodissociation is branched between two-body ($HgBr_2 \rightarrow HgBr + Br$) and three-body dissociation ($HgBr_2 \rightarrow Hg + Br + Br$) pathways. Here, we note that these two branched pathways are not completely parallel to each other. The Hg and Br atoms that are formed via three-body dissociation recombine to form HgBr ($Hg + Br \rightarrow HgBr$), opening a route between the two-body and three-body pathways. This conversion of Hg and Br atoms to HgBr clearly affects the reaction dynamics on the 100 ps timescale and thereafter.

By solving the rate equations of the $HgBr_2$ and $HgI_2$ photodissociation reaction, the time evolution of each chemical species involved in the two reactions were extracted and plotted in Figure 13(a) and (b), respectively. By keeping track of the population changes of the reactant, intermediates and products species, the detailed structural dynamics and reaction rate of each step were elucidated.

The reaction pathways and reaction rates are summarised in Figure 13(c). Initially, 10% of the $HgBr_2$ molecules in the 25 mM methanol solution are excited by the 266 nm laser pulse. Among the photoexcited $HgBr_2^*$ molecules, 74% decay into the ground state by electronic/vibrational relaxation or geminate recombination, releasing their energy to the solvent bath. The remaining 26% portion of $HgBr_2^*$ dissociate completely (8%) or stay as HgBr radical (18%). At 100 ps, the chemical species present are HgBr, Br and Hg. Among them, Br is the dominant species since it is produced in both two-body and three-body dissociation. The transiently generated Br atoms are consumed via three ensuing reactions. First, 24% of the generated Br atoms recombine non-geminately with the entire population of Hg atoms to form HgBr radicals, leading to the increase of the HgBr population in 1–10 ns. Second, 63% of the Br atoms recombine non-geminately with the HgBr radical to form parent $HgBr_2$. The remaining 13% of the Br atoms combine to form $Br_2$ [138,139].

The reaction pathways and the rates for the $HgI_2$ photodissociation are summarised in Figure 13(d) [137]. Initially, 33% of the $HgBr_2$ molecules in methanol are excited by the 266 nm laser pulse. Here, we note that the efficiency of the $HgBr_2$ photoexcitation by UV laser pump is only 10% compared to 33% efficiency in $HgI_2$ due to higher absorption

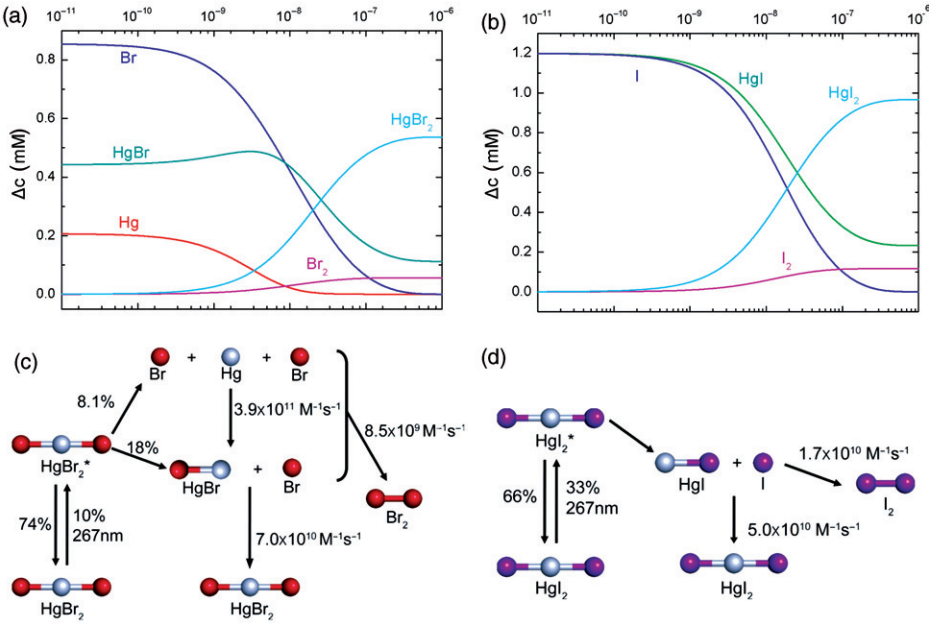


Figure 13. [Colour online] (a) Time-dependent concentration changes of chemical species involved in the photodissociation reaction of $HgBr_2$ in methanol obtained from global fitting analysis. Br (blue), HgBr (green), Hg (red), $HgBr_2$ (cyan) and $Br_2$ (magenta). (b) Schematic of the reaction mechanism of $HgBr_2$ photodissociation in methanol determined by the TRXL measurements and analysis. (c) Time-dependent concentration changes of chemical species involved in the photodissociation reaction of $HgI_2$ in methanol obtained from global fitting analysis. I (blue), HgI (green), $HgI_2$ (cyan) and $I_2$ (magenta). (d) Schematic of the reaction mechanism of $HgI_2$ photodissociation in methanol determined by the TRXL measurements and analysis. It can be clearly seen that reaction mechanisms of $HgBr_2$ and $HgI_2$ are different.
Source: Adapted and modified from Ref. [227].



cross-section of $HgI_2$ than $HgBr_2$ at 266 nm. The difference was compensated for using a higher concentration of $HgBr_2$ (25 mM) than of $HgI_2$ (10 mM). Among the photoexcited $HgI_2^*$ molecules, 66% of returns to the ground state by electronic/vibrational relaxation or geminate recombination. The remaining 34% portion of $HgI_2^*$ dissociate to HgI radical and I atom. Subsequently, $I_2$ is formed by combination of I atoms or $HgI_2$ is formed by non-geminate recombination.

The most notable difference between the photodissociation of $HgBr_2$ and $HgI_2$ is the branching ratio between two-body and three-body dissociation pathways. In other words, the photodissociation of $HgI_2$ occurs only via two-body dissociation pathway, whereas $HgBr_2$ dissociates via both two-body (18%) and three-body (8%) dissociation pathways with about 2 : 1 branching ratio. The difference in the reaction pathways of the two mercuric halides demonstrates the effect of atomic substituents on the reaction mechanism in a simple chemical reaction, although its origin is not clear yet. We can speculate that three-body dissociation of $HgI_2$ occurs at a much higher rate than that of $HgBr_2$, for example at much earlier times than 100 ps. If so, the pathway might not observed with the 100 ps time resolution of this experiment.

The branching ratios and rates of recombination were also found to be different between $HgBr_2$ and $HgI_2$. In particular, via $X + X \rightarrow X_2$ (X = Br, I) reaction, 13% of Br atoms combine to form $Br_2$ at $8.5 \times 10^9\,M^{-1}\,s^{-1}$ in contrast to the formation of $I_2$ with its 29% branching ratio and $1.7 \times 10^{10}\,M^{-1}\,s^{-1}$. The slower formation of $Br_2$ than $I_2$ disagrees with a previous spectroscopic study, where the non-geminate recombination of photodissociated $Br_2$ was found to be almost twice faster than that of $I_2$ in $CCl_4$ solution [139]. This reversal in relative formation rates might be explained by our use of a polar solvent, methanol, rather than the non-polar solvent $CCl_4$ used in the previous study, but the exact origin needs further investigation. In contrast, for $HgX_2$ recovery via $HgX + X \rightarrow HgX_2$ reaction, the reaction rate is higher for $HgBr_2$ than for $HgI_2$. The higher rate of $HgBr_2$ formation is likely to result from the higher diffusion rate of Br.

### 5.2. *Reaction pathways of $Br_2$ and $I_2$*

The dissociation and recombination of diatomic halide molecules, such as $Br_2$ and $I_2$ in solution have been studied for many years by fs and picosecond optical spectroscopy as a paradigm for the dynamics of chemical bonds [140–143]. Using transient pump-probe techniques, the motion of the excited-state wave packet has been probed with down to 30 fs time resolution. The first TRXL study of dissociation dynamics of diatomic halide molecule in solution was performed on $I_2$ in $CH_2Cl_2$ [144], but the weak intensity of the X-ray beam used in the experiment made it difficult to refine the structures of the reaction products due to the poor SNR. Later, TRXL using the pink beam from undulators in a third generation synchrotron, which achieved a 250-fold gain in X-ray intensity, was applied to study the dissociation dynamics of $I_2$ and $Br_2$ in liquid $CCl_4$ to reveal not only the structure of the reaction products but also the hydrodynamics of the solvent medium [63,69,145].

Here, we briefly describe how photodissociation of $I_2$ occurs in $CCl_4$. As shown in Figure 14, the $I_2$ molecule is first excited vertically from its ground state X to a mixture of the B and $^1\pi_u$ states using a 150 fs pulse at 530 nm. The excited states are repulsive and the molecules move apart at an increasing speed. At the curve crossing between B and $^1\pi_u$, all molecules move to the state $^1\pi_u$ due to solvent-induced intersystem crossing. After 300 fs, the atoms collide with the solvent at a distance of about 4 Å with a speed of 1000 m/s. A small fraction, 10%, of the free I atoms escape the cage and recombine in tens of nanoseconds via random diffusion through the solvent, which we term the $\gamma$ process. In the remaining 90% of cases, highly excited $I_2^*$ molecules are formed in the cage in 1–2 ps to recombine directly to the X state ($\alpha$ process) or get trapped in the $A/A'$ state ($\beta$ process). Laser spectroscopic studies have shown that the bottom of the $A/A'$ potential state is reached in less than 10 ps and that the bottom of the X state is reached in about 140 ps. The heat released during the vibrational relaxation is absorbed by the solvent. As described in a previous section, on timescales shorter than 10 ns, the solvent temperature increases at a constant volume. At later times, the solvent expands with a decrease in temperature and density. The recombination time of 140 ps in $CCl_4$ solvent is much longer than in low-Z alcohols, which is ascribed to the relatively high mass of $CCl_4$ and the fact that neighbouring molecules lock into each other thereby reducing the transfer of rotational energy.

To determine the $Br_2$ and $I_2$ solute components alone, the non-excited solvent signal needs to be temperature adjusted to match the solvent temperature when the laser is *on*.

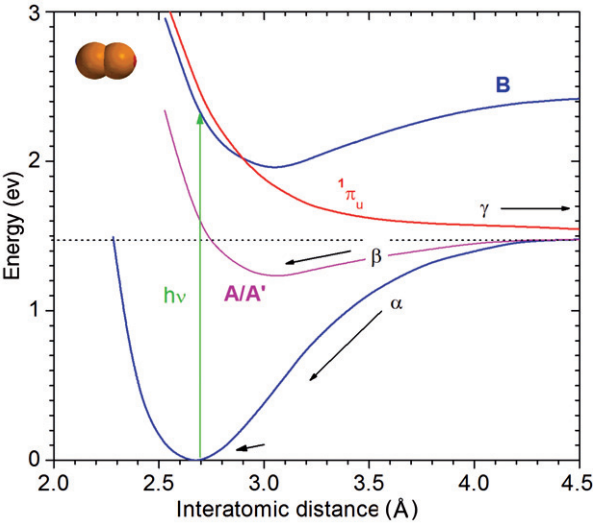


Figure 14. [Colour online] Energy curves for $I_2$ in the gas phase. The laser excitation is shown with the green arrow and the recombination processes $\alpha$, $\beta$ and $\gamma$ are indicated with black arrows.

To do so, the contribution from solvent heating alone is measured by a multi-photon experiment with 150 fs and 400 nm pulses that excite vibrations of the C–Cl bond in $CCl_4$. Then, the measured solvent-heating signal is subtracted from the solution signal, as shown in Figure 15. It should be noted that the solution (black curve) and solvent (red curve) signals coincide at above 4.5 Å, i.e. at the distances larger than the size of a $Br_2$ molecule. A detailed description of the temperature correction and the hydrodynamics can be found in Ref. [69,145].

The photodissociation of $Br_2$ and $I_2$ in $CCl_4$ can be compared as follows. The branching ratios for the $\alpha$, $\beta$ and $\gamma$ processes for bromine in $CCl_4$ were determined to be 30%, 60% and 10% when the dissociation is done at 400 nm. The equivalent figures for iodine are 70%, 20% and 10% [63] at 530 nm. The difference can be understood from the potential energy curves for $Br_2$ and $I_2$ [141]. Predissociation of the iodine B state results in atoms with a kinetic energy of 3600 $cm^{-1}$, while in bromine, the recoil energy is 400 $cm^{-1}$. The energy drop in the repulsive curves of $Br_2$ is thus smaller than in $I_2$. The bromine atoms have shorter internuclear distances, which increases the probability of curve crossing from the repulsive states to the low lying $A/A'$ states. Furthermore, smaller internuclear distances and lower recoil energies lower the possibility of cage escape of bromine atoms. The 5.5 ns lifetime of the $A/A'$ state for bromine is longer than that for iodine with 2.7 ns. The longer lifetime of bromine is attributed to the deeper $A/A'$ well than in iodine [141].

### 5.3. *Effect of the solvents on the reaction dynamics of a solute: $CH_2I_2$ in methanol and cyclohexane*

It is well-known that chemical reactions in solution are very sensitive to the geometry and polarity of the environment which might stimulate certain reaction pathways. This effect has been studied using TRXL in a comparative study of the photoproducts from $CH_2I_2$

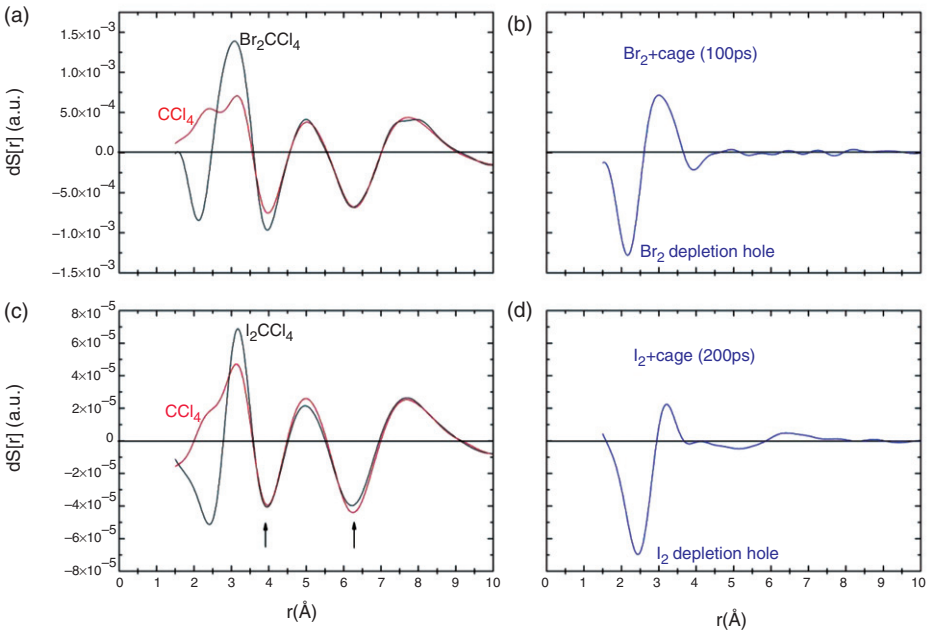


Figure 15. [Colour online] Recovering the solute signal by subtracting the solvent signal from the total solution signal. (a) Change in the electron density for $Br_2/CCl_4$ (black) and for pure $CCl_4$ (red) after 100 ps. The $CCl_4$ curve is from a separate solvent-heating experiment with an ultrashort laser pulse. The curves are scaled to each other at high $r$ values. The two curves approach each other at above 4 Å, which defines the perturbation limit of the excited $Br_2$ structure. (b) The contribution of $Br_2$ solute and cage structure alone is obtained by subtracting the black curve from the red in (a). It is the change in the radial-electron-density seen by an average excited atom in the solution. The $A/A'$ state peaks at 3.0 Å, so these $Br_2$ molecules are 0.8 Å greater than in the ground state at 2.2 Å. Note that the $A/A'$ peak is broader than the $Br_2$ hole, which means that the $A/A'$ potential is broader than in the ground state. The $A/A'$ state decays with a time constant of 5 ns. (c) and (d) The same as (a) and (b), respectively, for $I_2$ in $CCl_4$. Note that the position of the bromine hole is smaller than in iodine and that the $A/A'$ state occupancy is two to three times higher for bromine.
Source: Adapted from Ref. [145].



in a polar and non-polar solvent [76]. Since TRXL provides direct information on the transient structures of reaction intermediates, it is an appropriate tool to study how these structures are perturbed by their interactions with the solvent. The photoreaction of $CH_2I_2$ is initiated by exciting the C–I bond to an anti-bonding state, and subsequently the bond is broken in a fraction of a picosecond. The released iodine radical I·either escapes the solvent cage or recombines geminately with the $CH_2I^{\bullet}$ radical to form a transient $CH_2I{-}I$ isomer or vibrationally excited $CH_2I_2$*.

The fate of the iodine radicals that escape the cage is influenced by the polarity of the solvent. The study by Neutze and co-workers showed that $I_2$ is formed in non-polar solvents, whereas $I_3^-$ is formed in polar solvents. Moreover, the $CH_2I^{\bullet}$ radical lives much longer than $I^{\bullet}$ and $CH_2I{-}I$ and is expected to recombine with another $CH_2I$ to form $C_2H_4I_2$ as a final product. The lifetime of the CHI–I isomer is 4.2 ns in polar methanol and 100 ns in non-polar cyclohexane. Of greater chemical importance is the ability of TRXL to

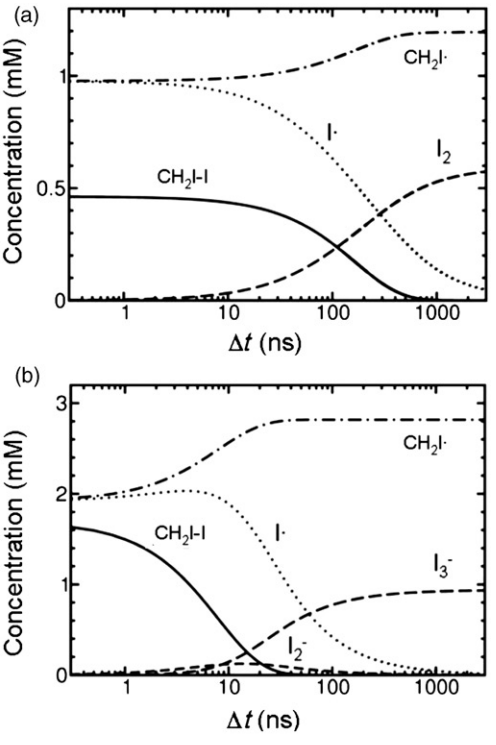


Figure 16. Time dependence of the structural intermediates in the photoreaction of $CH_2I_2$ in a polar and non-polar solvent. (a) Cyclohexane (non-polar). (b) Methanol (polar). The lifetime of $CH_2I$–I is 117 ns in cyclohexane and 4 ns in methanol. The recombination of I takes 150 ns in cyclohexane and 35 ns in methanol. The increase in concentration of $CH_2I^{\bullet}$ is from thermally induced bond breakage in $CH_2I$–I. Note that the $I_2$ formation in cyclohexane is replaced by $I_3-$ in methanol.

determine the I–I distance in $CH_2I{-}I$. This transient iodine–iodine bond is 0.07 Å shorter in cyclohexane than in methanol and the difference is due to the presence of hydrogen bonds in the polar solvent.

The measured scattering curves were analysed against gas-phase candidate structures as computed by DFT. The structures of $CH_2I_2$, $CH_2I^{\bullet}$, $CH_2I{-}I$, $C_2H_4I_2$, I, $I_2$ and $I_3^-$ were calculated and used in MD simulations to determine the solvent packing, i.e. the cage structure, around the molecules. The MD results were used to calculate the change in the scattering curves relative to the initial $CH_2I_2$ structure. By fitting measured scattering curves to theoretical curves consisting of a mixture of structural transitions between transient intermediates, we obtained the time-dependent concentrations of each chemical species involved in the reaction. The comparative results between photodissociation of $CH_2I_2$ in polar (methanol) and non-polar (cyclohexane) solvents are shown in Figure 16.

### 5.4. *Effect of the excitation wavelength on the reaction pathways: $Ru_3(CO)_{12}$ in cyclohexane with visible and UV excitation*

The triangular metal carbonyl cluster $Ru_3(CO)_{12}$ is one of the simplest thermally stable metal carbonyls. This molecular system has served as the paradigm for the photochemistry

of transition metal carbonyls as this complex is used in controlled photoactivated synthesis where specific types of bonds in the complex are broken at specific wavelengths [146,147]. As the mechanism leading to the cleavage of metal–metal bonds is of great theoretical and practical interest [148,149], the photolysis of $Ru_3(CO)_{12}$ has been extensively studied by spectroscopy in solid matrices and in solution [147,150–157]. Ultrafast IR spectroscopy based on the detection of bridging CO ligands of intermediates has been one of the most successful spectroscopic methods in identifying intermediates in the photochemistry of this system whereas most techniques have failed to characterise the structure of the intermediates. Recent ultrafast IR spectroscopy measurements revealed two transient intermediates containing bridging carbonyls, $Ru_3(CO)_{11}(\mu\text{–}CO)$ (Intermediate 1) for the metal–metal cleavage reaction channel and $Ru_3(CO)_{10}(\mu\text{–}CO)$ (Intermediate 2) for the CO loss reaction channel, [157] for solutions of $Ru_3(CO)_{12}$ in non-coordinating solvents, such as cyclohexane excited with either an UV (266 nm) or a visible (400 nm) optical pulse (Figure 17). We also studied $Ru_3(CO)_{12}$ in cyclohexane after photolysis at two different wavelengths (260 and 390 nm) using TRXL. This molecular system represents one of the most complicated ones studied by TRXL as we considered 16 chemical species as potential intermediates. Initial attempts to fit the experimental curves with the known Intermediates 1 and 2 only did not give satisfactory results, suggesting the presence of a third intermediate. The most striking results from the analysis of the TRXL data is that at both visible and UV excitation the major intermediate is not one of the two intermediates identified by ultrafast IR spectroscopy, but rather a new intermediate $Ru_3(CO)_{10}$ (Intermediate 3) shown in Figure 17. This new intermediate has no bridging CO ligand whereas the other two intermediates contain bridging CO ligands. Among the species that we considered, there are three isomers of $Ru_3(CO)_{10}$ but only one of them (Intermediate 3) has no bridging carbonyls. We tried to observe if our data can distinguish among these isomers. The fit with the $Ru_3(CO)_{10}$ with no bridging carbonyls gives the best agreement with the experimental data whereas the fits with the other two isomers are worse. When the three isomers are simultaneously included in the fit, the concentrations of the other two intermediates converge to zero. We concluded that IR spectroscopy can specifically monitors the time course of the concentration of Intermediates 1 and 2 via the absorption bands of their bridging carbonyls, but other intermediates, especially those containing only terminal carbonyls with absorption bands overlapping with those of the parent molecule, may go unnoticed.



With 260 nm excitation (Figure 18) [158], Intermediate 3 ($Ru_3(CO)_{10}$) and Intermediate 1 ($Ru_3(CO)_{11}(\mu\text{-}CO)$) are formed at the onset of the reaction, indicating the rupture of Ru–C and Ru–Ru bonds in $Ru_3(CO)_{12}$ with UV excitation. Since the X-ray pulse width is 100 ps (FWHM), our data are more sensitive to the decay time rather than the rise time of the intermediates. Intermediate 1 decays to the initial $Ru_3(CO)_{12}$ with a unimolecular rate constant of $1.76\ (\pm 1.91) \times 10^7\,s^{-1}$. Intermediate 2, $Ru_3(CO)_{10}(\mu\text{-}CO)$, is not formed from the initial molecule at the onset of the reaction, but appears after 50 ns and recombines with a CO ligand to the parent molecule with a bimolecular rate constant of $3.38\ (\pm 0.36) \times 10^{10}\,M^{-1}\,s^{-1}$. Intermediate 3 dominates at all time delays. It recombines with a CO ligand to Intermediate 2 with a bimolecular rate constant of $2.08\ (\pm 0.24) \times 10^9\,M^{-1}\,s^{-1}$. Since only Intermediates 1 and 3 are formed at the onset of the reaction and Intermediate 1 decays rapidly to the parent molecule, the only pathway to form Intermediate 2 is the recombination of Intermediate 3 with one CO. Intermediate 2

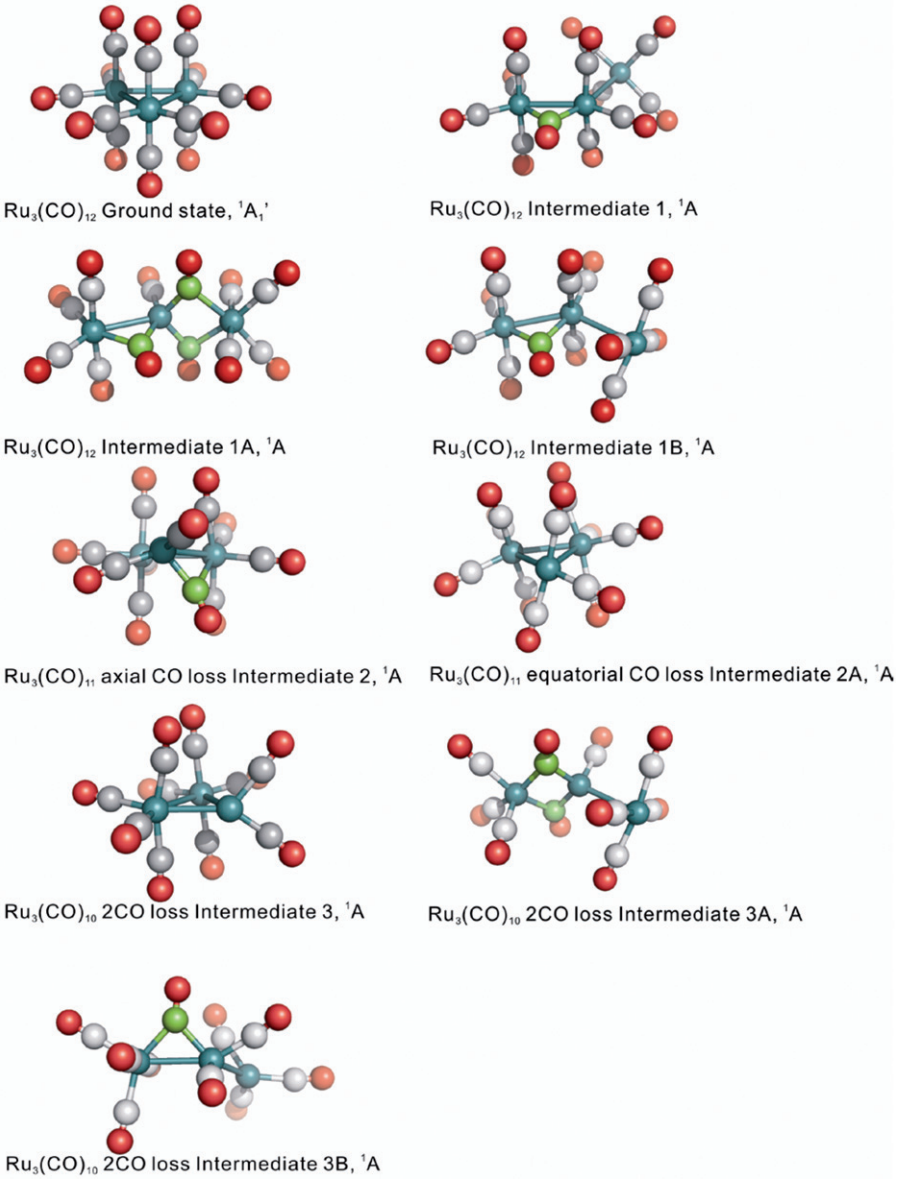


Figure 17. Molecular structures of a parent $Ru_3(CO)_{12}$ molecule (in the ground state) and representative intermediates among 16 species considered after photolysis in cyclohexane. The structures were obtained by DFT calculations. Ru, C and O atoms are coloured in cyan, grey and red, respectively. To distinguish bridging carbonyls, their carbon atoms are coloured in green. Symbols after the name correspond to the symmetry. The B3LYP level with the 6-311 + G(d) basis set for C and O, Stuttgart RSC 1997 ECP for Ru were used in the calculation.
Source: Adapted from the Supporting Information of Ref. [73].

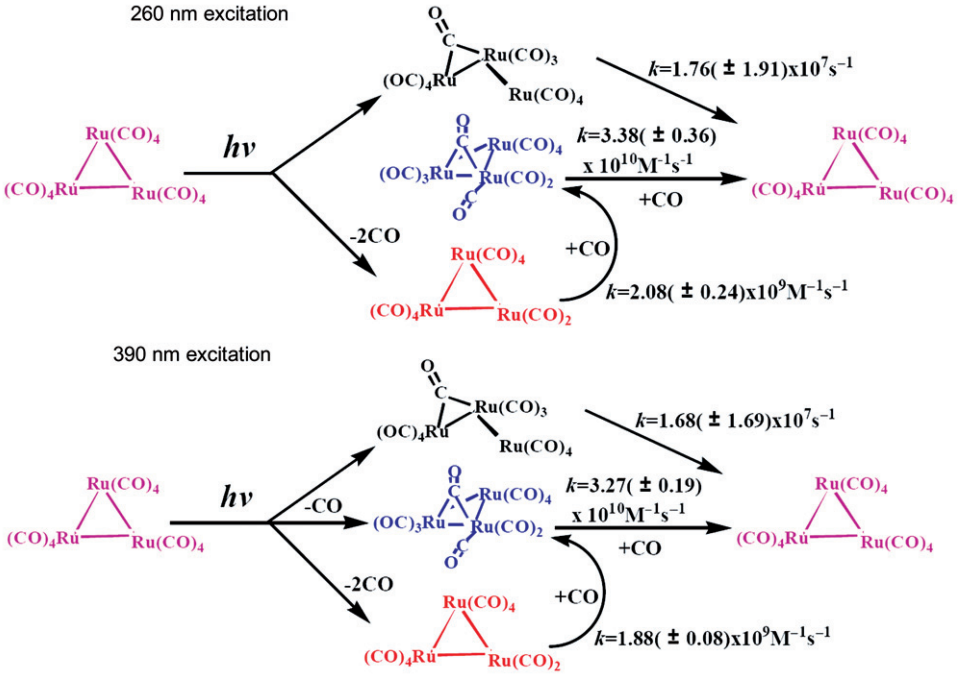


Figure 18. [Colour online] Structural dynamics of $Ru_3(CO)_{12}$ in cyclohexane determined by TRXL at two excitation wavelengths.

does not accumulate as a result of the decay of Intermediate 3 because it is unstable and rapidly recombines to $Ru_3(CO)_{12}$. The results of the fits indicate that the bimolecular rate constant of Intermediate 2 is more than an order of magnitude larger than that of Intermediate 3 which explains their population changes.

On the other hand, at 390 nm excitation, all three intermediates form on the onset of the reaction. Intermediate 1 decays exponentially to the initial $Ru_3(CO)_{12}$ with a unimolecular rate constant of $1.68\ (\pm 1.69) \times 10^7\ s^{-1}$. As it is a very minor species, the error associated with its decay time is rather large. In fact, a reasonably good fit can be obtained without including this intermediate. By contrast, the $Ru_3(CO)_{10}(\mu\text{-CO})$ Intermediate 2 was necessary to obtain a reasonable fit. According to the result of the fit, it recombines non-geminately with a CO ligand to return to the parent molecule $Ru_3(CO)_{12}$ with a bimolecular rate constant of $3.27\ (\pm 0.19) \times 10^{10}\ M^{-1}\ s^{-1}$. Intermediate 3 dominates at all time delays. It decays to Intermediate 2 with a bimolecular rate constant of $1.88\ (\pm 0.08) \times 10^9\ M^{-1}\ s^{-1}$. Since the decay rate of Intermediate 3 is much lower than that of Intermediate 2, the latter does not accumulate from the decay of Intermediate 3. Hence, any intermediate with the formula $Ru_3(CO)_{11}$ can be a candidate for the actual intermediate formed from the non-geminate recombination of Intermediate 3 and a CO ligand. The exact structure of this intermediate connecting the Intermediate 3 and the parent molecule could not be determined in this study. It should be noted that the rate constants observed for the 260 nm excitation are the same as those for 390 nm excitation within experimental errors even if they are not restrained to be the same in the global

fitting analysis. This gives confidence in the data analysis and indicates that the global fitting analysis is a stable method. The dynamics of the $Ru_3(CO)_{10}$ Intermediate 3, which is the major photoproduct and dominates at all time delays, is similar for the two excitation wavelengths. The populations of the minor intermediates (Intermediates 1 and 2) obtained by TRXL are less reliable than those obtained from the specific spectroscopic signal especially for minor species like Intermediate 1. A good fit to the 390 nm excitation data can be obtained with Intermediates 2 and 3 only. Intermediate 1 was introduced in the analysis mainly for consistency with ultrafast spectroscopy. At both 260 and 390 nm excitations, the simultaneous formation of the $Ru_2(CO)_9$, $Ru_2(CO)_8$ or $Ru_2(CO)_6$ dimers by loss of one of the monomer units $Ru(CO)_3$, $Ru(CO)_4$ or $Ru(CO)_5$ from the parent molecule $Ru_3(CO)_{12}$ is not consistent with the TRXL data although it is thermodynamically favoured. In a recent theoretical study [159], the optimised global energy minimum of $Ru_3(CO)_{10}$ corresponds to one of the isomers with bridged CO and $C_{3v}$ symmetry. Inclusion of this $Ru_3(CO)_{10}$ isomer in the data analysis, indicates that its contribution to the scattered signal is insignificant.

Intermediate 2 is formed simultaneously with Intermediates 1 and 3 at the onset of the reaction at 390 nm, through CO loss from the initial $Ru_3(CO)_{12}$. At 260 nm, however, Intermediate 2 is not formed from the initial $Ru_3(CO)_{12}$ at the onset of the reaction but by bimolecular recombination of Intermediate 3 and a free CO around 50 ns. The different kinetics at 260 nm is assumed to be mainly due to the different electronic states involved in the absorption bands of the initial $Ru_3(CO)_{12}$ molecule at UV and visible wavelengths. Theoretical studies of $Ru_3(CO)_{12}$ have shown that excitation at 390 nm populates both the $\sigma \rightarrow \sigma^*$ and MLCT states directly due to overlap of the two bands [146,153,157], resulting in the simultaneous formation of metal–metal cleavage and CO loss intermediates at the onset of the photofragmentation reaction. However, only the MLCT state associated with the CO loss reaction channel is initially populated upon UV excitation, and the $\sigma \rightarrow \sigma^*$ state for metal–metal cleavage reaction channel is assumed to be populated through internal energy conversion which occurs within a few hundred femtoseconds [155,160]. With UV excitation, a competing dissociation reaction favours the simultaneous loss of two CO forming $Ru_3(CO)_{10}$ only at the onset. $Ru_3(CO)_{10}$ then recombines non-geminately with a free CO to Intermediate 2. Careful inspection reveals that with the same initial $Ru_3(CO)_{12}$ concentration, the concentration of Intermediate 3 is 45% higher with excitation at 260 nm than with 390 nm. Previous flash photolysis studies on $Ru_3(CO)_{12}$ in cyclohexane indicated that the quantum yields of CO loss intermediates increase significantly as the excitation wavelength was shortened [161], which is consistent with our observation. In a previous matrix-isolation study at 90 K, it was reported that a transient intermediate $Ru_3(CO)_{11}$ with terminal CO only is formed through the loss of one equatorial CO from the starting molecule $Ru_3(CO)_{12}$ upon UV and visible excitation [146]. It then converts to intermediate 2 with bridged CO by annealing the matrix at 110 K [146]. The result indicated that $Ru_3(CO)_{10}$(μ–CO). Intermediate 2 is formed by the isomerisation of $Ru_3(CO)_{11}$ with terminal CO only. Inclusion of this intermediate in the global fitting indicated that within our time resolution, its formation in solution is negligible both at 260 and 390 nm excitation. As the higher stability of $Ru_3(CO)_{10}$(μ-CO) Intermediate 2 (37 kJ mol$^{-1}$) compared to $Ru_3(CO)_{11}$ with terminal CO only provides a thermodynamic driving force for the isomerisation reaction [157], it is likely that this reaction is too fast to be detected with the current time resolution.

Based on the time dependence of the concentrations of the different intermediates, a photodissociation mechanism of $Ru_3(CO)_{12}$ in cyclohexane can be proposed which is compatible with the time-resolved X-ray scattering and ultrafast spectroscopy results [157]: upon excitation at 260 nm, the metal–metal and metal–carbon bonds rupture in $Ru_3(CO)_{12}$ which lead to the simultaneous formation of Intermediates 3 and 1 at the onset of the reaction. In the course of the reaction, the major product Intermediate 3 recombines with a free CO to Intermediate 2, which eventually decays to the starting molecule $Ru_3(CO)_{12}$ by recombination with another CO. At 390 nm, three intermediates are formed at the onset of the reaction from the initial molecule $Ru_3(CO)_{12}$. The subsequent reactions of Intermediates 3 and 1 are essentially independent of the excitation wavelength with Intermediate 1 rapidly relaxing to the parent molecule $Ru_3(CO)_{12}$ through geminate recombination. A schematic representation of photofragmentation pathways is shown in Figure 18. Formation of other species or reaction pathways that occur much faster than the time resolution of our experiments, of course, cannot be ruled out. This applies in particular to the possibility that $Ru_3(CO)_{10}$ would be formed from the photofragmentation of some early intermediates.



### 5.5. *Tackling irreversible reaction: protein folding of Cyt-c*

Protein structural changes in solution have been mainly characterised by time-resolved optical spectroscopic methods that, despite their high time resolution (<100 fs), are only indirectly related to 3-D structures in space. For protein crystals, a combination of high time resolution and structural sensitivity has become readily available with the advent of sub-nanosecond Laue crystallography [41,44,46,162], but its applicability has been limited to a few model systems due to the stringent prerequisites such as highly ordered and radiation-resistant single crystals. More importantly, crystal packing constraints might hinder biologically relevant motions. Owing to such limitations, time-resolved X-ray crystallography has been applied to only reversible reactions in single crystals, and it cannot be simply used to study irreversible reactions, such as protein folding. To obtain information about protein motions in a more natural environment, X-ray scattering and nuclear magnetic resonance (NMR) have so far been the main direct structural probes of protein structures in solution [163,164]. Due to the inverse relationship between the interatomic distance and the scattering angle, the scattering from macromolecules is radiated at both small angles, the small-angle X-ray scattering (SAXS), as well as in the wide-angle X-ray scattering (WAXS) range. SAXS is sensitive to overall structure, such as the overall size and shape of the protein, while WAXS gives a more detailed information on the tertiary and quaternary protein structures which involve the fold of helices and sheets. However, thus far, the time resolution was limited to 160 μs at best [165]. NMR is also a powerful technique for structure determination in solution, but it works best for smaller proteins and needs properly labelled samples [166]. More importantly, due to the nature of the microwave pulses, the time resolution of protein NMR is inherently limited to milliseconds.

For proteins in solutions, the relatively low concentration (only a few millimolar or less) makes TRXL non-trivial, and the large size of the proteins (more than a thousand times larger volume than for small molecules) complicates the structural analysis. However, the recent TRXL data from model proteins in solution have demonstrated that

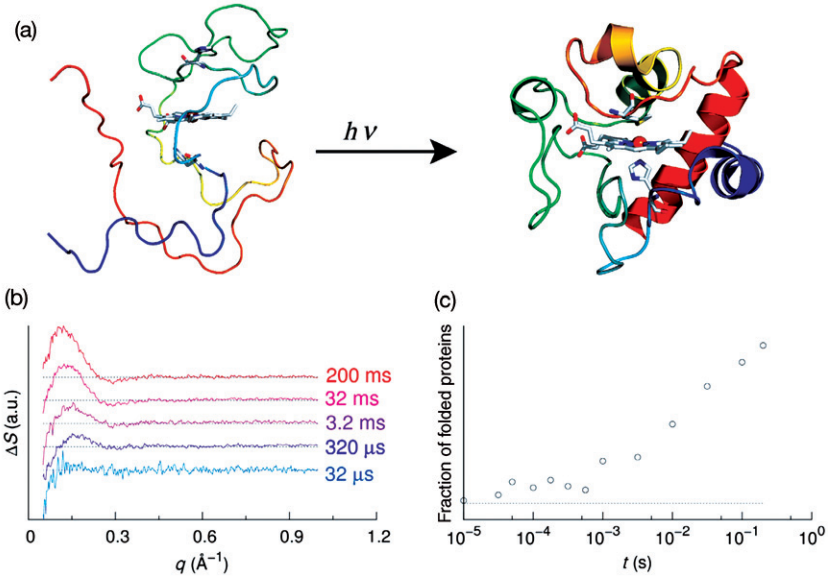


Figure 19. [Colour online] Application of TRXL to track the folding of Cyt-c. (a) Schematic representation of light-induced folding of Cyt-c. (b) Time-resolved WAXS data relative to CO-photolysis-induced folding of Cyt-c. A 200 ns laser pulse at 532 nm was used to initiate photodissociation of the CO ligand, which in turn initiates the folding process. Experimental data at representative time delays are shown. (c) Population of the folded state as a function of time estimated from a linear combination of the experimental signal at 32 μs and 0.2 s (open symbols). A simple exponential analysis yields a time constant of about 25 ms.
Source: Adapted and modified from Ref. [75].



the medium-scale to large-scale dynamics of proteins is rich in information on timescales from nanoseconds to milliseconds [75]. TRXL methodology has been applied to human haemoglobin (Hb), a tetrameric protein made of two identical $\alpha\beta$ dimers that is known to have at least two different quaternary structures (a ligated stable 'relaxed' (R) state and an unligated stable 'tense' (T) structures) in solution. The tertiary and quaternary conformational changes of human Hb triggered by laser-induced ligand dissociation have been identified by TRXL. A preliminary analysis with the allosteric kinetic model gives a timescale for the R–T transition of ~1–3 μs, which is shorter than the timescale derived with time-resolved optical spectroscopy. The optically induced tertiary relaxation of Mb and the refolding of Cyt-c have been also studied by TRXL. As previously mentioned, the advantage of TRXL over time-resolved X-ray protein crystallography is that it can probe irreversible reactions as illustrated with the folding of Cyt-c as well as reversible reactions, such as ligand reactions in heme proteins.

The basic idea of protein folding is that the 3-D structure of proteins is by and large determined by the sequence of their amino acids. Unfolded polypeptide chains use this information to accurately and quickly fold into their native structures (Figure 19a). The optically triggered folding of horse heart Cyt-c has been extensively studied with spectroscopic techniques [167,168] and also by fast-mixing SAXS [165]. Cyt-c is a single

domain protein similar to Mb. Unlike Hb and Mb, Cyt-c does not usually bind external ligands, such as CO since the iron atom of the heme group is covalently coordinated to the Met-80 residue of the protein. However, if Cyt-c is partially unfolded with a denaturing agent, it is possible to replace the Met-80 residue with CO. The substituted CO ligand can be optically dissociated, which in turn triggers the folding process. The time-dependent evolution of the TR-WAXS signal of Cyt-c after photolysis is evident, especially in the small-angle region (Figure 19b). As a preliminary analysis, we fitted the observed signal to a linear combination of one pattern at the earliest time delay, 32 μs, and another at the latest time delay studied, 0.2 s. This simple approach reproduces the experimental data at all times very well. The plot of the weighting factor of the late time component against time is shown in Figure 19(c) and a simple exponential analysis yields a timescale of about 25 ms for the CO-photolysis-triggered folding.

### 5.6. *Extracting the molecular structure of a protein intermediate by experiment-restrained MD simulations: a case study with Mb*



Mb is a heme protein that can bind small-molecule ligands, such as oxygen and CO in muscles. It can be considered as a subunit of Hb, the paradigm protein for the study of allostery. Due to its small size, availability and photosensitivity of the heme-ligand bond, Mb has served as a prototypical model system for studying protein structural dynamics. Accordingly, the structural dynamics of Mb have been intensively studied with various spectroscopic [169–176] and structural [44,177–182] probes. The small-molecule ligands can form covalent bonds with $Fe^{2+}$ in the heme group and they can be photolysed by visible light on the sub-picosecond timescale [170,171]. Upon CO photolysis of MbCO, a small portion of the dissociated CO ligands geminately rebind to the heme, while the others travel to various pocket sites that accommodate them before they eventually escape into the solvent. On longer timescales, MbCO is reformed via non-geminate recombination of CO and Mb. The migration pathways of the dissociated CO have been extensively characterised in solution by time-resolved spectroscopy, but much less is known about the global structural changes, such as helix movements associated with the ligand migrations, partly due to the lack of structural sensitivity of those techniques. Time-resolved resonance Raman spectroscopy is a sensitive probe to structural changes [173] because resonance Raman peaks associated with tyrosine and tryptophan residues provide highly detailed, site-specific information about the structural transitions. However, only selected vibrational modes are enhanced by resonant electronic excitation, making it difficult to obtain global structural information from resonance Raman signals. In contrast to these spectroscopic techniques, TRXSS is sensitive to global structure since X-ray is scattered off all atomic pairs and chemical species in a molecule. Thus, we used TRXSS to directly monitor global structural changes associated with the migration and rebinding of the ligands.

TRXL data on a carbonmonoxy Mb (MbCO) solution upon CO photolysis show a detectable difference scattering curve at the time delay of 10 ns. The existence of the clear oscillatory feature in Mb is significant for the following reason. Hb consists of four subunits and thus large-amplitude quaternary (rearrangements of subunits) structural transitions as well as subtle tertiary (within a subunit) structural transitions are possible between liganded and unliganded states. In contrast, Mb is a single subunit and can accompany only subtle tertiary structural changes. For example, the known crystallographic models of liganded and unliganded Hb show root-mean-square deviation (RMSD)

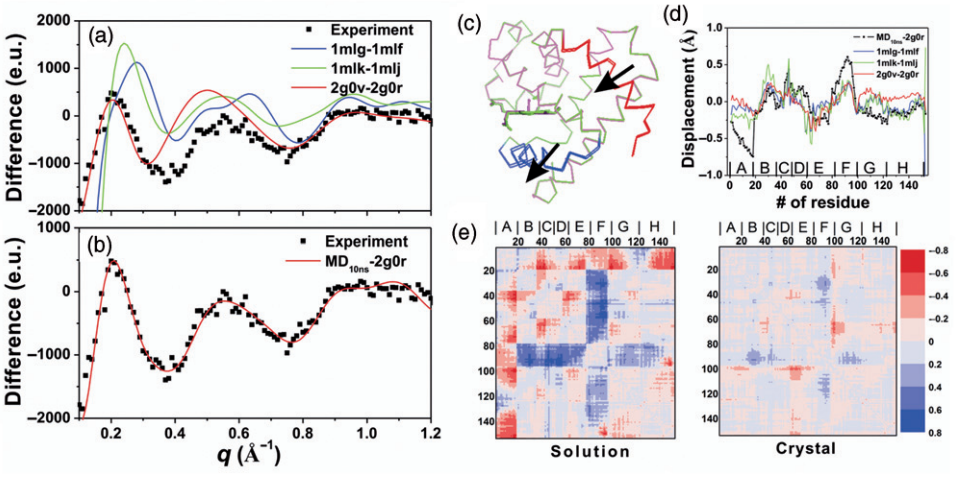


Figure 20. (a) TRXSS data at 10 ns for MbCO → Mb in solution, and comparison with calculated difference curves (Mb–MbCO) where various known crystallographic models are used. (b) Experimental data and comparison with the difference scattering curve from a solution structural model for Mb (MD 10 ns) found from an experiment-restrained MD simulation and a reference crystallographic model for MbCO (2g0r). (c) Overlap of the obtained solution structure of Mb (green) and MbCO (magenta). The largest movements (indicated with arrows) are seen in the F helix (blue) and the A helix (red). (d) Displacement plot between the refined Mb structure (MD 10 ns) and MbCO (2g0r) as a function of amino acid sequence and comparison with those of crystal structures. Helices are labelled in the bottom. (e) Comparison of difference distance maps for solution and crystal (Left) A difference distance map between the refined solution Mb model obtained from experiment-restrained MD modelling and a reference crystallographic model for MbCO (2g0r). (Right) That of crystal structures (2g0v–2g0r). Helices are labelled in the top.
Source: Adapted from Ref. [220].

values from 4 to 9 Å through the quaternary structural change [183], but the corresponding RMSD values between the known crystallographic models of Mb and MbCO are less than 0.3 Å [181,182]. The fact that the Mb data show clear oscillatory features supports the high structural sensitivity of TRXSS, but extracting structural information from the measured data is another challenge. To tackle this problem, we developed a tool for structure analysis, experiment-restrained rigid-body MD simulations.

The first quick-and-easy process one can try is to calculate the scattering curves from the crystallographic models of Mb and MbCO in the protein data bank (PDB). In Figure 20(a), the experimental difference curve of MbCO–Mb is compared with a 'crystal-difference-curve' which is obtained from various known crystallographic models. Among the numerous available crystallographic models, the three curves closest to the experimental curve are shown. Crystallographic models do not agree well with the experimental data, indicating that the solution structures are different. Note that the crystallographic models also show some structural variations among themselves as evidenced by the different scattering curves.

Normally static X-ray scattering data is used for *ab initio* 3-D shape determination from the envelope model, the bead model, and the dummy-residue (DR) model [184–188]. Recently, rigid-body modelling, where the tertiary structures are preserved, has been applied to construct multidomain proteins from solution scattering [189]. This rigid body modelling

technique based on atomic structures uses known crystallographic models to calculate the scattering amplitude of the rigid-body which is determined by the atomic structures. In addition, Monte Carlo (MC) simulations using simulated annealing or restrained MD simulations are combined with modelling techniques to avoid being trapped in a local minimum in a refinement target function [163,184,190]. These modelling methods provide a large convergence to find structures from the scattering data, but require *a priori* assumptions, for example known crystallographic models. In our structural modelling, we have used a similar experiment-restrained rigid-body MD approach that uses *a priori* knowledge based on the available crystallographic models. In our approach, the protein is divided [163,189–192] into a number of (here we used eight) rigid bodies in the unit of $\alpha$ helices. The heme is used as a separate rigid body. The difference between the calculated and experimental scattering curves is used to calculate an MD force term in addition to the usual van der Waals force term. A time-resolved difference scattering curve rather than a static scattering curve is used as the experimental curve. An MD simulation with simulated annealing runs until it reaches a best structure whose theoretical difference scattering curve gives satisfactory agreement with the experimental data. To check the validity of our rigid-body MD approach, we generated a mock difference curve using two known structures of Mb and MbCO, also generated structural variants by modifying the original Mb structure and used these modified structures (G1, G2 and G3) as the starting structures. The subtle structural difference between the two structures can be visualised in the difference distance map (Figure 21b) that plots the difference of the distance between any possible combinations of two C$\alpha$ atoms in the two structures. One can observe that the overall patterns of the difference distance maps for G1, G2 and G3 relative to the same reference structure (2g0r) are quite different. Accordingly, as shown in Figure 21(a), the three difference curves calculated from G1, G2 and G3 do not agree with the mock data and also show considerable discrepancies among themselves. After rigid-body restrained MD simulations the final structures ($MD_{G1}$, $MD_{G2}$ and $MD_{G3}$ where the subscript denotes the starting structure) converged to the correct structure with RMSD values less than 0.1 Å. This can be also seen in their difference distance maps that show more or less identical patterns. The difference scattering curves are also in excellent agreement with the mock data, confirming that our procedure can find the global minimum faithfully.

After verifying that the restrained rigid-body MD simulation works for mock data, we applied it to the experimental data using various crystallographic models as starting structures. The best agreement was obtained for MbCO fixed at 2g0r and Mb varied starting from 2g0v. The agreement is satisfactory up to 1 $Å^{-1}$. The obtained solution-structure provides us with the opportunity to compare it with the crystallographic model. The overall pattern of the solution model is similar to that of the crystallographic models. The most well-known structural change for MbCO $\rightarrow$ Mb is the clamshell movement where the E and F helices move downwards relative to the position of the heme. The solution model also follows the same motion. However, there are also apparent differences in that the solution model shows a larger displacement in the A and F helices.

### 5.7. *Structural dynamics of light-driven bR*

bR and proteorhodopsin (pR) are light-driven proton pumps that were both studied recently by Neutze and co-workers using TRXL [193]. Following the absorption of a

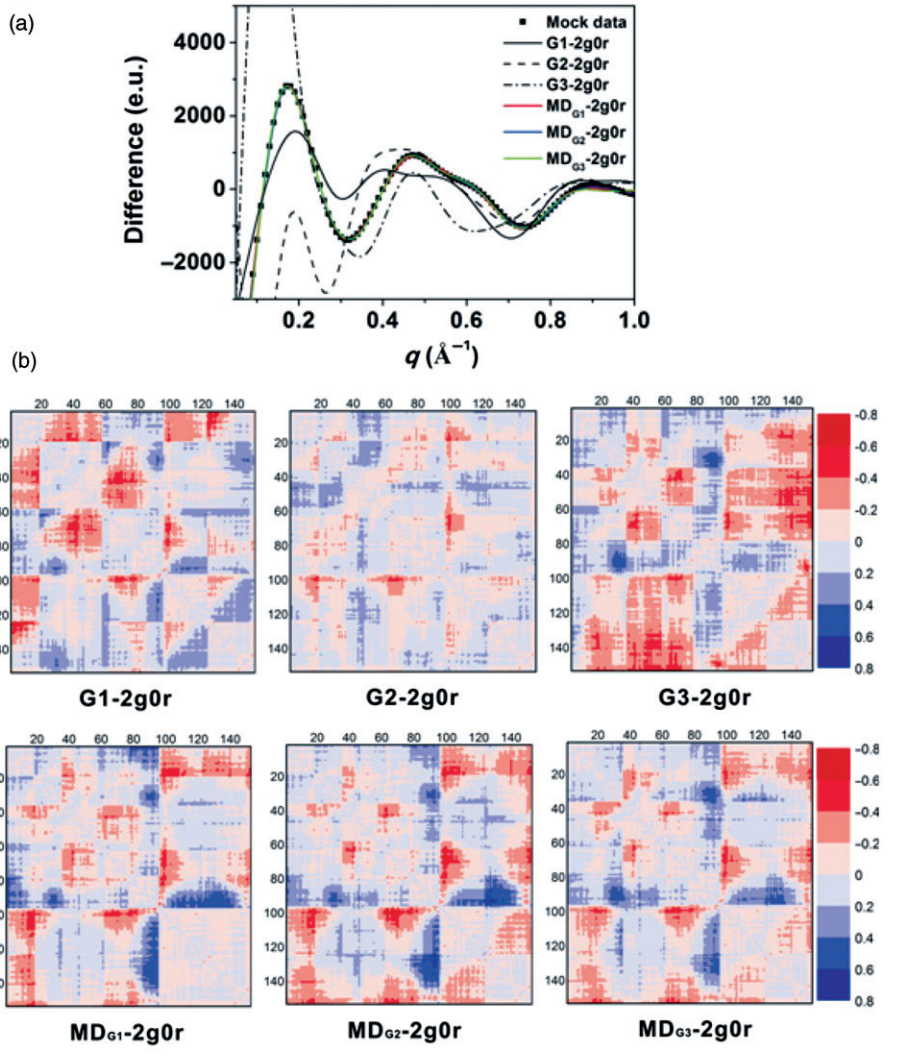


Figure 21. (a) Difference scattering curves before and after rigid-body-restrained MD simulations. The mock data was generated by subtracting the scattering curve of a crystallographic model for MbCO (2g0r) from the scattering curve of a Mb structure modified from 2g0v. We also generated structural variants (G1, G2 and G3) by modifying 2g0v as starting structures. After experiment-restrained MD simulations the final structures ($MD_{G1}$, $MD_{G2}$ and $MD_{G3}$) converged to the correct structure with RMSD values less than 0.1 Å. (b) (Top) Comparison of the difference distance maps of G1, G2 and G3 structures. The 2g0r structure is the reference. (Bottom) Comparison of the difference distance maps of $MD_{G1}$, $MD_{G2}$ and $MD_{G3}$ structures. The difference distance maps for G1, G2 and G3 show clearly different patterns whereas those for the final structures ($MD_{G1}$, $MD_{G2}$ and $MD_{G3}$) are almost identical, indicating that after experiment-restrained MD simulations, the final structures ($MD_{G1}$, $MD_{G2}$ and $MD_{G3}$) converge to the correct structure.
Source: Adapted from the Supporting Information of Ref. [220].

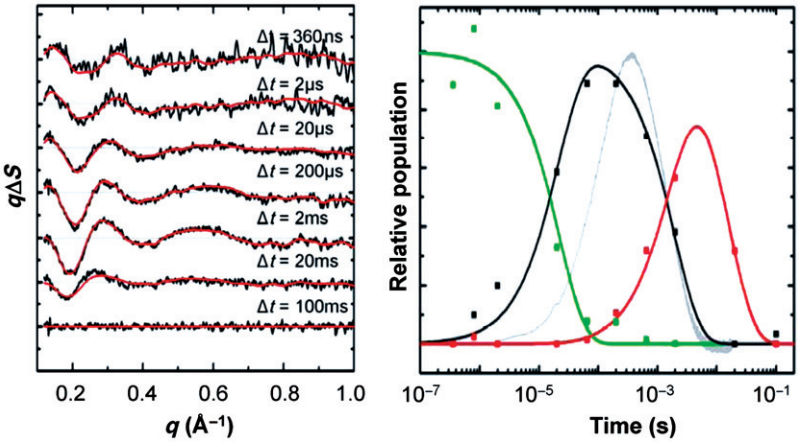


Figure 22. [Colour online] Time-resolved WAXS data probing the photocycle of bR following photoactivation (left) and its decomposition (right) into three generic components (early, green; intermediate, black; and late, red). Note that the 100 ms curve is zero as the photocycle is completed in less than 100 ms. Solid red lines in the left panel show how this spectral decomposition accurately represents the experimental data (black lines). The transient change in absorption at 410 nm, which characterises the Schiff base deprotonation, is shown in grey.



photon by a retinal molecule inside bR, a sequence of conformational changes occur to drive proton pumping across the cell membrane. bR has been intensely studied for four decades whereas pR, a homologue found in bacteria in the oceans, was discovered only a decade ago. It is now recognised that pR provides a major primary energy input into the ocean's biosphere [194].

Several X-ray diffraction studies of the resting state and trapped intermediate states of bR have been reported [195]. Although many details concerning the movements of amino acid residues and water molecules were revealed in these low-temperature studies, the results were sometimes controversial since the nature and magnitude of the observed $\alpha$-helix movements did not always agree between the studies. To address the controversy, the TRXL method was used to study the structural dynamics of bR protein at room temperature.

The difference WAXS curves for bR, shown in Figure 22, were decomposed into three time-independent, spectrally distinct curves by SVD analysis. These three basis spectra represent early, intermediate and late stages of protein conformation change before returning to the resting state. By fitting time-dependent scattering curves of bR using these basis spectra, the timescales upon which these curves rise and fall were extracted from the scattering data (Figure 22). The basis spectra were compared with the intermediate bR structures in crystals from PDB. The solution scattering curves equivalent of the crystal structures were calculated with the software CRYSOL [196]. These predicted scattering curves were calculated for the same number of residues for the resting and excited state to prevent artificial differences due to differing numbers of residues. It turned out that none of the crystal models match the experimental data everywhere in $q$ satisfactorily. Three structures captured some aspects of the WAXS data between 0.2 and 0.7 $\text{Å}^{-1}$, the L-state structures [197,198] and the D96G, F171C, F219L triple mutant [199].

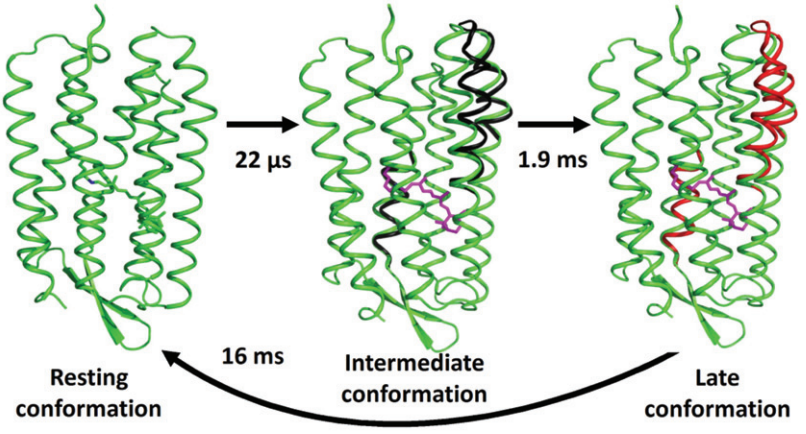


Figure 23. Large-scale $\alpha$-helical movements during the photocycle of bR as observed by time-resolved WAXS. The resting conformation (green), an intermediate conformational state (black) and a late conformational state (red) are represented. Significant outwards movement of the cytoplasmic portions of helices E and F, and an inwards movement of helix C towards the Schiff base, occur already within 22 µs of photoactivation and increase in amplitude later in the photocycle.



This situation is very different from what emerged from time-resolved WAXS studies of photolysed Hb : CO complexes [75] for which the deposited X-ray structure directly yielded a fair fit to the data.

Therefore, it was necessary to refine these initial crystal structures against the difference WAXS data. The analysis revealed that significant movements of the cytoplasmic halves of the $\alpha$-helices E and F, and of the extracellular half of helix C, occur prior to the primary proton transfer event from the retinal Schiff base to Asp85. The amplitudes of these movements were observed to increase further by 50% during the latter half of the photocycle after the Schiff base was deprotonated (Figure 23). This overall picture provides a significantly simpler description of the structural changes that occur during proton pumping by bR that emerged from intermediate trapping studies. Moreover, very similar structural conclusions were drawn from time-resolved WAXS data recorded from pR, revealing shared dynamical principles for proton pumping. Finally, by successfully resolving the nature and time scales of $\alpha$-helical movements that occur in a well-characterised membrane protein-like bR, this study opens the door to future studies of the structural dynamics of more complex integral membrane proteins.

## 6. Potential applications with XFELs

Compared to time-resolved optical spectroscopy, TRXD techniques using the third generation synchrotrons has limited time resolution, at best ~100 ps. Now, this limitation can be overcome with the advent of accelerator-driven fs X-ray sources. One of them is the XFEL that uses self-amplified spontaneous emission (SASE) from an electron bunch in long undulators at the end of a linear accelerator. The XFEL that will be operational from year 2010, the LCLS at Stanford, will generate highly coherent, sub-100 fs X-ray

pulses with typically $10^{12}$ photons per pulse at 8.5 keV. This technical breakthrough in pulsed X-ray source is expected to revolutionise ultrafast X-ray science, opening many new opportunities for doing novel experiments and theories. In particular, the XFEL will substantially improve the pulse duration, photon flux and coherence of the X-ray pulses, making TRXD even more powerful for studying reaction dynamics. In this section, we propose potential XFEL experiments for studying reaction dynamics by taking full advantage of the highly coherent nature of the ultrashort XFEL pulses. Examples of fs X-ray diffraction experiments using highly coherent, sub-100 fs pulses from an XFEL include chemical reactions of small molecules in the gas and solution phases, solvation dynamics and protein structural transitions. In these potential experiments, ultrafast reaction dynamics and motions of coherent rovibrational wave packet can be monitored in real time. In addition, the high photon flux and coherence of the XFEL pulses might make it possible to obtain the 3-D structure of a protein from diffraction patterns of single protein molecules.



### 6.1. *Gas-phase reactions*

The gas phase is ideal for studying reaction dynamics due to its isolated, collision-free environment. Accordingly, there have been many studies of reaction dynamics in the gas phase by optical spectroscopy [14] and time-resolved electron diffraction [200–203]. In particular, time-resolved electron diffraction has been effective in directly probing structural dynamics of small molecules in the gas phase. However, the technique has been limited in resolving ultrafast dynamics owing to the relatively poor time resolution of about 1 ps. The TRXD technique can overcome this limitation using fs X-ray pulses from an XFEL.

Here, we note that gas-phase reaction dynamics have never been studied by X-ray diffraction. The lack of gas-phase studies with X-ray diffraction is attributed to (1) the low density of the sample provided by a molecular beam and (2) the low flux of X-ray pulses from synchrotrons. The first issue can be addressed by the advance of gas-phase ultrafast electron diffraction technique, which has already demonstrated that a gas pressure sufficient for diffraction measurements can be achieved using a medium-pressure nozzle, and the second issue will be solved by the high photon flux from an XFEL. The number of electrons per pulse in a typical time-resolved electron diffraction is $\sim 10^4$ at 1 kHz [201]. In order to make up for the deficiency in scattering power ($1:1 \times 10^6$) and the repetition rate ($\sim$100 Hz for XFEL) of X-ray versus electron, one will need $10^{11}$ ($=10^4 \times 10^6 \times 10$) X-ray photons per pulse. Since XFEL can generate X-ray pulses containing more than $10^{12}$ photons per pulse, TRXD will be able to readily probe gas-phase structural dynamics under similar conditions as for TRED (with a sample pressure of 1–10 Torr in the diffraction volume). Besides, the TRXD using XFEL will have a time resolution of $\sim$100 fs, which is not only 10 times better than state-of-the-art electron diffraction but also comparable to the period of molecular vibrations. With such time resolution, the atomic motions in a molecule can be recorded literally in 'real time'. Thus, X-ray diffraction using XFEL radiation will open up a new horizon in gas-phase reaction dynamics.

For the first gas-phase TRXD experiment, molecules of interest include diatomic molecules, such as $I_2$ and NaI. Previously, photodissociation dynamics of these small molecules have been intensely studied in the gas phase by fs optical spectroscopy and

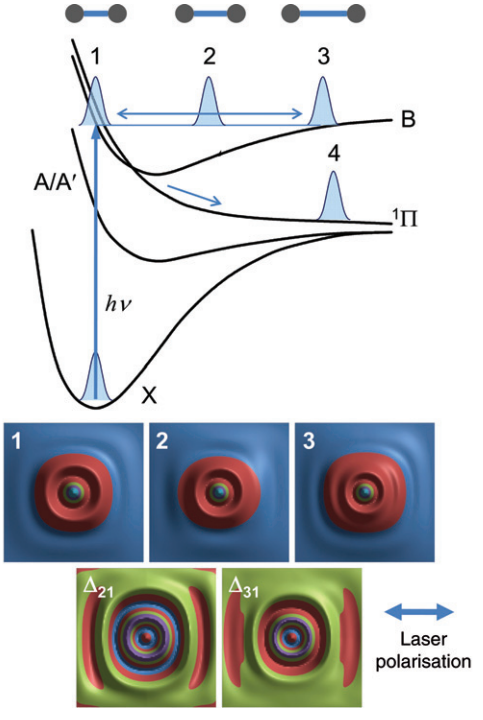


Figure 24. Photodissociation dynamics of iodine ($I_2$) in the gas phase. Once the iodine molecule is photoexcited to a bound B state by a linearly polarised coherent laser pulse, the coherently prepared rovibrational wave packet evolves in the B state, inducing the oscillation of I–I bond length (**1**–**3**) and molecular orientation. The oscillation in the bond length is manifested in the X-ray diffraction patterns, as shown in the bottom. The difference diffraction patterns ($\Delta_{21}$ and $\Delta_{31}$) between the images obtained at different nuclear configurations reflect the changes in molecular structure associated with wave packet motions. In addition, the anisotropy in the diffraction pattern is distinct due to the alignment of molecular orientation along the laser polarisation direction. The ability to transiently align the molecule using polarised excitation will freeze the orientation of the molecule, allowing us to determine the molecular structure more accurately in an aligned molecule. As time evolves after photoexcitation, the excited population will be transferred to a repulsive $^1\Pi$ state at the surface crossing between B and $^1\Pi$ states, leading to photodissociation to two iodine atoms (**4**). Source: Adapted from Ref. [231].

ultrafast electron diffraction. Furthermore, the electron diffraction signals in the femtosecond regime have been already simulated for some of these systems [204,205]. Owing to the vast amount of both experimental and theoretical results available for comparison and accessibility by quantum chemistry due to their simple molecular structure, these molecules are ideal systems to test the performance of fs X-ray diffraction experiment using XFEL.

To get a glimpse of what type of detailed information can be obtained from this novel experiment, we will take a closer look at one of the proposed systems, iodine ($I_2$) in the gas phase. When a ground-state iodine molecule is excited to a strongly bound B state which then relaxes to the repulsive $^1\Pi$ state, the distance between the two iodine atoms increases and the iodine molecule eventually dissociates into two iodine atoms, as shown in Figure 24. By making use of sub-100 fs time resolution and highly coherent nature

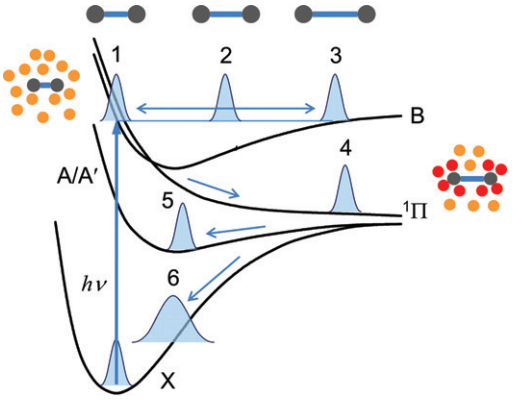


Figure 25. [Colour online] Photodissociation dynamics of $I_2$ molecule in the solution phase. Once an iodine molecule is excited to a bound B state, coherently prepared rovibrational wave packet evolves to induce the oscillation in I–I bond length (**1**–**3**) and molecular orientation. Owing to the solute–solvent interaction, the vibrational and rotational coherences dephase much faster than in the gas phase. Once it relaxes to a repulsive $^1\Pi$ state, internuclear distance between two iodine atoms start to increase (**4**). However, due to the cage effect by the surrounding solvent molecules, most of the excited iodine molecules geminately recombine to form a wave packet either in the $A/A'$ state (**5**) or in the hot ground state (**6**). These wave packet motions and transitions between energy surfaces of different states can be readily probed by fs X-ray diffraction measurement.
Source: Adapted from Ref. [231].



of the X-ray pulses generated from XFEL, many important aspects of this photoinduced reaction, other than a simple reaction rate, can be elucidated.

First of all, the initial dynamics of the vibrational and rotational wave-packet motion in the excited state can be directly probed by XFEL pulses. Such fast wave-packet dynamics could not be resolved by picosecond X-ray or electron diffraction due to lack of time resolution. When an iodine molecule is photoexcited by an ultrashort laser pulse, a rovibrational wave packet is coherently prepared on the B state. As the wave packet evolves in the bound B state, the motions of the wave packet will result in oscillations of I–I bond length and orientation of the iodine molecule. Such oscillation in molecular structure and orientation will appear as a periodic change in the diffraction pattern in time, giving a direct evidence of quantum mechanical wave-packet dynamics and related structural changes. Here, we note that the 'wave packet' term is used in a loose manner to describe both coherent states and incoherent ensembles of iodine.

The vibrational wave-packet dynamics reflected in the X-ray diffraction pattern are well-demonstrated in the simulated X-ray diffraction patterns shown in Figure 24. The 2-D diffraction pattern was calculated using a typical approach based on Debye formalism. Here, we note that, to simplify the calculation, we used the Debye formalism that takes into account only interatomic distance of the constituent atoms based on the Born–Oppenheimer approximation. In principle, however, the diffraction pattern is sensitive to the electron density distribution within a molecule rather than nuclear positions. Therefore, one may explore changes in electron density distribution by including quantum mechanical description of molecular wave functions [206]. To account for the

effect of a linearly polarised laser excitation, instead of orientationally averaging equally over $\theta$ and $\varphi$, we applied the excitation probability proportional to $\cos^2\theta$, where $\theta$ is the angle between the laser polarisation and the direction of I–I bond. A number of randomly oriented $I_2$ molecules were generated and treated to be excited following the $\cos^2\theta$ excitation probability. Diffraction patterns from $I_2$ molecules of various orientations were averaged to obtain an orientationally averaged 2-D diffraction pattern, as shown in Figure 24. Following this approach, we calculated the X-ray diffraction patterns at different nuclear configurations of photoexcited iodine molecule in the bound B state. As the bond length between iodine atoms varies in the B state, it can be clearly seen that the shape and pattern of the 2-D diffraction image change. The same wave packet motions are manifested in the fs optical spectroscopic signals as vibrational and rotational quantum beats owing to quantum interference effects [207–209]. Direct observation of these nuclear wave-packet motions will help to reveal the geometry and anharmonicity of molecular PES, transition dynamics at the surface crossings between different energy surfaces and detailed reaction pathway associated with molecular structure. For iodine in the gas phase, at 5 K, the period of vibrational coherence is ~300 fs with the coherence maintained longer than 40 ps, while the recurrence period of rotational coherence is ~600 ps with a dephasing time of ~50 ps [207,208]. Considering the long lifetime of the B state (microsecond timescale) as well as the long dephasing time of the vibrational and rotational coherences compared to the fs time resolution of the XFEL–TRXD experiment, many periods of wave-packet motions should be readily resolved in the gas phase.

By making use of polarised laser excitation, more information on the structural transitions of chemical reactions can be obtained. For example, excitation by linearly polarised laser light will have the effect of transiently aligning the transition dipole moment of the excited molecule along the direction of polarisation, as demonstrated by the anisotropic diffraction pattern measured in the photodissociation of $C_2F_4I_2$ with electron diffraction [203]. The ability to freeze the molecular alignment transiently will help to determine the structure of reacting molecules more accurately. For example, the dephasing of rotational coherence commonly takes tens of picoseconds, and therefore, the dynamics of vibrational wave packet occurring on hundreds of femtoseconds can be obtained from the transiently aligned molecules. This prediction is well-supported by the simulated X-ray diffraction patterns shown in Figure 24. The X-ray patterns were calculated assuming that iodine molecule is photoexcited by linearly polarised light. In the difference signals between the diffraction patterns obtained at different nuclear configurations in the B state, the anisotropy along the polarisation direction is distinct. Such anisotropy associated with the transient molecular alignment will persist much longer than the period of vibrational wave-packet motions. Also, by monitoring the disappearance rate of such anisotropic pattern, the dephasing dynamics of rotational wave packet can be obtained as well. Therefore, the excitation using linearly polarised light will help us to characterise the transient structures and their dynamics more accurately.

More challenging targets for femtosecond TRXD experiment are polyatomic molecules with more than two atoms. They include haloalkane molecules, such as $CF_3I$, $CF_2I_2$ and $C_2F_4I_2$, organometallic compounds, such as $Fe(CO)_5$ and $(C_5H_5)Co(CO)_2$ and hydrocarbons, such as pyridine ($C_5H_5N$) and cyclohexadiene ($C_6H_8$). These molecules have been studied by electron diffraction since the gas pressure sufficient for the diffraction experiment is easily achieved for these molecules. However, due to relatively poor time

resolution of electron diffraction, only a few picoseconds, only the molecular structures of the transient intermediates were obtained while the details of real-time atomic motions were not captured. For example, picosecond electron diffraction studies on ring-shaped molecules, such as pyridine [210] and cyclohexadiene [55] demonstrated the kinetics of the ring opening upon photoexcitation, but could not determine the structural mechanism, for example whether the ring is broken in a symmetric or asymmetric fashion. Using the fs TRXD technique, such initial atomic motions along the reaction coordinates can be captured in real time. Clusters of atoms or molecules are even more challenging. These systems have been studied by time-resolved electron diffraction as well [211], but only with microsecond time resolution limited by the time of flight after a nozzle. The fs TRXD should be able to follow the phase transition within a cluster, elucidating the relationship between the structural parameters and the phase transition.

To summarise, fs TRXD measurement of reaction dynamics in the gas phase is feasible when considering the photon statistics. Since the diffraction signals from gas-phase reactions are supposed to be much simpler than those in solution without the complication of solvent interactions, studying gas-phase reactions in parallel with liquid-phase reactions will be beneficial for testing the performance of XFEL radiation. The proposed fs TRXD experiments in the gas phase will monitor the reaction dynamics in the collision-free limit and demonstrate the full power of TRXD technique combined with XFEL.

For the gas-phase TRXD experiment, the gas vapour sample can be supplied through a medium-pressure nozzle connected to a heated sample reservoir [201]. Typically, the pressure at the nozzle is about 5 Torr when the backing pressure is about 100 Torr. At this condition, the ambient pressure inside the vacuum chamber can be as high as $10^{-3}$ Torr. To maintain a good vacuum in adjacent chambers, differential pumping should be employed. Clusters of atoms or molecules can be obtained as well using a sufficiently high backing pressure.



### 6.2. *Reactions in liquid and solution phases*

In the recent years, structural dynamics of chemical reactions in solution have been successfully studied by TRXL using the third generation synchrotrons with a time resolution of ~100 ps. As described earlier, the use of XFEL radiation will significantly improve the time resolution of TRXL, reaching the realm of optical spectroscopy in its ability to resolve ultrafast processes. Among the candidates for the first fs TRXL experiment in solution phase are diatomic molecules ($I_2$ and $Br_2$), hydrocarbons (stilbene), haloalkanes ($CBr_4$, $CHI_3$, $CH_2I_2$, $C_2H_4I_2$ and $C_2F_4I_2$), organometallic compounds (Platinum Pop, ferrocene, $Fe(CO)_5$, $Ru_3(CO)_{12}$ and $Os_3(CO)_{12}$), and protein molecules (Mb, Hb and Cyt-c). These molecules have been studied previously by TRXD with 100 ps time resolution. In particular, molecules containing heavy atoms are promising since heavy atoms give a large signal and thus a good contrast against the solvent background. In that regard, iodine ($I_2$) is a good candidate for XFEL-based TRXD experiment. The photodissociation and subsequent recombination of iodine in solution have been regarded as a prototype example for the solvent cage effect and thus have been intensively studied [143,212–214]. As shown in Figure 25, once an iodine molecule is excited to a bound B state and then relaxes to the repulsive $^1\Pi$ state, the two iodine atoms start to separate as in the gas phase. However, the excited iodine molecule soon gets hit by surrounding solvent

molecules unlike in the gas phase. As a result, most of the excited iodine molecules recombine geminately to form a wave packet either in the hot ground state or in the $A/A'$ state. As detailed in a previous section, using TRXL with 100 ps time resolution, rather slow relaxation dynamics of $A/A'$ state to the ground state were measured, but vibrational relaxation in the hot ground state and-the $A/A'$ state was barely resolved [215]. Using fs X-ray pulses from XFEL, the vibrational relaxation process that induces the rearrangement of surrounding solvent molecules is readily resolved, accounting for the solute–solvent interaction.

Furthermore, even faster processes can be resolved by making use of the potential sub-100 fs resolution of XFELs, including vibrational and rotational wave-packet motions on the bound B state potential and the curve crossing to a dissociative state. For example, the periods for the vibrational wave-packet motions of iodine in hexane were found to be 160 and 300 fs for coherences in the ground and B states, respectively, at room temperature [214], therefore those wave-packet motions can be readily resolved by an XFEL. The observation of such wave-packet dynamics and related structural changes will give new insight to the geometry of PESs, curve-crossing dynamics and solvent effects on the reaction dynamics (in comparison with the experiment on iodine in the gas phase described in the previous section). However, due to solute–solvent interaction, coherent rovibrational wave packet of iodine in the solution phase dephases much faster than in the gas phase. For example, the dephasing time of a vibrational mode of $\sim$100 $cm^{-1}$ frequency (300 fs period) in the excited B state is only $\sim$300 fs, limiting the visibility of oscillatory wave-packet motions to only a few periods.

Another interesting example for XFEL–TRXL experiment is solvation dynamics. For example, when an fs laser pulse initiates an electronic transition of a dye molecule (e.g. Coumarin 153) dissolved in a polar solvent (e.g. methanol), a large dipole is induced in the excited-state ($S_1$) solute molecule that has zero dipole moment in the ground state ($S_0$). Since the electronic transition is rapid compared to nuclear motions of the solvent molecules, the initial solvation environment is characteristic of the equilibrium condition of $S_0$, not of $S_1$. As time evolves, the surrounding solvent molecules reorganise in response to the change in charge distribution of the solute molecule so that the solvation energy in the excited state can be lowered. Previously, such collective motion of solvent molecules has been probed rather indirectly using optical spectroscopic methods, for example fluorescence dynamic Stokes shift, photon echo and optical Kerr effect techniques [3,216–218]. In contrast, X-ray diffraction can give more direct structural information by the change in the X-ray diffraction pattern induced by the collective motion of the solvent molecules. Since solvation dynamics have been reported to occur in tens to hundreds of femtoseconds, fs X-ray diffraction will be suitable for resolving f process.

Another candidate for XFEL–TRXL experiments in solution is proteins. Although they are much more challenging to study owing to their structural complexity, the reward will be much bigger considering the immense impact of structural biology. As discussed in a previous section, the structural dynamics of proteins, such as Hb, Mb and Cyt-c, have been studied using 100 ps X-ray solution diffraction technique [219,220]. As an example, in the TRXL measurements on two types of Mb with a RMSD less than 0.3 Å, the difference scattering curves of the two are distinctly different. This result highlights the high sensitivity of scattering to subtle structural differences. The improved time resolution

of TRXL using XFEL radiation will elucidate more details of ultrafast dynamics of the protein structural transitions.

As suggested in a previous section with examples of cyclohexadiene and pyridine in the gas phase, chemical reactions of organic molecules without heavy atoms can be readily studied due to the solvent-free nature of the gas-phase environment. However, it might be quite challenging to study the same reactions in solution because of the low contrast of the solute signal against the solvent response and thus the poor SNR. The problem of low SNR might be circumvented by labelling the solute molecule with heavy atoms at the risk of modifying the structure and dynamics of the solute. Alternatively, a solvent containing much heavier atoms than the solute can be used so that collective structural change in the solvent environment can reflect the reaction dynamics of the less visible solute molecules.

### 6.3. *Single-pulse, single-molecule diffraction*



Since XFEL can generate X-ray pulses with photon counts of up to $10^{12}$ photons, it will be possible to realise a novel X-ray scattering experiment: the single-pulse diffraction experiment, where a single-shot image is recorded to capture the reaction dynamics. The single-pulse diffraction experiment will not only increase the data acquisition rate substantially but also alleviate the sample deterioration problem induced by the intense X-ray radiation, especially for fragile proteins. In addition, the problem of the timing jitter between the optical laser pulse and the X-ray pulse can be eliminated if each single pair of the laser and X-ray pulses is time-stamped. In the TRXD setup on the third generation synchrotrons, the diffraction images are typically obtained by accumulating the diffraction signals from $5 \times 10^3$ X-ray pulses corresponding to a total of $\sim 5 \times 10^{12}$ X-ray photons.

Considering that the photon flux of the X-ray pulse generated from XFEL is on the order of $1 \times 10^{12}$, a single shot of the XFEL pulse contains enough photons to generate a diffraction image comparable to an exposure for a few seconds with the third generation synchrotron. Also, if every single image can be recorded with a time index, i.e. time stamped, at the frequency of the macro-bunch train, the images can be sorted in time bins and averaged to improve the SNR. Therefore, the single-pulse diffraction experiment is feasible with high-photon flux XFEL pulses.

As long as the single-pulse diffraction experiment works with a good SNR sufficient for data analysis, we can imagine a more challenging experiment, i.e. a single-pulse, single-molecule X-ray diffraction experiment. In the early stages of the XFEL programme, the single-molecule X-ray diffraction using ultrashort X-ray pulses were proposed by Hajdu and co-workers. Single-molecule diffraction gives the prospect of overcoming the sample damage problem caused by the intense X-ray radiation encountered in conventional diffraction measurements as well as solving the 3-D structure of biological macromolecules without the need of growing well-diffracting single crystals [221–223]. The biggest obstacles in the single-molecule diffraction experiment are poor SNR of the signal diffracted from only a single molecule as well as the difficulty in handling the sample at extremely low concentration. These obstacles can be overcome with the aid of advanced numerical data processing procedures and electrospraying sample injection methods that might eventually make single-molecule diffraction experiment feasible.

The signal amplitude of single-molecule diffraction can be further enhanced if a molecule of interest, e.g. proteins, can be labelled in a site-specific manner using a heavy atom probe that can scatter X-ray much more strongly. For example, a recent study reported that gold nanocrystals can be used as a sensitive heavy atom probe for measuring the length and structural fluctuations of DNA double helix [224]. The single-molecule TRXD measurement using the nanocrystal labelling scheme can complement single-molecule spectroscopy because it directly monitors rapid structural fluctuations of single molecules and allows direct construction of the structural conformation space.

Once the single-molecule diffraction experiment is realised, in addition to the structural analysis of the biological macromolecules, it will have significant implications for the study of chemical reaction dynamics. For example, we can expect to determine the structures of transition states in a chemical reaction as well as nuclear wave functions. Transition states connecting the reactant to the product govern the reaction rates and pathways, but their structure has never been directly characterised due to their extremely low population and occurrence probability. For the same reason, nuclear wave functions of even a simple diatomic molecule have never been directly measured. Since a diffraction pattern from a single molecule is determined by the structure and conformation of the molecule, we can construct an image space consisting of single-molecule diffraction images obtained from all possible structures and orientations of a given molecule. Once such an image space is built, a series of measured single-molecule diffraction images can be compared with the corresponding molecular structures to determine the molecular structure of a given image. Since the occurrence probability of a particular structure is governed by the square of a nuclear wave function, the nuclear wave function can be reconstructed by sorting out a series of single-molecule diffraction images as a function of their occurrence probability and structural parameters. In principle, single-molecule diffraction can detect the instant structure of an individual molecule, and therefore it may also be possible to capture the structure of transition states.



## 7. Summary and future perspectives

In this article, we have described the principles and the experimental details of TRXL with recent examples. With the 100 ps X-ray pulses readily available from synchrotrons, TRXL has been established as a powerful tool for characterising fast structural transition dynamics of chemical reactions and biological processes, ranging from small molecules to proteins in solution. In particular, the technique provides rather direct information on transient molecular structures since the scattering signals are sensitive to all chemical species present in the sample unlike in optical spectroscopy. Although there still remain challenges to overcome, for example, the limited structure and time resolution, TRXL is expected to play an important role in revealing transient structural dynamics in many other systems in solution and liquid phases, especially with the aid of next generation X-ray sources. At the frontier of the technical advances supporting such bright prospects of TRXL is the advent of linac-based X-ray light sources, which can generate X-ray pulses of fs duration. They include SASE-XFEL and energy recovery linacs (ERL) that are currently under development will be available in the near future.

Among these novel X-ray sources, the high-gain XFEL using SASE promises to generate highly coherent, fs X-ray pulses on the order of 100 fs with a high photon flux up

to $10^{13}$ photons per pulse. The superb time resolution of XFEL will enable us to access reaction dynamics in fs time regime, elucidating much more details of ultrafast structural dynamics. Also, the high flux of XFEL provides the potential for single-shot collection of the XFEL signal. On the other hand, ERL can be operated at a high repetition rate on the order of MHz to GHz. Such high repetition rate capability of ERL will be able to significantly improve the SNR of TRXL signal since TRXL is basically a perturbative, pump-probe-type experiment. With such a high-repetition rate X-ray source, TRXL can be implemented combined with a high-repetition rate oscillator instead of fs amplified lasers, which is commonly operated at only a kHz rate. Furthermore, the nanometre-scale size of the X-ray beam from the ERL (typically 100 nm diameter) will allow tight focussing of the laser beam down to the order of micrometers, enabling the collection of signal from a small volume of sample. Since the scattering signal from the small area will be relatively weak, low-noise and fast-gatable 2-D detectors are desirable for future ERL-applied TRXL experiments. The development of pixel detectors using silicon-on-insulator technology will pave the way for such high-performance 2-D detectors.

The excellent beam characteristics of the ERL will be further extended to develop the coherent X-ray source, for example, oscillator-type XFEL (XFEL oscillator or XFEL-O) [225]. The X-ray source generating fully coherent X-ray pulses will serve as the ultimate X-ray light source with superb spatial and temporal coherence. Then, what kind of potential applications can we expect once fully coherent X-ray pulses become available? For example, by making an analogy to the ultrafast optical spectroscopy that fully takes advantage of the temporal coherence of ultrashort optical laser pulses, one could imagine phase-coherent spectroscopy in the X-ray regime with controlled timing, phase and intensity among multiple, coherent X-ray pulses [226]. X-ray radiation has the sub-nanometre wavelength, which corresponds to the sub-attosecond period in the time domain, X-ray pulses offer much higher spatial and temporal resolution than achievable in the optical regime. Thus, the development of X-ray sources that can generate coherent X-ray pulses will revolutionise the whole X-ray science.



## Acknowledgements

We thank the co-workers listed in many of the references of this article. This study was supported by the Creative Research Initiative (Center for Time-Resolved Diffraction) of MEST/NRF. We acknowledge the support from the WCU programme.

## References

[1] J. T. Hynes, in *Ultrafast Dynamics of Chemical Systems*, edited by J. D. Simon (Kluwer, Dordrecht, 1994), pp. 345–381.
[2] H. Frauenfelder and P. G. Wolynes, Science **229**, 337 (1985).
[3] M. Maroncelli, J. MacInnis, and G. R. Fleming, Science **243**, 1674 (1989).
[4] B. Bagchi and A. Chandra, in *Advances in Chemical Physics*, edited by I. Prigogine and S. A. Rice (Wiley, New York, 1991), Vol. 80, pp. 1–126.
[5] M. J. Weaver, Chem. Rev. **92**, 463 (1992).
[6] Y. T. Lee, Science **236**, 793 (1987).
[7] J. J. Lin, J. Zhou, W. Shiu, and K. Liu, Science **300**, 966 (2003).

[8] S. Yan, Y.-T. Wu, B. Zhang, X.-F. Yue, and K. Liu, Science **316**, 1723 (2007).
[9] Y.-J. Lu, L. Lee, J.-W. Pan, T. X. Xie, H. A. Witek, and J. J. Lin, J. Chem. Phys. **128**, 104317 (2008).
[10] X. Liu, J. J. Lin, S. Harich, G. C. Schatz, and X. Yang, Science **289**, 1536 (2000).
[11] Z. R. M. Qiu, L. Che, D. Dai, S. A. Harich, X. Wang, X. Yang, C. Xu, D. Xie, M. Gustafsson, R. T. Skodje, Z. Sun, and D. H. Zhang, Science **311**, 1440 (2006).
[12] A. H. Zewail, Angew. Chem. Int. Ed. **40**, 4371 (2001).
[13] L. R. Khundkar and A. H. Zewail, Annu. Rev. Phys. Chem. **41**, 15 (1990).
[14] A. H. Zewail, *Femtochemistry: Ultrafast Dynamics of the Chemical Bond* (World Scientific, Singapore, 1994), Vol. 1 and 2.
[15] I. V. Hertel and W. Radloff, Rep. Prog. Phys. **69**, 1897 (2006).
[16] M. Wall, A. N. Tarnovsky, T. Pascher, V. Sundstrom, and E. Akesson, J. Phys. Chem. A **107**, 211 (2003).
[17] X. M. Zheng and D. L. Phillips, Chem. Phys. Lett. **324**, 175 (2000).
[18] Y. L. Li, D. M. Chen, D. Q. Wang, and D. L. Phillips, J. Org. Chem. **67**, 4228 (2002).
[19] N. Biswas and S. Umapathy, J. Chem. Phys. **107**, 7849 (1997).
[20] P. Kukura, D. W. McCamant, S. Yoon, D. B. Wandschneider, and R. A. Mathies, Science **310**, 1006 (2005).
[21] Y. Mizutani and T. Kitagawa, Science **278**, 443 (1997).
[22] W. J. Schreier, T. E. Schrader, F. O. Koller, P. Gilch, C. E. Crespo-Hernandez, V. N. Swaminathan, T. Carell, W. Zinth, and B. Kohler, Science **315**, 625 (2007).
[23] S. O. Williams and D. G. Imre, J. Phys. Chem. **92**, 3363 (1988).
[24] P. M. Johnson and C. E. Otis, Annu. Rev. Phys. Chem. **32**, 139 (1981).
[25] D. M. Neumark, Annu. Rev. Phys. Chem. **52**, 255 (2001).
[26] A. Stolow, Annu. Rev. Phys. Chem. **54**, 89 (2003).
[27] D. W. Chandler and P. L. Houston, J. Chem. Phys. **87**, 1445 (1987).
[28] A. J. R. Heck and D. W. Chandler, Annu. Rev. Phys. Chem. **46**, 335 (1995).
[29] G. R. Fleming, Annu. Rev. Phys. Chem. **37**, 81 (1986).
[30] Y.-T. Kao, C. Saxena, L. Wang, A. Sancar, and D. Zhong, Proc. Natl. Acad. Sci. USA **102**, 16128 (2005).
[31] W. Qiu, L. Wang, W. Lu, A. Boechler, D. A. R. Sanders, and D. Zhong, Proc. Natl. Acad. Sci. USA **104**, 5366 (2007).
[32] L. Zhang, L. Wang, Y.-T. Kao, W. Qiu, Y. Yang, O. Okobiah, and D. Zhong, Proc. Natl. Acad. Sci. USA **104**, 18461 (2007).
[33] E. T. J. Nibbering, H. Fidder, and E. Pines, Annu. Rev. Phys. Chem. **56**, 337 (2005).
[34] P. Kukura, D. W. McCamant, and R. A. Mathies, Annu. Rev. Phys. Chem. **58**, 461 (2007).
[35] M. C. Asplund, M. T. Zanni, and R. M. Hochstrasser, Proc. Natl. Acad. Sci. USA **97**, 8219 (2000).
[36] J. R. Zheng, K. W. Kwak, J. Xie, and M. D. Fayer, Science **313**, 1951 (2006).
[37] M. Cho, Chem. Rev. **108**, 1331 (2008).
[38] P. Coppens, Chem. Commun. 1317 (2003).
[39] P. Coppens, I. I. Vorontsov, T. Graber, A. Y. Kovalevsky, Y. S. Chen, G. Wu, M. Gembicky, and I. V. Novozhilova, J. Am. Chem. Soc. **126**, 5980 (2004).
[40] H. Ihee, Acc. Chem. Res. **42**, 356 (2009).
[41] H. Ihee, S. Rajagopal, V. Srajer, R. Pahl, S. Anderson, M. Schmidt, F. Schotte, P. A. Anfinrud, M. Wulff, and K. Moffat, Proc. Natl. Acad. Sci. USA **102**, 7145 (2005).
[42] C. D. Kim, S. Pillet, G. Wu, W. K. Fullagar, and P. Coppens, Acta Cryst. A **58**, 133 (2002).
[43] S. Techert, F. Schotte, and M. Wulff, Phys. Rev. Lett. **86**, 2030 (2001).
[44] F. Schotte, M. Lim, T. A. Jackson, A. V. Smirnov, J. Soman, J. S. Olson, G. N. J. Phillips, M. Wulff, and P. Anfinrud, Science **300**, 1944 (2003).

[45] A. Tomita, T. Sato, K. Ichiyanagi, S. Nozawa, H. Ichikawa, M. Chollet, F. Kawai, S.-Y. Park, T. Tsuduki, T. Yamato, S. Koshihara, and S. Adachi, Proc. Natl. Acad. Sci. USA **106**, 2612 (2009).
[46] V. Srajer, T.-Y. Teng, T. Ursby, C. Pradervand, Z. Ren, S. Adachi, W. Schildkamp, D. Bourgeois, M. Wulff, and K. Moffat, Science **274**, 1726 (1996).
[47] E. Collet, M. H. Lemee-Cailleau, M. Buron-Le Cointe, H. Cailleau, M. Wulff, T. Luty, S. Y. Koshihara, M. Meyer, L. Toupet, P. Rabiller, and S. Techert, Science **300**, 612 (2003).
[48] A. Cavalleri, S. Wall, C. Simpson, E. Statz, D. W. Ward, K. A. Nelson, M. Rini, and R. W. Schoenlein, Nature **442**, 664 (2006).
[49] S. H. Lee, A. L. Cavalieri, D. M. Fritz, M. C. Swan, R. S. Hegde, M. Reason, R. S. Goldman, and D. A. Reis, Phys. Rev. Lett. **95**, 246104 (2005).
[50] A. M. Lindenberg, J. Larsson, K. Sokolowski-Tinten, K. J. Gaffney, C. Blome, O. Synnergren, J. Sheppard, C. Caleman, A. G. MacPhee, D. Weinstein, D. P. Lowney, T. K. Allison, T. Matthews, R. W. Falcone, A. L. Cavalieri, D. M. Fritz, S. H. Lee, P. H. Bucksbaum, D. A. Reis, J. Rudati, P. H. Fuoss, C. C. Kao, D. P. Siddons, R. Pahl, J. Als-Nielsen, S. Duesterer, R. Ischebeck, H. Schlarb, H. Schulte-Schrepping, Th. Tschentscher, J. Schneider, D. von der Linde, O. Hignette, F. Sette, H. N. Chapman, R. W. Lee, T. N. Hansen, S. Techert, J. S. Wark, M. Bergh, G. Huldt, D. van der Spoel, N. Timneanu, J. Hajdu, R. A. Akre, E. Bong, P. Krejcik, J. Arthur, S. Brennan, K. Luening, and J. B. Hastings, Science **308**, 392 (2005).
[51] K. J. Gaffney, A. M. Lindenberg, J. Larsson, K. Sokolowski-Tinten, C. Blome, O. Synnergren, J. Sheppard, C. Caleman, A. G. MacPhee, D. Weinstein, D. P. Lowney, T. Allison, T. Matthews, R. W. Falcone, A. L. Cavalieri, D. M. Fritz, S. H. Lee, P. H. Bucksbaum, D. A. Reis, J. Rudati, A. T. Macrander, P. H. Fuoss, C. C. Kao, D. P. Siddons, R. Pahl, K. Moffat, J. Als-Nielsen, S. Duesterer, R. Ischebeck, H. Schlarb, H. Schulte-Schrepping, J. Schneider, D. von der Linde, O. Hignette, F. Sette, H. N. Chapman, R. W. Lee, T. N. Hansen, J. S. Wark, M. Bergh, G. Huldt, D. van der Spoel, N. Timneanu, J. Hajdu, R. A. Akre, E. Bong, P. Krejcik, J. Arthur, S. Brennan, K. Luening, and J. B. Hastings, Phys. Rev. Lett. **95**, 125701 (2005).
[52] A. L. Cavalieri, D. M. Fritz, S. H. Lee, P. H. Bucksbaum, D. A. Reis, J. Rudati, D. M. Mills, P. H. Fuoss, G. B. Stephenson, C. C. Kao, D. P. Siddons, D. P. Lowney, A. G. MacPhee, D. Weinstein, R. W. Falcone, R. Pahl, J. Als-Nielsen, C. Blome, S. Dursterer, R. Ischebeck, H. Schlarb, H. Schulte-Schrepping, Th. Tschentscher, J. Schneider, O. Hignette, F. Sette, K. Sokolowski-Tinten, H. N. Chapman, R. W. Lee, T. N. Hansen, O. Synnergren, J. Larsson, S. Techert, J. Sheppard, J. S. Wark, M. Bergh, C. Caleman, G. Huldt, D. van der Spoel, N. Timneanu, J. Hajdu, R. A. Akre, E. Bong, P. Emma, P. Krejcik, J. Arthur, S. Brennan, K. J. Gaffney, A. M. Lindenberg, K. Luening, and J. B. Hastings, Phys. Rev. Lett. **94**, 114801 (2005).
[53] D. M. Fritz, D. A. Reis, B. Adams, R. A. Akre, J. Arthur, C. Blome, P. H. Bucksbaum, A. L. Cavalieri, S. Engemann, S. Fahy, R. W. Falcone, P. H. Fuoss, K. J. Gaffney, M. J. George, J. Hajdu, M. P. Hertlein, P. B. Hillyard, M. Horn-von Hoegen, M. Kammler, J. Kaspar, R. Kienberger, P. Krejcik, S. H. Lee, A. M. Lindenberg, B. McFarland, D. Meyer, T. Montagne, É. D. Murray, A. J. Nelson, M. Nicoul, R. Pahl, J. Rudati, H. Schlarb, D. P. Siddons, K. Sokolowski-Tinten, Th. Tschentscher, D. von der Linde, and J. B. Hastings, Science **315**, 633 (2007).
[54] H. Ihee, V. A. Lobastov, U. Gomez, B. M. Goodson, R. Srinivasan, C.-Y. Ruan, and A. H. Zewail, Science **291**, 458 (2001).
[55] R. C. Dudek and P. M. Weber, J. Phys. Chem. A **105**, 4167 (2001).
[56] S. T. Park, J. S. Feenstra, and A. H. Zewail, J. Chem. Phys. **124**, 174707 (2006).
[57] B. J. Siwick, J. R. Dwyer, R. E. Jordan, and R. J. D. Miller, Science **302**, 1382 (2003).
[58] H. Ihee, S. Rajagopal, V. Srajer, R. Pahl, S. Anderson, M. Schmidt, F. Schotte, P. A. Anfinrud, M. Wulff, and K. Moffat, Proc. Natl. Acad. Sci. USA **102**, 7145 (2005).

[59] M. Schmidt, R. Pahl, V. Srajer, S. Anderson, Z. Ren, H. Ihee, S. Rajagopal, and K. Moffat, Proc. Natl. Acad. Sci. USA **101**, 4799 (2004).
[60] A. Debnarova, S. Techert, and S. Schmatz, J. Chem. Phys. **125**, 224101 (2006).
[61] M. Gembicky, S. Adachi, and P. Coppens, J. Synchrotron Rad. **14**, 295 (2007).
[62] I. I. Vorontsov, A. Y. Kovalevsky, Y. S. Chen, T. Graber, M. Gembicky, I. V. Novozhilova, M. A. Omary, and P. Coppens, Phys. Rev. Lett. **94**, 193003 (2005).
[63] A. Plech, M. Wulff, S. Bratos, F. Mirloup, R. Vuilleumier, F. Schotte, and P. A. Anfinrud, Phys. Rev. Lett. **92**, 125505 (2004).
[64] H. Ihee, M. Lorenc, T. K. Kim, Q. Y. Kong, M. Cammarata, J. H. Lee, S. Bratos, and M. Wulff, Science **309**, 1223 (2005).
[65] J. Davidsson, J. Poulsen, M. Cammarata, P. Georgiou, R. Wouts, G. Katona, F. Jacobson, A. Plech, M. Wulff, G. Nyman, and R. Neutze, Phys. Rev. Lett. **94**, 245503 (2005).
[66] M. Cammarata, M. Lorenc, T. K. Kim, J. H. Lee, Q. Y. Kong, E. Pontecorvo, M. Lo Russo, G. Schiro, A. Cupane, M. Wulff, and H. Ihee, J. Chem. Phys. **124**, 124504 (2006).
[67] T. K. Kim, M. Lorenc, J. H. Lee, M. Russo, J. Kim, M. Cammarata, Q. Y. Kong, S. Noel, A. Plech, M. Wulff, and H. Ihee, Proc. Natl. Acad. Sci. USA **103**, 9410 (2006).
[68] J. H. Lee, K. H. Kim, T. K. Kim, Y. Lee, and H. Ihee, J. Chem. Phys. **125**, 174504 (2006).
[69] M. Wulff, S. Bratos, A. Plech, R. Vuilleumier, F. Mirloup, M. Lorenc, Q. Kong, and H. Ihee, J. Chem. Phys. **124**, 034501 (2006).
[70] P. Georgiou, J. Vincent, M. Andersson, A. B. Wohri, P. Gourdon, J. Poulsen, J. Davidsson, and R. Neutze, J. Chem. Phys. **124**, 234507 (2006).
[71] Q. Y. Kong, M. Wulff, J. H. Lee, S. Bratos, and H. Ihee, J. Am. Chem. Soc. **129**, 13584 (2007).
[72] J. H. Lee, J. Kim, M. Cammarata, Q. Kong, K. H. Kim, J. Choi, T. K. Kim, M. Wulff, and H. Ihee, Angew. Chem. Int. Ed. **47**, 1047 (2008).
[73] Q. Kong, J. H. Lee, A. Plech, M. Wulff, H. Ihee, and M. H. J. Koch, Angew. Chem. Int. Ed. **47**, 5550 (2008).
[74] J. H. Lee, T. K. Kim, J. Kim, Q. Kong, M. Cammarata, M. Lorenc, M. Wulff, and H. Ihee, J. Am. Chem. Soc. **130**, 5834 (2008).
[75] M. Cammarata, M. Levantino, F. Schotte, P. A. Anfinrud, F. Ewald, J. Choi, A. Cupane, M. Wulff, and H. Ihee, Nat. Methods **5**, 881 (2008).
[76] J. Vincent, M. Andersson, M. Eklund, A. B. Wohri, M. Odelius, E. Malmerberg, Q. Y. Kong, M. Wulff, R. Neutze, and J. Davidsson, J. Chem. Phys. **130**, 154502 (2009).
[77] M. Christensen, K. Haldrup, K. Bechgaard, R. Feidenhans'l, Q. Y. Kong, M. Cammarata, M. Lo Russo, M. Wulff, N. Harrit, and M. M. Nielsen, J. Am. Chem. Soc. **131**, 502 (2009).
[78] T. Haldrup, H. T. Lemke, K. Haldrup, T. N. Nielsen, D. A. Arms, D. A. Walko, A. Miceli, E. C. Landahl, E. M. Dufresne, and M. M. Nielsen, J. Synchrotron. Rad. **16**, 387 (2009).
[79] K. Ichiyanagi, T. Sato, S. Nozawa, K. H. Kim, J. H. Lee, J. Choi, A. Tomita, H. Ichikawa, S. Adachi, H. Ihee, and S. Koshihara, J. Synchrotron. Rad. **16**, 391 (2009).
[80] L. X. Chen, W. J. H. Jager, G. Jennings, D. J. Gosztola, A. Munkholm, and J. P. Hessler, Science **292**, 262 (2001).
[81] M. Saes, C. Bressler, R. Abela, D. Grolimund, S. L. Johnson, P. A. Heimann, and M. Chergui, Phys. Rev. Lett. **90**, 047403 (2003).
[82] T. Sato, S. Nozawa, K. Ichiyanagi, A. Tomita, M. Chollet, H. Ichikawa, H. Fujii, S. Adachi, and S. Koshihara, J. Synchrotron. Rad. **16**, 110 (2009).
[83] C. Rischel, A. Rousse, I. Uschmann, P.-A. Albouy, J.-P. Geindre, P. Audebert, J.-C. Gauthier, E. Forster, J.-L. Martin, and A. Antonetti, Nature **390**, 490 (1997).
[84] A. Cavalleri, M. Rini, H. H. W. Chong, S. Fourmaux, T. E. Glover, P. A. Heimann, J. C. Kieffer, and R. W. Schoenlein, Phys. Rev. Lett. **95**, 067405 (2005).
[85] A. Cavalleri, S. Wall, C. Simpson, E. Statz, D. W. Ward, K. A. Nelson, M. Rini, and R. W. Schoenlein, Nature **442**, 664 (2006).
[86] M. Bargheer, N. Zhavoronkov, M. Woerner, and T. Elsaesser, ChemPhysChem. **7**, 783 (2006).

[87] T. K. Kim, J. H. Lee, M. Wulff, Q. Y. Kong, and H. Ihee, ChemPhysChem **10**, 1958 (2009).
[88] S. Bratos and M. Wulff, in *Advances in Chemical Physics*, edited by S. Rice (John Wiley & Sons, New York, 2007).
[89] P. R. Longaker and M. M. Litvak, J. Appl. Phys. **40**, 4033 (1969).
[90] M. Cammarata, M. Lorenc, T. K. Kim, J. H. Lee, Q. Y. Kong, E. Pontecorvo, M. L. Russo, G. Schiro, A. Cupane, M. Wulff, and H. Ihee, J. Chem. Phys. **124**, 124504 (2006).
[91] D. Bourgeois, T. Ursby, M. Wulff, C. Pradervand, A. LeGrand, W. Schildkamp, S. Laboure, V. Srajer, T.-Y. Teng, M. Roth, and K. Moffat, J. Synchrotron. Rad. **3**, 65 (1996).
[92] M. Wulff, F. Schotte, G. Naylor, D. Bourgeois, K. Moffat, and G. Mourou, Nucl. Instrum. Methods **A398**, 69 (1997).
[93] S. Nozawa, S. Adachi, J. Takahashi, R. Tazaki, L. Guerin, M. Daimon, A. Tomita, T. Sato, M. Chollet, E. Collet, H. Cailleau, S. Yamamoto, K. Tsuchiya, T. Shioya, H. Sasaki, T. Mori, K. Ichiyanagi, H. Sawa, H. Kawata, and S. Y. Koshihara, J. Synchrotron Rad. **14**, 313 (2007).
[94] B. Lindenau, J. Räbiger, S. Polachowski, and J. K. Fremerey, AIP Conf. Proc. **705**, 1019 (2004).
[95] S. Bratos, F. Mirloup, R. Vuilleumier, and M. Wulff, J. Chem. Phys. **116**, 10615 (2002).
[96] S. Bratos, F. Mirloup, R. Vuilleumier, M. Wulff, and A. Plech, Chem. Phys. **304**, 245 (2004).
[97] M. Wulff, S. Bratos, A. Plech, R. Vuilleumier, F. Mirloup, M. Lorenc, Q. Kong, and H. Ihee, J. Chem. Phys. **124**, 034501 (2006).
[98] E. R. Henry and J. Hofrichter, Meth.Enzymol. **210**, 129 (1992).
[99] http://www.esrf.fr/computing/scientific/FIT2D/
[100] A. Plech, M. Wulff, S. Bratos, F. Mirloup, R. Vuilleumier, F. Schotte, and P. A. Anfinrud, Phys. Rev. Lett. **92**, 125505 (2004).
[101] W. J. Fader, J. Appl. Phys. **47**, 1975 (1976).
[102] S. Bratos, F. Mirloup, R. Vuilleumier, M. Wulff, and A. Plech, Chem. Phys. **304**, 245 (2004).
[103] H. Ihee, M. Lorenc, T. K. Kim, Q. Y. Kong, M. Cammarata, J. H. Lee, S. Bratos, and M. Wulff, Science **309**, 1223 (2005).
[104] R. Srinivasan, J. S. Feenstra, S. T. Park, S. Xu, and A. H. Zewail, Science **307**, 558 (2005).
[105] H. Ihee, J. Cao, and A. H. Zewail, Angew. Chem. Int. Ed. **40**, 1532 (2001).
[106] R. O. Pierce, Wied. Ann. **6**, 597 (1879).
[107] J. Maya, J. Chem. Phys. **67**, 4976 (1977).
[108] B. E. Wilcomb, R. Burnham, and N. Djeu, Chem. Phys. Lett. **75**, 239 (1980).
[109] A. Gedanken, B. Raz, U. Even, and I. Eliezer, J. Mol. Spectrosc. **32**, 287 (1969).
[110] S. Bell, R. D. McKenzie, and J. B. Coon, J. Mol. Spectrosc. **20**, 217 (1966).
[111] C. Whitehurst and T. A. King, J. Phys. D: Appl. Phys. **20**, 1577 (1987).
[112] W. R. Wadt, J. Chem. Phys. **72**, 2469 (1980).
[113] V. Kushawaha and M. Mahmood, J. Appl. Phys. **62**, 2173 (1987).
[114] V. Kushawaha, A. Michael, and M. Mahmood, J. Phys. B: At. Mol. Opt. Phys. **21**, 2507 (1988).
[115] R. Azria, J. P. Ziesel, R. Abouaf, L. Bouby, and M. Tronc, J. Phys. B: At. Mol. Opt. Phys. **16**, L7 (1983).
[116] J. Husain, J. R. Wiesenfeld, and R. N. Zare, J. Chem. Phys. **72**, 2479 (1980).
[117] J. J. A. McGarvey, N.-H. Cheung, A. C. Erlandson, and T. A. Cool, J. Chem. Phys. **74**, 5133 (1981).
[118] J. Maya, IEEE J. Quantum Electron. **15**, 579 (1979).
[119] G. A. Bowmaker, *Spectroscopy of Inorganic-Based Materials* (Wiley, New York, 1987).
[120] A. C. Erlandson and T. A. Cool, Chem. Phys. Lett. **96**, 685 (1983).
[121] R. M. Bowman, M. Dantus, and A. H. Zewail, Chem. Phys. Lett. **156**, 131 (1989).
[122] M. Dantus, R. M. Bowman, M. Gruebele, and A. H. Zewail, J. Chem. Phys. **91**, 7437 (1989).
[123] T. Baumert, S. Pedersen, and A. H. Zewail, J. Phys. Chem. **97**, 12447 (1993).
[124] D. P. Zhong and A. H. Zewail, J. Phys. Chem. A **102**, 4031 (1998).

[125] K. B. Moller and A. H. Zewail, Chem. Phys. Lett. **295**, 1 (1998).
[126] J. Somloi and D. J. Tannor, J. Phys. Chem. **99**, 2552 (1995).
[127] S. Gnanakaran and R. M. Hochstrasser, J. Chem. Phys. **105**, 3486 (1996).
[128] S. Gnanakaran and R. M. Hochstrasser, Int. J. Quantum Chem. **72**, 451 (1999).
[129] S. Gnanakaran, M. Lim, N. Pugliano, M. Volk, and R. M. Hochstrasser, J. Phys.: Condens. Matter **8**, 9201 (1996).
[130] M. H. Lim, M. F. Wolford, P. Hamm, and R. M. Hochstrasser, Chem. Phys. Lett. **290**, 355 (1998).
[131] N. Pugliano, S. Gnanakaran, and R. M. Hochstrasser, J. Photochem. Photobiol. A **102**, 21 (1996).
[132] N. Pugliano, D. K. Palit, A. Z. Szarka, and R. M. Hochstrasser, J. Chem. Phys. **99**, 7273 (1993).
[133] N. Pugliano, A. Z. Szarka, S. Gnanakaran, M. Triechel, and R. M. Hochstrasser, J. Chem. Phys. **103**, 6498 (1995).
[134] N. Pugliano, A. Z. Szarka, and R. M. Hochstrasser, J. Chem. Phys. **104**, 5062 (1996).
[135] M. Volk, S. Gnanakaran, E. Gooding, Y. Kholodenko, N. Pugliano, and R. M. Hochstrasser, J. Phys. Chem. A **101**, 638 (1997).
[136] H. Bursing and P. Vohringer, Phys. Chem. Chem. Phys. **2**, 73 (2000).
[137] T. K. Kim, M. Lorenc, J. H. Lee, M. Russo, J. Kim, M. Cammarata, Q. Y. Kong, S. Noel, A. Plech, M. Wulff, and H. Ihee, Proc. Natl. Acad. Sci. USA **103**, 9410 (2006).
[138] R. L. Strong, J. Am. Chem. Soc. **87**, 3563 (2002).
[139] Z. R. Zhu and J. M. Harris, Chem. Phys. Lett. **186**, 183 (1991).
[140] D. F. Kelley, N. A. Abul-Haj, and D.-J. Jang, J. Chem. Phys. **80**, 4105 (1984).
[141] N. A. Abul-Haj and D. F. Kelley, Chem. Phys. Lett. **119**, 182 (1985).
[142] N. A. Abul-Haj and D. F. Kelley, J. Phys. Chem. **91**, 5903 (1987).
[143] A. L. Harris, J. K. Brown, and C. B. Harris, Annu. Rev. Phys. Chem. **39**, 341 (1988).
[144] R. Neutze, R. Wouts, S. Techert, J. Davidsson, M. Kocsis, A. Kirrander, F. Schotte, and M. Wulff, Phys. Rev. Lett. **87**, 195508 (2001).
[145] Q. Kong, J. H. Lee, M. L. Russo, T. K. Kim, M. Lorenc, M. Cammarata, S. Bratos, T. Buslaps, V. Honkimaki, H. Ihee, and M. Wulff, Acta Cryst. A **66**, 252 (2010).
[146] J. G. Bentsen and M. S. Wrighton, J. Am. Chem. Soc. **109**, 4530 (1987).
[147] B. F. G. Johnson, J. Lewis, and M. V. Twigg, J. Organomet. Chem. **67**, C75 (1974).
[148] Y.-M. Wuu, J. G. Bentsen, C. G. Brinkley, and M. S. Wrighton, Inorg. Chem. **26**, 530 (1987).
[149] M. G. Richmond, Chem. Rev. **248**, 881 (2004).
[150] J. G. Bentsen and M. S. Wrighton, J. Am. Chem. Soc. **109**, 4518 (1987).
[151] M. F. Desrosiers and P. C. Ford, Organometallics **1**, 1715 (1982).
[152] J. Malito, S. Markiewicz, and A. Poe, Inorg. Chem. **21**, 4335 (1982).
[153] J. L. Graff, R. D. Sanner, and M. S. Wrighton, J. Am. Chem. Soc. **101**, 273 (1979).
[154] F. W. Grevels, J. G. A. Reuvers, and J. Takats, J. Am. Chem. Soc. **103**, 4069 (1981).
[155] M. F. Desrosiers, D. A. Wink, R. Trautman, A. E. Friedman, and P. C. Ford, J. Am. Chem. Soc. **108**, 1917 (1986).
[156] F. W. Grevels, W. E. Klotzbucher, J. Schrickel, and K. Schaffner, J. Am. Chem. Soc. **116**, 6229 (1994).
[157] E. A. Glascoe, M. F. Kling, J. E. Shanoski, and C. B. Harris, Organometallics **25**, 775 (2006).
[158] Q. Kong, J. H. Lee, K. H. Kim, J. Kim, M. Wulff, H. Ihee and M. H. Koch, J. Am. Chem. Soc. **132**, 2600 (2010).
[159] B. Peng, Q. S. Li, Y. M. Xie, R. B. King, and H. F Schaefer III, Dalton Trans. 6977 (2008).
[160] A. J. Vlcek, Coord. Chem. Rev. **200**, 933 (2000).
[161] M. F. Desrosiers, D. A. Wink, and P. C. Ford, Inorg. Chem. **24**, 1 (1985).
[162] K. Moffat, Chem. Rev. **101**, 1569 (2001).
[163] A. Grishaev, J. Wu, J. Trewhella, and A. Bax, J. Am. Chem. Soc. **127**, 16621 (2005).

[164] C. D. Schwieters, J. J. Kuszewski, N. Tjandra, and G. M. Clore, J. Magn. Reson. **160**, 65 (2003).
[165] S. Akiyama, S. Takahashi, T. Kimura, K. Ishimori, I. Morishima, Y. Nishikawa, and T. Fujisawa, Proc. Natl. Acad. Sci. USA **99**, 1329 (2002).
[166] M. Kainosho, T. Torizawa, Y. Iwashita, T. Terauchi, A. M. Ono, and P. Güntert, Nature **440**, 52 (2006).
[167] C. M. Jones, E. R. Henry, Y. Hu, C.-K. Chan, S. D. Luck, A. Bhuyan, H. Roder, J. Hofrichter, and W. A. Eaton, Proc. Natl. Acad. Sci. USA **90**, 11860 (1993).
[168] E. Chen, M. J. Wood, A. L. Fink, and D. S. Kliger, Biochemistry **37**, 5589 (1998).
[169] D. Beece, L. Eisenstein, H. Frauenfelder, D. Good, M. C. Marden, L. Reinisch, A. H. Reynolds, L. B. Sorensen, and K. T. Yue, Biochemistry **19**, 5147 (1980).
[170] S. Franzen, B. Bohn, C. Poyart, and J. L. Martin, Biochemistry **34**, 1224 (1995).
[171] L. Richard, L. Genberg, J. Deak, H.-L. Chiu, and R. J. D. Miller, Biochemistry **31**, 10703 (1992).
[172] G. Dadusc, J. P. Ogilvie, P. Schulenberg, U. Marvet, and R. J. D. Miller, Proc. Natl. Acad. Sci. USA **98**, 6110 (2001).
[173] A. Sato and Y. Mizutani, Biochemistry **44**, 14709 (2005).
[174] X. Xie and J. D. Simon, Biochemistry **30**, 3682 (1991).
[175] M. Sakakura, S. Yamaguchi, N. Hirota, and M. Terazima, J. Am. Chem. Soc. **123**, 4286 (2001).
[176] L. Y. Zhang, L. J. Wang, Y. T. Kao, W. H. Qiu, Y. Yang, O. Okobiah, and D. Zhong, Proc. Natl. Acad. Sci. USA **104**, 18461 (2007).
[177] M. Schmidt, K. Nienhaus, R. Pahl, A. Krasselt, S. Anderson, F. Parak, G. U. Nienhaus, and V. Srajer, Proc. Natl. Acad. Sci. USA **102**, 11704 (2005).
[178] D. Bourgeois, B. Vallone, F. Schotte, A. Arcovito, A. E. Miele, G. Sciara, M. Wulff, P. Anfinrud, and M. Brunori, Proc. Natl. Acad. Sci. USA **100**, 8704 (2003).
[179] A. Ostermann, R. Waschipky, F. G. Parak, and G. U. Nienhaus, Nature **404**, 205 (2000).
[180] V. Srajer, T. Teng, T. Ursby, C. Pradervand, Z. Ren, S. Adachi, W. Schildkamp, D. Bourgeois, M. Wulff, and K. Moffat, Science **274**, 1726 (1996).
[181] M. L. Quillin, T. Li, J. S. Olson, G. N. Phillips Jr, Y. Dou, M. Ikeda-Saito, R. Regan, M. Carlson, Q. H. Gibson, H. Li, and R. Elber, J. Mol. Biol. **245**, 416 (1995).
[182] R. Aranda, E. J. Levin, F. Schotte, P. A. Anfinrud, and G. N. Phillips, Acta Cryst. D **62**, 776 (2006).
[183] M. M. Silva, P. H. Rogers, and A. Arnone, J. Biol. Chem. **267**, 17248 (1992).
[184] D. I. Svergun, V. Petoukhov, and M. H. J. Koch, Biophys. J. **80**, 2946 (2001).
[185] D. I. Svergun and M. H. J. Koch, Curr. Opin. Struct. Biol. **12**, 654 (2002).
[186] P. Chacon, F. Moran, J. F. Diaz, E. Pantos, and J. M. Andreu, Biophys. J. **74**, 2760 (1998).
[187] D. I. Svergun, Biophys. J. **76**, 2879 (1999).
[188] D. Walther, F. E. Cohen, and S. Doniach, J. Appl. Cryst. **33**, 350 (2000).
[189] M. V. Petoukhov and D. I. Svergun, Biophys. J. **89**, 1237 (2005).
[190] M. Kojima, A. A. Timchenko, J. Higo, K. Ito, H. Kihara, and K. Takahashi, J. Appl. Cryst. **37**, 103 (2004).
[191] J. G. Grossman, M. Neu, E. Pantos, F. J. Schwab, R. W. Evans, E. Townes-Andrews, P. F. Lindley, H. Appel, W.-G. Thies, and S. S. Hasnain, J. Mol. Biol. **225**, 811 (1992).
[192] I. Micetic and B. Salvato, Micron **35**, 17 (2004).
[193] M. Andersson, E. Malmerberg, S. Westenhoff, G. Katona, M. Cammarata, A. B. Wohrl, L. C. Johansson, F. Ewald, M. Eklund, M. Wulff, J. Davidsson, and R. Neutze, Structure **17**, 1265 (2009).
[194] O. Beja, E. N. Spudich, J. L. Spudich, M. Leclerc, and E. F. DeLong, Nature **411**, 786 (2001).
[195] R. Neutze, E. Pebay-Peyroula, K. Edman, A. Royant, J. Navarro, and E. M. Landau, Biochim. Biophys. Acta **1565**, 144 (2002).

[196] D. Svergun, C. Barberato, and M. H. J. Koch, J. Appl. Cryst. **28**, 768 (1995).
[197] K. Edman, A. Royant, G. Larsson, F. Jacobson, T. Taylor, D. van der Spoel, E. M. Landau, E. Pebay-Peyroula, and R. Neutze, J. Biol. Chem. **279**, 2147 (2004).
[198] A. Royant, K. Edman, T. Ursby, E. Pebay-Peyroula, E. M. Landau, and R. Neutze, Nature **406**, 645 (2000).
[199] S. Subramaniam and R. Henderson, Nature **406**, 653 (2000).
[200] J. C. Williamson, J. Cao, H. Ihee, H. Frey, and A. H. Zewail, Nature **386**, 159 (1997).
[201] H. Ihee, V. A. Lobastov, U. M. Gomez, B. M. Goodson, R. Srinivasan, C.-Y. Ruan, and A. H. Zewail, Science **291**, 458 (2001).
[202] C.-Y. Ruan, V. A. Lobastov, R. Srinivasan, B. M. Goodson, H. Ihee, and A. H. Zewail, Proc. Natl. Acad. Sci. USA **98**, 7117 (2001).
[203] P. Reckenthaeler, M. Centurion, W. Fuß, S. A. Trushin, F. Krausz, and E. E. Fill, Phys. Rev. Lett. **102**, 213001 (2009).
[204] J. C. Williamson and A. H. Zewail, J. Phys. Chem. **98**, 2766 (1994).
[205] J. D. Geiser and P. M. Weber, J. Chem. Phys. **108**, 8004 (1998).
[206] N. E. Henriksen and K. B. Møller, J. Phys. Chem. B **112**, 558 (2008).
[207] R. M. Bowman, M. Dantus, and A. H. Zewail, Chem. Phys. Lett. **161**, 297 (1989).
[208] M. Dantus, R. M. Bowman, and A. H. Zewail, Nature **343**, 737 (1990).
[209] D. M. Willberg, J. J. Breen, M. Gutmann, and A. H. Zewail, J. Phys. Chem. **95**, 7136 (1991).
[210] V. A. Lobastov, R. Srinivasan, B. M. Goodson, C.-Y. Ruan, J. S. Feenstra, and A. H. Zewail, J. Phys. Chem. A **105**, 11159 (2001).
[211] T. S. Dibble and L. S. Bartell, J. Phys. Chem. **96**, 8603 (1992).
[212] L. F. Meadows and R. M. Noyes, J. Am. Chem. Soc. **82**, 1872 (1960).
[213] Y. Yan, R. M. Whitnell, K. R. Wilson, and A. H. Zewail, Chem. Phys. Lett. **193**, 402 (1992).
[214] N. F. Scherer, D. M. Jonas, and G. R. Fleming, J. Chem. Phys. **99**, 153 (1993).
[215] M. Wulff, S. Bratos, A. Plech, R. Vuilleumier, F. Mirloup, M. Lorenc, Q. Kong, and H. Ihee, J. Chem. Phys. **124**, 034501 (2006).
[216] G. R. Fleming and M. Cho, Annu. Rev. Phys. Chem. **47**, 109 (1996).
[217] R. M. Stratt and M. Maroncelli, J. Phys. Chem. **100**, 12981 (1996).
[218] S. Park, B. N. Flanders, X. Shang, R. A. Westervelt, J. Kim, and N. F. Scherer, J. Chem. Phys. **118**, 3917 (2003).
[219] M. Cammarata, M. Levantino, F. Schotte, P. A. Anfinrud, F. Ewald, J. Choi, A. Cupane, M. Wulff, and H. Ihee, Nat. Methods **5**, 881 (2008).
[220] S. Ahn, K. H. Kim, Y. Kim, J. Kim, and H. Ihee, J. Phys. Chem. B **113**, 13131 (2009).
[221] R. Neutze, R. Wouts, D. van der Spoel, E. Weckert, and J. Hajdu, Nature **406**, 752 (2000).
[222] J. Hajdu, Curr. Opin. Struct. Biol. **10**, 569 (2000).
[223] G. Webster and R. Hilgenfeld, Single Mol. **3**, 63 (2002).
[224] R. S. Mathew-Fenn, R. Das, and P. A. B. Harbury, Science **322**, 446 (2008).
[225] K.-J. Kim, Y. Shvyd'ko, and S. Reiche, Phys. Rev. Lett. **100**, 244802 (2008).
[226] S. Mukamel, D. Abramavicius, L. Yang, W. Zhuang, I. V. Schweigert, and D. V. Voronine, Acc. Chem. Res. **42**, 553 (2009).
[227] S. Jun, J. H. Lee, J. Kim, J. Kim, K. H. Kim, Q. Kong, T. K. Kim, M. L. Russo, M. Wulff and H. Ihee, Phys. Chem. Chem. Phys. in press (2010), DOI: 10.1039/c002004d.
[228] T. K. Kim, M. Lorenc, J. H. Lee, M. L. Russo, J. Kim, M. Cammarata, Q. Kong, S. Noel, A. Plech, M. Wulff, and H. Ihee, Proc. Natl. Acad. Sci. USA **103**, 9410 (2006).
[229] A. M. Lindenberg, Y. Acremann, D. P. Lowney, P. A. Heimann, T. K. Allison, T. Matthews, and R. W. Falcone, J. Chem. Phys. **122**, 204507 (2005).
[230] P. Georgiou, J. Vincent, M. Andersson, A. B. Wohrl, P. Gourdon, J. Poulsen, J. Davidsson, and R. Neutze, J. Chem. Phys. **124**, 234507 (2006).
[231] J. Kim, K. H. Kim, J. H. Lee, and H. Ihee, Acta Cryst. A **66**, 270 (2010).